



**DGK**

Veröffentlichungen der DGK

Ausschuss Geodäsie der Bayerischen Akademie der Wissenschaften

---

Reihe C

Dissertationen

Heft Nr. 912

**Philipp J. Schneider**

**On the Analysis and Patterns of Persistent Scatterer  
Interferometry Results for Satellite-based Deformation  
Monitoring**

**München 2023**

**Bayerische Akademie der Wissenschaften**

ISSN 0065-5325

ISBN 978-3-7696-5324-3

---

Diese Arbeit ist gleichzeitig veröffentlicht in:  
OPUS – Online Publikationen der Universität Stuttgart  
<http://dx.doi.org/10.18419/opus-13477>, Stuttgart 2023







# On the Analysis and Patterns of Persistent Scatterer Interferometry Results for Satellite-based Deformation Monitoring

A thesis

accepted by the Faculty of Aerospace Engineering and Geodesy  
of the University of Stuttgart  
in partial fulfillment of the requirements for the degree of  
Doctor of Engineering Sciences (Dr.-Ing.)

by

Philipp J. Schneider, M.Sc.

born in Stuttgart

München 2023

Bayerische Akademie der Wissenschaften

Adresse der DGK:



Ausschuss Geodäsie der Bayerischen Akademie der Wissenschaften (DGK)

Alfons-Goppel-Straße 11 • D – 80 539 München

Telefon +49 – 331 – 288 1685 • E-Mail [post@dgk.badw.de](mailto:post@dgk.badw.de)

<http://www.dgk.badw.de>

Main referee: Prof. Dr.-Ing. Uwe Sörgel

Co-referee: Prof. Dr.-Ing. Stefan Hinz

Day of the exam: 21.04.2023

---

© 2023 Bayerische Akademie der Wissenschaften, München

Alle Rechte vorbehalten. Ohne Genehmigung der Herausgeber ist es auch nicht gestattet,  
die Veröffentlichung oder Teile daraus auf photomechanischem Wege (Photokopie, Mikrokopie) zu vervielfältigen

ISSN 0065-5325

ISBN 978-3-7696-5324-3

# Contents

<b>Abstract</b>	<b>5</b>
<b>Kurzfassung</b>	<b>7</b>
<b>Acronyms</b>	<b>9</b>
<b>1 Introduction</b>	<b>11</b>
1.1 Motivation . . . . .	11
1.2 Objectives . . . . .	12
1.3 Outline . . . . .	12
<b>2 Principles of Persistent Scatterer Interferometry</b>	<b>15</b>
2.1 Differential Interferometric Synthetic Aperture Radar . . . . .	15
2.1.1 The Radar Principle . . . . .	15
2.1.2 Common Wavelengths . . . . .	16
2.1.3 Scattering Properties . . . . .	18
2.1.4 Resolution of Side Looking Real Aperture Radar Systems . . . . .	21
2.1.5 The Synthetic Aperture Radar Principle . . . . .	22
2.1.6 Geocoding of SAR Images . . . . .	27
2.1.7 Interferometric Synthetic Aperture Radar . . . . .	27
2.1.8 Differential Interferometric Synthetic Aperture Radar . . . . .	30
2.1.9 Persistent Scatterer Interferometry . . . . .	30
2.1.10 Other Mentionable DInSAR Techniques . . . . .	34
2.1.11 DInSAR Analysis Software . . . . .	35
2.1.12 Interferometry Capable SAR-Missions . . . . .	35
2.2 Using Persistent Scatterer Interferometry for Deformation Analysis and Monitoring . . . . .	36
2.3 Bottom Line . . . . .	39
<b>3 Investigation into Deformations of Large Surfaces</b>	<b>41</b>
3.1 Grid-Base Representation . . . . .	41
3.1.1 Spatial Interpolation . . . . .	41
3.2 Temporal Interpolation . . . . .	42
3.2.1 Polynomial Approximation for Resampling . . . . .	43
3.3 Using Multiple Observations for Decomposition . . . . .	43
3.4 Spectral Analysis of Time-Series Fields . . . . .	44
3.4.1 Empirical Orthogonal Functions for the Analysis of a Field of Time-Series . . . . .	45
3.5 Experiments . . . . .	47
3.5.1 Interpolation and Decomposition . . . . .	47
3.5.2 Temporal Interpolation and Time Series Decomposition . . . . .	50
3.5.3 Spectral Analysis . . . . .	51

<b>4</b>	<b>Monitoring of Single Buildings</b>	<b>57</b>
4.1	Extracting PS Points on Buildings	58
4.1.1	City-wide Based on OpenStreetMap Footprints	58
4.1.2	Reverse Geocoding of OpenStreetMap Footprints	58
4.2	Finding Groups of PS Points on a Building	59
4.2.1	Deformation Space	60
4.2.2	Distance Metric	61
4.2.3	Non-linear Dimension Reduction Based on a Hybrid-Distance Metric	61
4.2.4	Clustering Workflow	62
4.2.5	Influence of Different Persistent Scatterer Interferometry (PSI) Processing Chains	63
4.3	Comparing PS Groups to Ground-based Measurements	64
4.3.1	Line-of-Sight to Vertical Deformation	64
4.3.2	Projection of 3 Dimensional Deformation to Line-of-sight Deformation	64
4.4	Integrating PS Points into Building Information Systems	64
4.4.1	Building Information Systems	65
4.4.2	Structured Meshes	65
4.4.3	Cluster to Segment Assignment	65
4.4.4	Quality Metric	67
4.4.5	Industry Foundation Classes	68
4.4.6	Integration with Industry Foundation Classes (IFC)	68
4.5	Experiments	70
4.5.1	Reverse Geocoding	70
4.5.2	Comparing PS Groups to Ground-based Measurements	72
4.5.3	Detecting Damage	76
4.5.4	Linking Groups to Structures in Mesh	78
4.5.5	Assigning Information to IFC File	82
4.5.6	Conclusion	83
<b>5</b>	<b>Web Platforms</b>	<b>85</b>
5.1	Tools	85
5.1.1	Web Development with HTML and JavaScript	86
5.1.2	Tiling of large Datasets	86
5.1.3	Processing of IFC files	86
5.2	Important Properties and Graphical User Interface Elements	87
5.2.1	Single PS Points	87
5.2.2	Clusters and 3D Building Models	88
5.3	Examples	90
5.3.1	City Wide Ground Motion Service	90
5.3.2	Project-Related Multi-modal Platform	92
5.3.3	Visualizing PS Groups on Single Buildings	95
5.3.4	Augmenting Building Information Models With PS-InSAR Data	97
<b>6</b>	<b>Conclusion, Limitations and Outlook</b>	<b>99</b>
	<b>Appendix</b>	<b>101</b>
A	Principles	102
	<b>Bibliography</b>	<b>105</b>
	<b>Acknowledgments</b>	<b>115</b>
	<b>Curriculum Vitae</b>	<b>117</b>

# Abstract

The remote sensing method Persistent Scatterer Interferometry (PSI) has developed in the last two decades into a tool for monitoring deformations of the earth's surface. Hereby it can be applied to large areas and scenes like earth quakes, landslides or sinkholes but the increasing availability of high resolution Synthetic Aperture Radar (SAR) data also enables a monitoring of small scenes like individual buildings. PSI is recognized and appreciated in the remote sensing community and its benefit has been proven in countless applications.

The PSI principle is based on the evaluation of time series of coherent SAR satellite images and considers the relative phase change over time for individual pixels. As a result of this interferometric evaluation, time series are obtained, which capture line-of-sight (LOS) movement of a scatterer over time with millimetre accuracy.

The PSI method is especially suited for urban areas, because of the high density of good radar back scatterers in these locations. For high-resolution SAR data, such as those acquired by the TerraSAR-X mission, millions of such so-called Persistent Scatterer (PS) points and their deformation time series can be obtained. The presentation, evaluation, and interpretation of such data is still a challenge.

The here presented research contributes to the question of how the joint analysis of many PS points and their time series can be used to infer the underlying causes of the deformation. The investigation of such a field of time series helps in the understanding of temporal and spatial patterns in movements.

A distinction is made between the analysis of large-scale areas and the consideration of points on individual buildings. For wide-area deformations, such as those caused by underground constructions, mining activities or by undermining groundwater flow, adapted methods from meteorology, interpolation and decomposition procedures of different observation geometries are presented and discussed.

For the monitoring of individual structures, such as single buildings, methods were developed that combine SAR data and geo-data from other sources, such as Airborne Laser Scanning (ALS) data and crowd sourced building circumferences. It can be shown that by grouping PS points that have correlated motion patterns, a building can be segmented into its statically independently moving elements. To achieve such a clustering in a robust way, so it can be applied to different data sources, a non-linear dimension reduction based on a hybrid distance metric is introduced.

The results from such a clustering can then be integrated into detailed 3D models, such as those available for Building Information Modeling (BIM) based construction processes, and thus offer the possibility of a continuous and efficient structural monitoring of a building.

Often PSI results have to be communicated to experts from non-SAR affine fields such as civil- and geo-engineering for interpretation, which can be challenging without specialized software. For this purpose, exemplary web portals are presented here, that allow PSI results to be displayed interactively. Such platforms are addressing the specific complexity of PSI data, so that informed decisions can be made.

The utility of an ensemble evaluation of many PSI time series can be demonstrated, as it proves beneficial in wide-area processes. Motion patterns become identifiable and their spatial propagation can undergo analysis. When considering PS points on single buildings, a grouping of points based on their deformation patterns leads to redundant measurement and segments a structure into its independently moving parts. This

segmentation can then be integrated into existing 3D building models and industry standards, signifying an important advancement towards automated and city-wide risk assessment of buildings. Web-based analysis platforms, specifically tailored for the SAR data, serve as a decision support system (DSS) and aid in sharing the findings with non-SAR experts.

# Kurzfassung

Die Fernerkundungsmethode Persistent Scatterer Interferometry (PSI) hat sich in den letzten zwei Jahrzehnten zu einem Instrument für die Deformationsüberwachung entwickelt. Dabei kann sie für weiträumige Gebiete wie Erdbeben, Erdrutsche oder Senkungen eingesetzt werden allerdings ermöglicht die zunehmende Verfügbarkeit von hochauflösenden Synthetic Aperture Radar (SAR)-Daten auch ein kleinräumiges Deformationsmonitoring, etwa zur Überwachung einzelner Gebäude. PSI ist in der Fernerkundungsgemeinschaft anerkannt und geschätzt, und seine Vorzüge haben sich in unzähligen Anwendungen bewährt. Das PSI-Prinzip basiert auf der Auswertung von Zeitreihen kohärenter SAR-Satellitenbilder und berücksichtigt die relative Phasenänderung über die Zeit für einzelne Pixel. Als Ergebnis dieser interferometrischen Auswertung erhält man Zeitreihen, die die LOS-Bewegung eines Streuers über die Zeit mit Millimetergenauigkeit erfassen. Die PSI-Methode eignet sich besonders für urbane Gebiete, da es dort eine hohe Dichte an guten Radarrückstreuern gibt. Für hochauflösende SAR-Daten, wie sie von der TerraSAR-X-Mission erfasst werden, können Millionen solcher so genannter Persistent Scatterer (PS)-Punkte und deren Deformationszeitreihen gewonnen werden. Die Darstellung, Auswertung und Interpretation solcher Daten ist nach wie vor eine Herausforderung.

Die hier vorgestellte Forschung leistet einen Beitrag zu der Frage, wie die gemeinsame Analyse vieler PS-Punkte und ihrer Zeitreihen genutzt werden kann, um auf die zugrunde liegenden Ursachen der Deformation zu schließen. Die Untersuchung eines solchen Feldes von Zeitreihen hilft beim Verständnis von zeitlichen und räumlichen Mustern in Bewegungen. Es wird unterschieden zwischen der Analyse großflächiger Bereiche und der Betrachtung von Punkten auf einzelnen Gebäuden. Für großflächige Verformungen, wie sie z.B. durch unterirdische Bauten, Bergbauaktivitäten oder durch unterspülendes Grundwasser verursacht werden, werden angepasste Methoden aus der Meteorologie, Interpolations- und Zerlegungsverfahren verschiedener Beobachtungsgeometrien vorgestellt und diskutiert. Für die Überwachung einzelner Strukturen, wie z.B. individueller Gebäude, wurden Methoden entwickelt, die SAR-Daten und Geodaten aus anderen Quellen, wie z.B. ALS-Daten und Gebäudeumrisse, kombinieren. Es kann gezeigt werden, dass durch die Gruppierung von PS-Punkten, welche korrelierte Bewegungsmuster aufweisen, ein Gebäude in seine statisch unabhängig bewegten Elemente segmentiert werden kann. Um ein solches Clustering auf robuste Weise zu erreichen, so dass es auf verschiedene Datenquellen angewendet werden kann, wird eine nichtlineare Dimensionsreduktion basierend auf einer hybriden Distanzmetrik eingeführt. Die Ergebnisse eines solchen Clustering können in detaillierte 3D-Modelle, wie sie für BIM-Konstruktionen verfügbar sind, integriert werden und bieten so die Möglichkeit eines kontinuierlichen und effizienten Monitorings eines Gebäudes.

Häufig müssen PSI-Ergebnisse zur Interpretation an Experten aus nicht-SAR-affinen Bereichen wie Bau- und Geotechnik weitergegeben werden. Zu diesem Zweck werden beispielhafte Webportale vorgestellt, die eine interaktive Darstellung von PSI-Ergebnissen ermöglichen. Solche Plattformen tragen der spezifischen Komplexität von PSI-Daten Rechnung, so dass fundierte Entscheidungen getroffen werden können.

Es kann gezeigt werden, dass eine Ensemble-Auswertung vieler PSI-Zeitreihen vorteilhaft ist. Für großflächige Prozesse können Bewegungsmuster identifiziert und deren räumliche Ausbreitung analysiert werden. Für die Betrachtung von PS-Punkten an Einzelgebäuden kann gezeigt werden, dass eine Gruppierung von Punkten auf der Basis ihrer Deformationsmuster zu einer redundanten Messung führt und ein

Bauwerk so in seine unabhängig voneinander bewegten Teile segmentieren werden kann. Eine solche Segmentierung kann dann in bestehende 3D-Gebäudemodelle und Industriestandards integriert werden. Dies ist ein wichtiger Schritt in Richtung einer automatisierten und stadtweiten Risikobewertung von Gebäuden. Webbasierte Analyseplattformen, die speziell auf SAR zugeschnitten sind, dienen so als Entscheidungshilfe und helfen dabei, PSI Ergebnisse mit Nicht-SAR-Experten zu teilen.



# Acronyms

**ALS** Airborne Laser Scanning

**APS** atmospheric and orbital phase screen

**BBD** Ground Motion Service Germany

**BIM** Building Information Modeling

**CR** corner reflector

**DA** Dispersion of Amplitude

**DBSCAN** density-based spatial clustering of applications with noise

**DEM** digital elevation model

**DInSAR** Differential Interferometric Synthetic Aperture Radar

**DSM** digital surface model

**DSS** decision support system

**DS** Distributed Scatterer

**EGMS** European Ground Motion Service

**EOF** Empirical Orthogonal Functions

**ESA** European Space Agency

**FFT** fast Fourier transformation

**GIS** geographic information system

**GNSS** Global Navigation Satellite System

**GSD** ground sampling distance

**GT** ground truth

**IFC** Industry Foundation Classes

**InSAR** Interferometric Synthetic Aperture Radar

**LOS** line-of-sight

**LiDAR** Light Detection And Ranging

<b>LuT</b>	Look-up Table
<b>OSM</b>	OpensStreetMap
<b>PRF</b>	pulse repetition frequency
<b>PSI</b>	Persistent Scatterer Interferometry
<b>PS</b>	Persistent Scatterer
<b>radar</b>	radio detection and ranging
<b>RTE</b>	Residual Topographic Error
<b>SAR</b>	Synthetic Aperture Radar
<b>SBAS</b>	Short Baseline Subsets
<b>SL</b>	Slant-Range
<b>SRTM</b>	Shuttle Radar Topography Mission
<b>StaMPS</b>	Stanford Method for Persistent Scatterers
<b>UMAP</b>	Uniform Manifold Approximation and Projection

# Chapter 1

## Introduction

### 1.1 Motivation

In the last two decades, the Differential Interferometric Synthetic Aperture Radar (DInSAR) technique Persistent Scatterer Interferometry (PSI) has become a widely adopted accepted, and understood technique. By analyzing the phase change of *persistent* radar scatterers over time, it allows the derivation of precise deformation time series from a staple of coherent Synthetic Aperture Radar (SAR) images. Several commercial and open algorithms can be used to carry out the analysis and the increasing availability of SAR images makes it a popular tool in seismology, civil engineering, disaster monitoring, and risk assignment for urban structures.

When discussing PSI results it is common to show a velocity map and pick out single points and analyze the time series of them. This approach can be sufficient if the Persistent Scatterer (PS) point cloud is very sparse or if the area of interest is small. When analyzing a large region or a dense PS point cloud, prior knowledge of the expected deformations and their causes is required in order to know where to focus the investigations. Such prior knowledge could be data from other sources that are often provided by non-DInSAR experts like civil engineers, geologists, or urban planners. For such specialists, it can be challenging to interpret the raw PSI results, since they commonly consist of hundreds of thousands of points and their associated time series.

In the here presented dissertation thesis, novel approaches for the combined analysis of many PS points at once are introduced. The focus hereby is on the post-processing of PS points. In this thesis, methods are discussed that instead of analyzing single PS points, rather consider the entire field of PS points and their deformation patterns, or time series. This gives an insight into the spatial distribution of an underlying deformation process. It is differentiated between large-scale analyses and the investigation into single buildings. A wide area deformation is typically surface rise or subsidence caused by underground construction, mining, water flow, or seismic activities. For the analysis of single buildings, the PSI data can be combined with data from other sources like dense LiDAR point clouds and building footprint databases or detailed 3D models. It is shown that PS points on a building show a correlated deformation if they lay on the same rigid structure e.g. the same part of the facade or roof. This fact can be used to segment a building into structural segments that can be combined with a semantic model of the building coming for example from a Building Information Modeling (BIM) model to integrate remote sensing-based monitoring into such a digital twin.

When presenting such complex 4D data to decision-makers novel approaches and analysis platforms have to be thought out. Experimental web-based platforms were developed in this thesis to present important

features and visualization concepts of such a decision support system (DSS) and to demonstrate how to integrate remote sensing-based monitoring into existing industry standards for building models.

The scope of this research is on the post-processing of PSI points, by finding and visualizing anomalies, patterns, and correlations within the data sets to discover relationships that would otherwise not be obvious. The developed algorithms are applied in qualitative experiments on several test sites and compared to data from other sources.

The overarching objective of this study is to develop methods, that enable a city-wide single building monitoring via the PSI method. The integration of PSI into the existing city and building models is an important step in this direction. The availability of high-resolution SAR data and accurate urban digital twins could make such efforts possible in the near future and this contribution advances the field of remote sensing in this direction.

## 1.2 Objectives

The concrete objective of this thesis is the development of new approaches for the joined analysis and visualization of PSI products. Here, methods for both, large areas and single buildings should be investigated. The integration of the findings from the PSI analysis with multi-modal data coming from official surveying or BIM models should be addressed. Finally, web-based platforms to visualize the findings to experts from other fields are discussed.

- PSI for the monitoring of large surface deformation. Thereby not only looking at single scatterers and their deformation histories but rather an ensemble of points from different view angles and using techniques from meteorology to find patterns in such data (Brockmann et al., 2020; Schneider and Soergel, 2020a,b).
- We investigated in groups of points that show correlated deformation behavior. Such groups can be found e.g. on rigid parts of a building. They are interesting since they give an overview of the extension of such rigid components and represent a redundant measurement. Ground-based measurements are used to evaluate such groups (Schneider et al., 2020).
- Automatically extract points on individual buildings, based on OpenStreetMap (OSM) data and a reverse geocoding approach. To improve the clustering by applying non-linear dimension reduction and a hybrid distance metric. (Schneider and Soergel, 2021b,a)
- Bring in prior knowledge about the buildings structure and its statics by combining the groups of PS points with semantic geometric representation, coming e.g. from a BIM model (Schneider and Soergel, 2022)
- Integrating the remote sensing monitoring data into the industry standard Industry Foundation Classes (IFC) for BIM models.
- Visualizing the findings in custom DSS that are web-based and therefore easy to access without specialized software and show the PSI specific aspects of the datasets.

## 1.3 Outline

This work is structured into 5 chapters, each chapter consists of several sections which can have subsections themselves. Chapter 1 is an introduction to this thesis, including the motivation along with an overview over

objectives and the research and scientific publications that led to this thesis. Chapter 2 gives an overview of the here used methods while focusing on the deduction of the Persistent Scatterer Interferometry (PSI) algorithm. At the end of this chapter, previous related work is discussed and open questions in the current state of the art are pointed out. Chapter 3 discusses methods for the evaluation of PSI results in a large area, while Chapter 4 focuses on its application for building monitoring. In Chapter 5 some concepts for the presentation of PSI data through web-based platforms are discussed. At the end of Chapter 3 to 5 experimental results for the presented methods are shown. On page 101, an appendix can be found.

Figures, Tables, and Equations are referred to with their chapter and section number. If an element is found in the appendix, it is referred to by a letter.



## Chapter 2

# Principles of Persistent Scatterer Interferometry

In this chapter, Persistent Scatterer Interferometry (PSI) is introduced. It begins with the discussion of the general radar principles, Synthetic Aperture Radar (SAR) and SAR Interferometry, and concludes with the principles of Differential Interferometric Synthetic Aperture Radar (DInSAR). The focus of this chapter is the explanation of the advantages and challenges of this powerful remote sensing method. In a brief review of the Persistent Scatterer Interferometry (PSI) method, the history and variations in the various approaches will be discussed. Subsequently, an overview of the applications of Persistent Scatterer Interferometry (PSI) in monitoring will be given, showing that the method has arrived in practice. However there are still open questions in the evaluation of the results of its application, some of these questions will be addressed in the succeeding chapters.

## 2.1 Differential Interferometric Synthetic Aperture Radar

Differential Interferometric Synthetic Aperture Radar (DInSAR) is a generic term for various modern evaluation methods for SAR data. Since a number of previous knowledge and explanations of terms are necessary for the principle understanding of this advanced method, an elaboration is done in the following subsections. The radio detection and ranging (radar) approach and its development up to the SAR and its interferometric evaluations are explained. An overview of the different wavelengths, used in space-born radar applications is given, followed by the physical scattering properties of different materials and environments that are important to interpreting the later SAR images and their more advanced derived DInSAR products. The important distortion and resolution geometry are discussed because they are necessary to understand the accuracy limitations of the PSI technique that is explained at the end of this section.

### 2.1.1 The Radar Principle

Radio detection and ranging (radar) is the generic term for an active remote sensing method that uses radio waves to determine the distance (ranging), angle, or velocity of objects. In its purest form, an electromagnetic pulse is transmitted from an antenna and propagates in a spherical manner at the speed of light.

If the electromagnetic waves hit a target, a part of the pulse is spherically reflected with power  $P_R$ . When

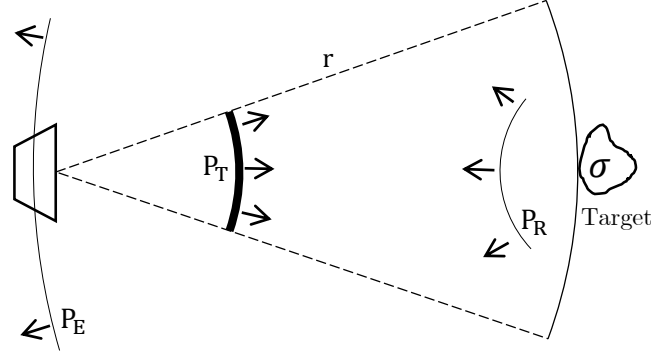


Figure 2.1: Schematic radar principle.

this signal reaches the receiving antenna its energy  $P_E$  can be detected (Figure 2.1). This relationship is described by the *radar Equation* (2.1).

$$P_R = \frac{P_T \cdot G^2 \cdot \lambda^2 \cdot \sigma}{64 \cdot \pi^3 \cdot r^4 \cdot L_v} \quad (2.1)$$

where  $P_T$  is the transmitted,  $P_R$  is the received power in Watt,  $r$  is the distance between the transmitter/receiver and the target in meters,  $G$  describes the characteristic gain factor of the receiving and transmitting antenna,  $\lambda$  is the utilized wavelength in meter and  $\sigma$  is the target back-scatter cross-section in square-meter. The system losses are summarized in a dimensionless factor  $L_v$ .

By measuring the time difference  $\Delta t$  between the transmission and the receiving of the pulse, the distance to the target  $r$  can be obtained by multiplying it with the speed of light  $c$ :

$$r = \frac{c \cdot \Delta t}{2} \quad (2.2)$$

### 2.1.2 Common Wavelengths

The main factors to increase the effectiveness of a radar system as described in 2.1.1, given a constant target size  $\sigma$ , target distance  $r$  and antennas gain, are to increase the transmitted power  $P_T$  or the wavelength.

While the antenna sizes and transmitting power are often limited by external requirements, such as available resources on a satellite, the possible wavelengths are given by the atmospheric electromagnetic opacity and the target features. In Figure, 2.2 this transparency for electromagnetic waves is plotted over the wavelength. One can see that the capability of electromagnetic waves to reach the earth's surface is not a simple function of the wavelength. This penetration depth comes from the superposition of different gas absorption spectra, such as  $N_2$ ,  $O_2$ ,  $O_3$ ,  $CO_2$  and  $H_2O$ . Figure 2.2 also explains why most day active land animals, including humans, developed sensitive eyes in the *visible* 350 nm – 750 nm window as most of the sun's black body radiation can reach the surface. Besides this *visible-notch* and a few near and far infrared bands, the atmosphere is opaque up until millimeter wavelength. Here starts the so called radio window that becomes fully transparent to electromagnetic waves in the centimeter range. Those microwaves are therefore used for long-distance radar systems.



The utilized wavelength are in between 1 cm and 1 m, which is in the range of 26 GHz to 300 MHz of the electromagnetic spectrum. Traditionally, this frequency range is divided into bands with the specific name scheme shown in Table 2.1.

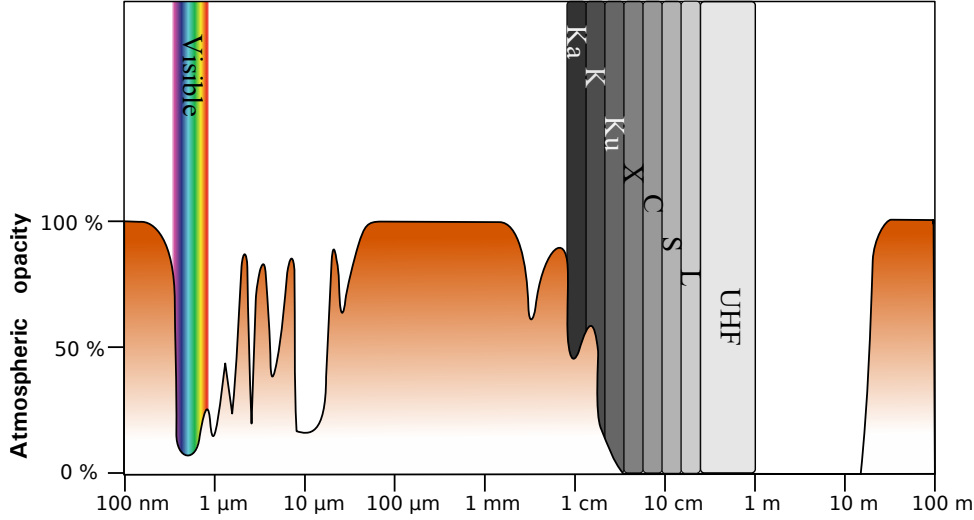


Figure 2.2: Atmospheric electromagnetic opacity (after Rüeger, 1996). Most remote sensing systems operate in one of the transparent windows.

radar Band	Frequency (GHz)	Wavelength (cm)
$K_a$	27–40	1.1–0.75
K	18 - 27	1.7–1.1
$K_u$	12–18	2.4–1.7
X	8–12	3.75–2.4
C	4–8	7.5–3.75
S	2–4	15–7.5
L	1–2	30–15
UHF/P	1–0.3	100–30

Table 2.1: Band names, frequencies, and wavelengths common in radar systems (IEEE, 1984).

The choice of the above wavelengths strongly affects what size of objects the radar is sensitive to. Generally, a radar system can detect objects of about the same spatial magnitude as the wavelength of the radar, and larger. Objects significantly smaller than the used wavelength, become transparent to the radar, although they cause certain damping of the transmitted signal. The smaller the objects, the less influence on the backscatter. The backscatter of objects is thus another factor when choosing the wavelength of a system. The factors that influence the backscattering will be discussed in the next subsection.

For terrestrial systems, such as small automotive radars, the K-Bands are a common choice due to the small antenna size and high possible bandwidths, which results in a high range accuracy (Gromek et al., 2021). For such systems, the attenuation of the atmosphere is actually desirable, because it suppresses the cross-talk between hundreds of users in the same area.

For space- and airborne systems with a long-range, the fully transparent window has to be used. The bands have to be chosen according to the desired objects to observe. If small objects like foliage, facade

structures or delicate details like the fan blades of a jet engine are of interest, short wavelengths like X-Band and C-Band are used (Zhang et al., 2017).

In earth observation longer wavelengths, such as S-Band and L-Band have the advantage that they do not interact with the canopy of a forest and are characterized by a large penetration depth. They can also pass through other volume scatterers, like vegetation, ice, dry soil, and sand. With interferometric applications in mind (see Sec.2.1.7), longer wavelengths offer the advantage of a greatly improved temporal coherence, important for repeat-pass interferometry. On the other hand, long wavelengths have one major disadvantage: generally the phase component of a received signal can be roughly estimated with a few degrees of accuracy. In SAR interferometry, the accuracy is therefore proportional to the wavelength. Hence, a shorter wavelength results in higher accuracy and sensitivity of the deformation measurements. For large scale interferometry applications, bigger wavelengths offer the advantage that even on vegetated areas a coherent signal can be obtained. However, shorter wavelengths such as X-band can be used in densely populated areas that show a high density of man made objects with good scatterer characteristics. The analysis and methods carried out in this work are mainly based on X-band SAR products from the German SAR satellite TerraSAR-X.

An overview of the wavelength used by common space-born SAR missions is given in Table A1.

### 2.1.3 Scattering Properties

The backscattering property of a surface or a material depends on its geometrical surface structure. The most important material characteristic is its dielectric properties which can be quantified by the material-specific dielectric constant. This value describes the relative permeability of a material expressed as a ratio to the vacuum's. This relative permeability is wavelength depended but does not vary much over the common radar spectrum. A low dielectric constant (close to 1) results in a pure transmission of the signal. In other words: this material is mainly transparent for electromagnetic waves of this wavelength. A high permeability leads to a certain part of the energy being reflected from the surface. In Table 2.2, an overview for a few relevant materials is given.

Material	relative permittivity $\epsilon_r$
Air	1
Metal	$\infty$
Dry Masonry	3-5
Moist Masonry	5-26
Dry Concrete	5-8
Moist Concrete	8-16
Asphalt	3-5
Granite	5-7
Dry Sand/Clay	4-8
Wet Sand/Clay	16-32
Ice	3-5
Water	81

Table 2.2: Relative permeability of different material at a frequency of 1 GHz (L-band) (Meyer et al., 2008).

The roughness of a surface has a great effect on the scattering direction of the electromagnetic waves and therefore on the received signal of a sensor. To determine this property, the wavelength has to be considered. Figure 2.3 shows three cases (Peake and Oliver, 1971): on a smooth surface, the incoming rays are reflected like on a mirror according to the Fresnel equations (i.e. the incident ray, the reflected ray, and the normal to the reflection surface at the point of the incidence lie in the same plane). Smooth surfaces like streets,

calm water bodies, and facades do not scatter back a significant amount of the signal, but rather redirect it and are therefore not visible under large incidence angles. On a rough surface, the incoming ray is diffuse reflected. The reflectance for such a Lambertian surface to an observer (receiver) is the same regardless of the view angle of the observer and provides a similar cross-section for all incidence angles. On an intermediate surface that can be described as a combination of the previous, a dominant specular reflection that can be approximated with the Fresnel law and Lambertian proportion occurs. The rays show an omnidirectional, diffuse scattering. This intermediate model describes most surfaces. The diffuse reflection can be detected from various incidence angles, but a right-angled beam leads to strong backscattering.

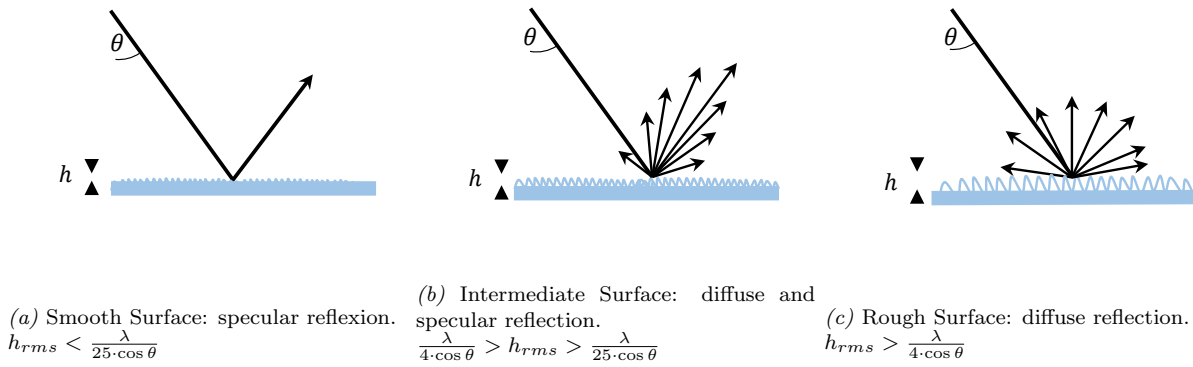


Figure 2.3: Reflection on surfaces. Depending on the mean surface height differences  $h_{rms}$  and the wavelength  $\lambda$ , the incidence angle  $\theta$ , the reflection varies between diffuse and specular (after Peake and Oliver (1971)).

Since the common wavelengths for radar systems vary in the order of 2 magnitudes (Table 2.1), the mean surface height differences  $h_{rms}$  for intermediate surfaces for a X-Band system are only  $h_{rms} = 0.2 - 1$  cm, while they lay in between 5 – 30 cm for an UHF system. This shows how the appearance of surfaces varies with the utilized wavelength in practice.

In addition to the surface properties, the geometry of an object also plays a role in backscattering. The rectangular arrangement of smooth surfaces causes a beam to be reflected back in the direction of the angle of incidence. When two or three intersecting smooth planes are arranged at an angle of 90 degrees to each other, its called a dihedral or trihedral corner reflector (see Figures 2.4a and 2.4b). The perpendicular arrangement results in a double or triple reflection towards the transmitter. This perpendicular arrangement can lead to very strong signal responses. In urban areas, a large number of artificial metal objects that contain rectangular features, like buildings, vehicles and masts leads to an accumulation of dominant scatterers. Typically, targets of such kind are the cause for the later discussed Persistent Scatterer (PS). Volume scattering can be observed if microwave radiation penetrates a medium and is reflected by multiple small elements in all directions (see Figure 2.4c). The narrow branches in vegetation (e.g. grass, bushes, and especially trees) lead to this effect. It can also be observed with dry snow and sand. The volume scatter process can be considered as not deterministic. Through small changes e.g. in the foliage the signal is reflected differently every time.

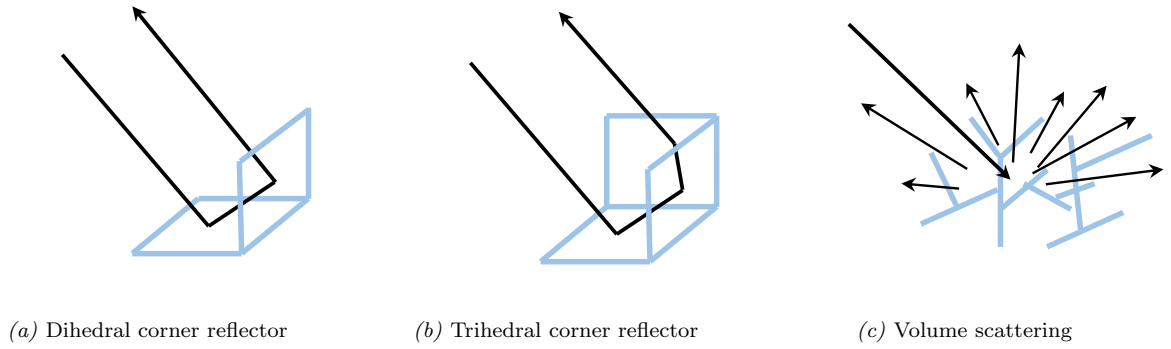


Figure 2.4: Backscattering on corner reflectors and in volumes.

In earth observation, the previously described effects make clear that the actual radar cross-section and thus the backscattered energy depends on various material and geometrical properties of a landscape. Figure 2.5 shows the experimentally determined relationship between this cross-section parameter  $\sigma$  and the incidence angle for different artificial and naturally occurring land cover classes. Terrain covered by industrial, commercial, and residential areas shows a significantly higher reflection coefficient than that covered by vegetation or bare soil and sand. This property makes clear that buildings in cities and infrastructure elements such as rails and pipelines are predestined for observation with radar techniques and explains why PSI is especially well suited for built-up land.

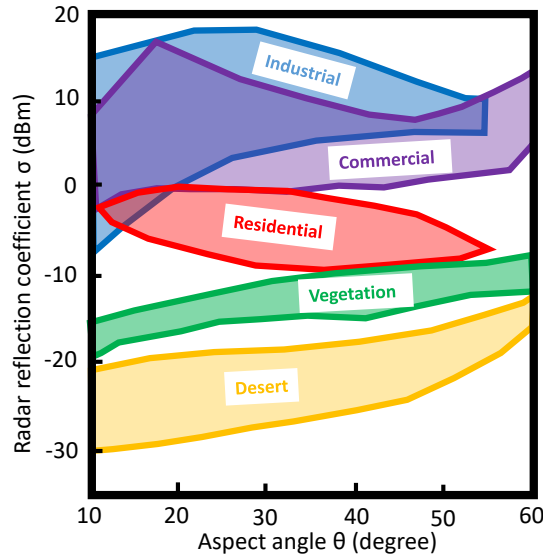


Figure 2.5: Relations between radar reflection coefficients, aspect angles of an X-band radar pulse, and terrain characteristics (after Newbry, 1960).

### 2.1.4 Resolution of Side Looking Real Aperture Radar Systems

The basic radar principle, as described in 2.1.1, is known for a century and has continuously been improved since. It has applications in various near and far-range sensing devices. If a radar system is mounted on the side of air or space-borne vehicle, slanted to the ground with an angle, it is called a side-looking real aperture radar. In the following subsection the resolution limits for a side-looking, radar are discussed. This explains the basics and the needs for the later described Synthetic Aperture Radar (SAR).

It is necessary to distinguish between two resolutions: the ground-range resolution away from the satellite and the azimuth resolution or swath width which refers to the strip of the Earth's surface from which data is collected by a side-looking radar (see Figure 2.6).

In its simplest form, the ground-range resolution  $\delta_r$  defines the ability to distinguish between scatterers in the ground-range direction:

$$\delta_r = \frac{c \cdot \tau}{2 \sin \theta} \quad (2.3)$$

$\delta_r$  depends on  $c$ , the speed of light,  $\tau$  the pulse duration of the transmitter, and  $\theta$  the incidence angle (see Figure 2.6).

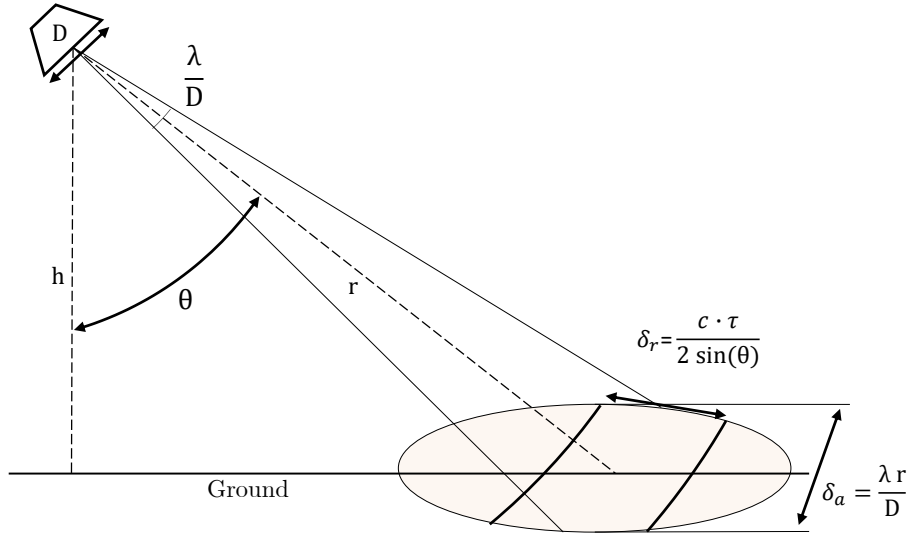


Figure 2.6: Ground-range resolution  $\delta_r$  depends on the pulse length  $\tau$ , respectively the bandwidth  $B$ . Azimuth resolution  $\delta_a$  is limited by antenna size  $D$  and wavelength  $\lambda$ .

Because  $\tau$  cannot be arbitrarily short, due to the resulting height power spike that would damage the transmitting systems, a signal processing trick is performed: instead of a short pulse, a rather long, linear frequency modulated ramp or *Chirp* is transmitted. By convolution of the received signal with this matched filter, objects can be resolved as if a short pulse was used. The bandwidth is roughly proportional to the

amount of information carried by the signal. To detect a rectangle pulse with the fast Fourier transformation (FFT) the bandwidth of the receiver is equal to the highest sine wave frequency component that is significant. A larger bandwidth of the receiver results in a shorter the rise time of the edges of the rectangular pulse. The bandwidth  $B$  and the pulse duration  $\tau$  are reciprocal:

$$B = \frac{1}{\tau}. \quad (2.4)$$

Instead of the pulse length, a radar system can be characterized by its bandwidth  $B$ . If the bandwidth is known, the physical maximum for the ground-range resolution can be derived. In Table A1 an overview of different SAR-satellite systems along with their bandwidth is given. For an exemplary system that has a bandwidth of 300 MHz, the terms in Eq. (2.3) and Eq. (2.4) give a maximum ground-range resolution of  $\delta r \approx 0.4$  m.

In contrast to the above-described range resolution, the swath width of a real aperture radar can not be enhanced by signal design. The swath width or azimuth resolution  $\delta_a$  describes the width of the beam that illuminates the earth. The echo of two objects can only be distinguished if the beam width is smaller than this. It can be approximated by the Rayleigh criterion:

$$\delta_a = \frac{\lambda \cdot r}{D}, \quad (2.5)$$

where  $r$  is the target distance,  $\lambda$  is the utilized wavelength and  $D$  is the length of the antenna. For common radar wavelength (e.g. X-band) and target distances of a few hundred kilometers, the antenna length needs to be in the order of dozens of kilometers to achieve an azimuth resolution in the order of meters.

To overcome this technical limitation of a real aperture radar and to achieve practical azimuth resolutions, synthetic apertures have to be used.

### 2.1.5 The Synthetic Aperture Radar Principle

In comparison to a real aperture radar system, the azimuth resolution is substantially improved by the Synthetic Aperture Radar (SAR) principle. The idea of a SAR is to simulate a large antenna by making several measurements at different locations and times. The measurements can then be combined in a post-processing step named focusing. This principle has been known for many decades (Wiley, 1954) but the wide adoption of SAR came along with the progress in digital signal storage and processing. This has led to many different earth observing systems in the last decades and opened the door for relatively cheap to manufacture and to operate satellite constellations that will continuously monitor our planet in the future. Moreira et al. (2013) give an overview of the history, principles, and challenges of current and future space-born SAR missions.

In the following section, the basic principle of a Synthetic Aperture Radar (SAR) is shortly explained, so the understanding of the further interferometry processing is facilitated. The imaging properties and geometry, especially the distortions are briefly discussed.

To overcome the limitations of real aperture described by Equation (2.5), the SAR system illuminates the target with repeating impulses in a side looking fashion across the flight track (see Figure 2.7).

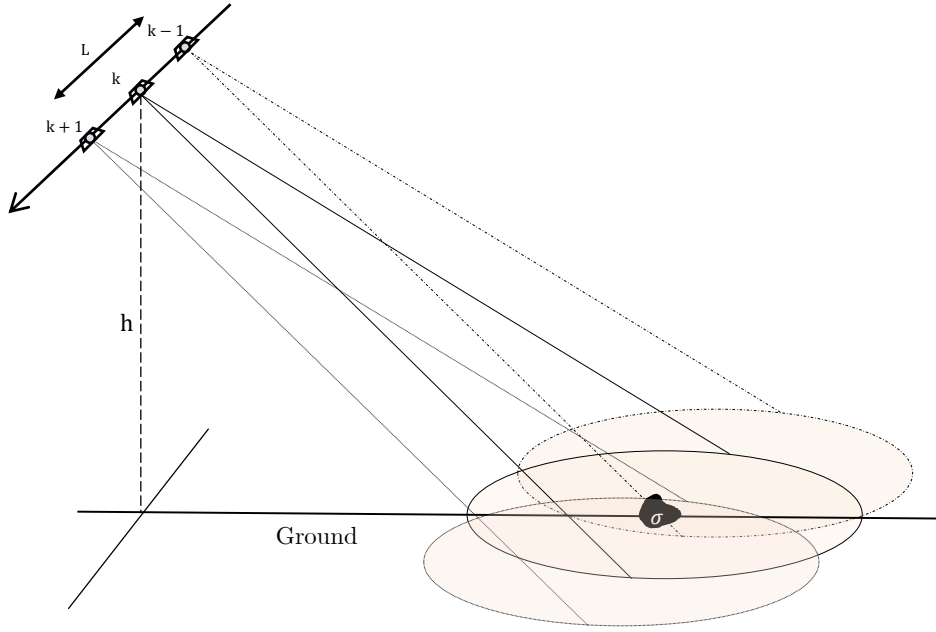


Figure 2.7: Schematic SAR radar Principle. While moving along the synthetic aperture  $L$  the radar sends out a sequence of pulses, illuminating the target  $\sigma$ . The received signals can be combined, enabling the kilometers long synthetic antenna, that is needed for a azimuth resolution in the order of meters.

For each position the received signal gets saved in the columns of an array, thereby each row of the array represents a step in time. By correlating each column with the matched filter, the targets can be distinguished in range direction. This process is analog to real aperture radar systems and called *range compression*.

Since the range to the center of the antenna footprint and the effective satellite velocity along with the pulse repetition frequency (PRF) is known, a matched filter otherwise known as azimuth chirp, can be computed from the original chirp. By correlating each row of the range compressed signal array with this azimuth chirp, the azimuth direction is focused. Hereby the so-called range doppler migration has to be compensated.

The final product of the focusing process is a SAR image, with complex values for each pixel. This means that for each resolution cell not only the amplitude of the reflected signal is known but also the phase is measured. The fact that the coherent SAR system reproduces the same measurement of the phase of the reflected signal (if none of the external influences change) is exploited in Interferometric Synthetic Aperture Radar (InSAR) (see Sec. 2.1.7).

The azimuth resolution  $\delta_{sa}$  for a SAR can be approximated by:

$$\delta_{sa} \approx \frac{\lambda \cdot r}{2 \cdot L} \approx \frac{D}{2} \quad (2.6)$$

which is remarkably independent of the range. Equation (2.6) also shows that the resolution can be improved by increasing the synthetic aperture length  $L$  or decreasing the size of the real aperture  $D$ . In

reality the length of the synthetic aperture can not be infinite and the size of  $D$  has to be reasonable (typical a few meters for satellites) to achieve a significant gain.

### 2.1.5.1 Acquisition modes

Modern SAR-systems can be used in different acquisition modes. This gives the user the possibility to vary between wide area captures with a low resolution and small area acquisition with a high resolution. Beam steering can be achieved with phased array antennas (Ossowska, 2015). This may be accomplished by switching the antenna elements changing the relative phases of the signals and allows changing the azimuth and elevation angle of the main lobe of a radiation pattern with no physical movement of the antenna. Figure 2.8 shows the three most common acquisition modes for space-born SAR systems.

**Stripmap-SAR** Stripmap-SAR is the standard procedure. The antenna pattern is not swivelled in the cross-track or range area. The swath is parallel to the ground track (projection of the flight path onto the earth's surface).

**Scan-SAR** Scan-SAR makes use of the agility of an active array antenna by scanning several strips at different distances and azimuth angles virtually simultaneously according to a sophisticated sequence plan. This wide area mode usually achieves a lower azimuth resolution resolution as the single synthetic apertures become shorter.

**Spotlight-SAR** In this SAR method, the azimuth resolution is improved compared to the limitations (antenna size and swath width) specified in the classic strip-map mode by keeping the antenna pointed at a specific target area (spot) for a longer period of time by rotating the azimuth accordingly. This increases the time-bandwidth product and consequently improves the achievable resolution. However, this happens at the expense of the total imageable area, as the next spot can only be targeted at a distance determined by the observation time and the flight speed.

For small areas of interest like cities the trade off between total area and resolution is acceptable. In this research we mainly use this kind of data. Typical Spotlight images from systems like TerraSAR-X have an overall size of  $4\text{ km} \times 5\text{ km}$  and a ground sampling distance (GSD) of approximately  $1\text{ m} \times 1\text{ m}$ .

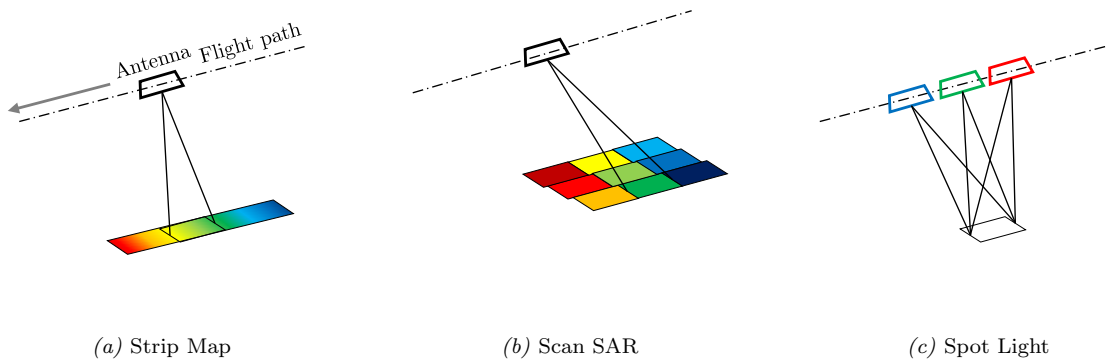


Figure 2.8: Modern space-born SAR systems can use beam steering to capture either a wide area with low resolution or a small area with a high azimuth resolution.



### 2.1.5.2 SAR Satellite Orbits and Acquisition Geometry

The SAR satellite is usually on a sun-synchronous orbit. Such an orbit has an inclination angle between  $95^\circ$  and  $100^\circ$  and is therefore close to a polar orbit. The north-to-south half circle is called the *descending track* or *descending orbit*, while the south-to-north half is called *ascending track* or *ascending orbit*. The observation of the same area from ascending and descending direction is common in InSAR since it allows to measure a deformation from two different line-of-sight (LOS). For common flight heights of low-earth satellites of approximately 1000 km it takes  $\approx 90$  min to complete one full orbit.

Repeat orbits play a big role in Interferometric Synthetic Aperture Radar (InSAR). A repeat orbit time is a duration for a satellite to be above the exact same point on earth. This can be controlled by carefully chosen orbit parameters that have to be continuously measured and actively controlled (Fu et al., 2012; Yamamoto et al., 2013). The fuel that is used to control the orbit and the attitude of the satellite is often the limiting factor for the duration of a SAR mission. Typical repeat orbits for SAR satellites are 10-30 days. But they can be much shorter if constellations of several satellites with individual sensors are used jointly (see Tab. A1).

For the illumination geometry of the earth's surface by a SAR satellite, several terms have been established over time. Figure 2.9 explains a few of this terms schematically.

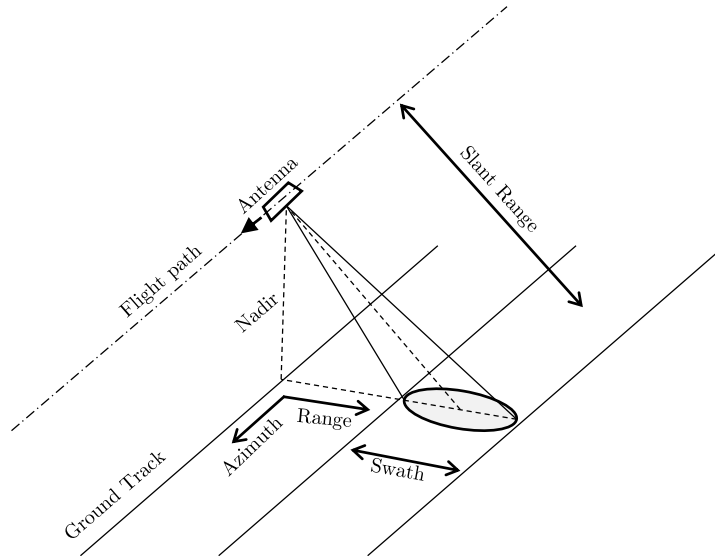


Figure 2.9: Schematic SAR radar geometry. Slant range is the length between the antenna and a ground pixel. The ground range is the distance between the ground track and a ground pixel. The swath is the area that is illuminated by the satellite at one time. Range and azimuth always refer to the direction away from the satellite, respectively in flight direction.

### 2.1.5.3 Perspective Properties of SAR Images

The imaging geometry of SAR images is different from that of optical images, like those captured by a frame camera or our eyes. In complex scenes like cities, distortion and perspective effects can make it difficult to interpret a SAR image. In the following, slant-range projection and the distortion cases are discussed.

In Figure 2.10a the normal case of SAR acquisition geometry is depicted: all points  $A$ ,  $B$  and  $C$  are projected onto the slant range  $A'$ ,  $B'$  and  $C'$ . In Figure 2.10b, a small hill is shown with an elevated point  $B$ . The slope between  $A$  and  $B$  is significantly shorter in the  $A' - B'$  projection, compared to the  $B' - C'$  distance. This effect is called foreshortening and can often be observed on hills and mountain slopes. Figure 2.10c illustrates the effect of layover. This ambiguity occurs on hills with a slope greater than the incidence angle. It also prominently appears on the walls of buildings that seem to lay toward the satellite. Note that the interval between  $A$  and  $B$  is projected into the same area as  $B$  to  $C$ . Since the SAR sensor is observing the scene in a side-looking manner, it can not see behind steep slopes or buildings. This shadowing effect is shown in Figure 2.10d. In the case of dense urban areas, only the facades towards the sensor can be imaged.

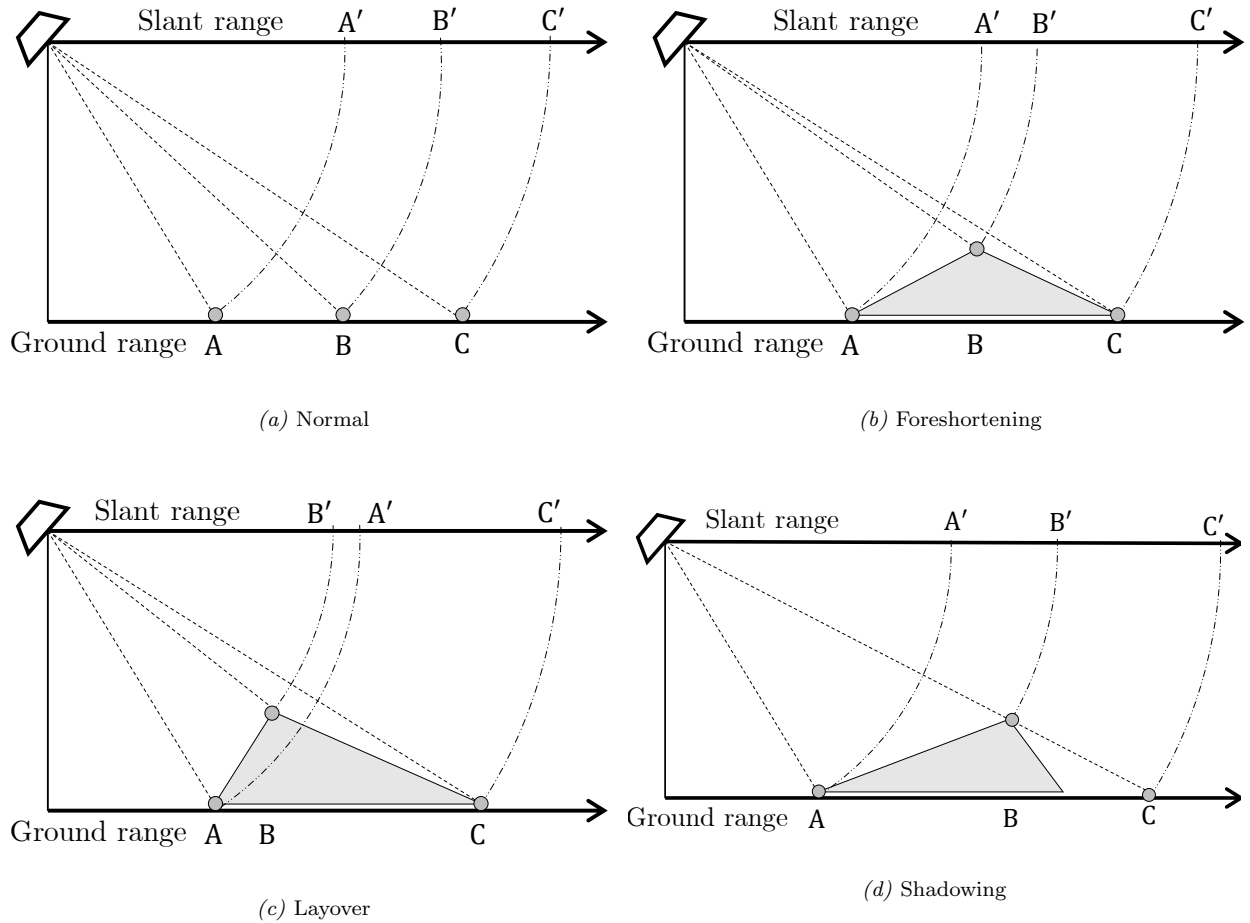


Figure 2.10: Slant Range Distortion

In Chapter 4, we deal with SAR images that show urban scenes with many buildings. To interpret such images the layover effect needs to be considered.

### 2.1.6 Geocoding of SAR Images

The SAR geocoding approach uses the satellite orbit, local terrain information, and SAR image processing parameters to calculate a lookup table. This table gives the SAR image coordinates for each point in the geocoded image geometry. The geographic coordinates can either be latitude and longitude, or the northing and easting of a particular map projection. This mapping from the geocoding is unique in the sense that every point in the map coordinates corresponds to a unique range and azimuth SAR image coordinates. The inverse transformation is not unique because SAR image layover causes a single point in the radar image to map to several points in the map projection coordinates (Johnsen et al., 1995; Wegmuller, 1999; Werner et al., 2002). Calculation of the lookup table digital elevation model (DEM) as input. The DEM is resampled first into the desired output projection and sample spacing. The precise slant range and sensor along-track positions are then calculated for every point of the resampled DEM coordinates. The lookup tables are then used to generate the geocoded, georeferenced SAR image that can be overlaid with a map.

Efficient geocoding is implemented in several SAR processing software packages. In Figure 2.11 the principle of SAR geocoding is schematically depicted.

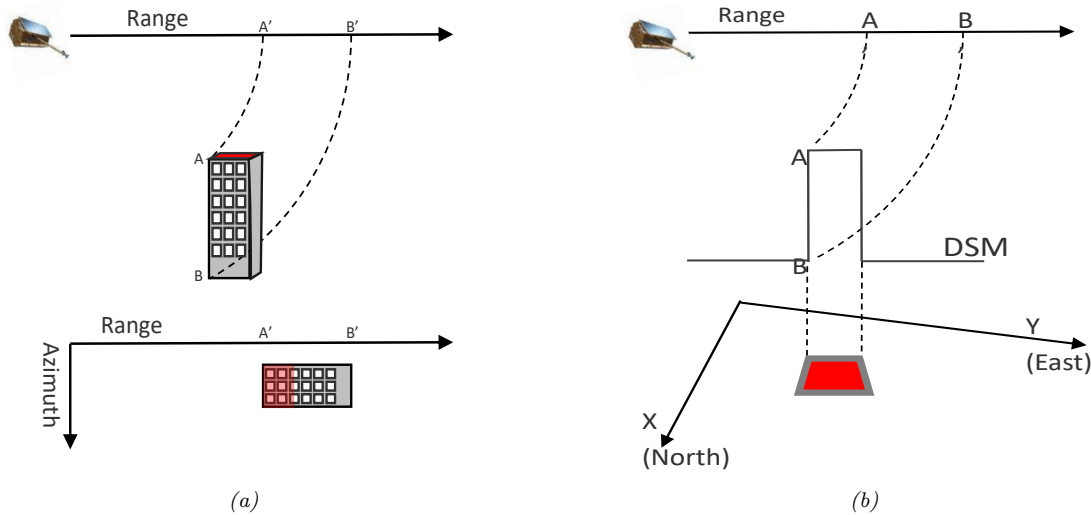


Figure 2.11: (a) Range-Azimuth imaging geometry. (b) If the exact orbit parameters of the satellite are known, each Range-Azimuth cell can be assigned to a geo-coordinate with the help of a precise digital surface model (DSM).

This principle can also be used to geocode other SAR products like interferograms or PS points to a common coordinate system. It is an important step in the PSI processing chain. Without geocoding the PS points it would be not possible to combine them with data from other sources.

### 2.1.7 Interferometric Synthetic Aperture Radar

In Interferometric Synthetic Aperture Radar (InSAR) the phase differences between two SAR images are evaluated. It is necessary that the two images have to be captured roughly from the same position in space.

For some applications like DSM generation a small cross-track baseline of several dozen, up to a few hundred meters is needed. There are two possibilities to achieve this configuration. In single pass interferometry, the two sensors are flown close to each other and scan the surface at the same time. This can be either done by distancing one antenna from the other with a long boom, as it was done by the Shuttle Radar Topography Mission (SRTM) (Rosen et al., 2000; Farr and Kobrick, 2000; Kobrick, 2006; Farr et al., 2007) or by flying two satellite platforms with identical sensors very close to each other on a helical orbit. This principle is prominently used with the TanDEM-X Mission (Krieger et al., 2007a, 2010). The second possibility to achieve this acquisition configuration is repeat pass orbit. By choosing the orbit parameters of a satellite, its ground track can be influenced. When the ground track reaches the same position on earth, is a trade-off between spatial and temporal resolution (Fu et al., 2012). This so-called repeat cycle is chosen carefully for every mission (see Table A1) but is usually in the order of 1-2 weeks. Precise orbit determination and control are therefore necessary for every InSAR capable satellite mission (Aorpmimai and Palmer, 2007). Several missions fly constellations of two or more satellites with identical sensors on the same orbit, but with a time delay of few days. This allows for a finer temporal resolution (short repeat cycle) while having the same ground track density (spatial resolution).

If both images are acquired at the same time, no temporal decorrelation on dynamic surfaces like vegetation and snow-covered landscapes can occur. This is the reason why single-track interferometry is preferably used for DEM generation.

In the following, the InSAR principle is briefly summarized. It applies to both, single pass and repeat pass interferometry but for the repeat pass has to be considered which is a factor 2 in the formulas. The following considerations help to understand advanced methods.

For the first SAR image (commonly referred to as the master image), acquired from the satellite's position  $M$  at the measured phase  $\phi_M$  of a single pixel, covering a target  $\sigma$  on the ground, can be modeled by:

$$\phi_M = \phi_{geom-M} + \phi_{scatt-M} \quad (2.7)$$

$$= \frac{4^1 \cdot \pi \cdot R_M}{\lambda} + \phi_{scatt-M} \quad (2.8)$$

where  $R_M$  is the distance from the satellite to the pixel on the ground,  $\phi_{scatt-M}$  is the scattering phase shift when the signal interacts with the target  $\sigma$  and  $\lambda$  is the utilized radar wavelength and the constant factor  $4^1 \cdot \pi$  models the multiple full phase turns on the two-way path.

For a second image acquired by the same sensor (the so-called slave image) from the position  $S$  a similar relationship can be established:

$$\phi_S = \phi_{geom-S} + \phi_{scatt-S} \quad (2.9)$$

$$= \frac{4^1 \cdot \pi \cdot R_S}{\lambda} + \phi_{scatt-S} \quad (2.10)$$

The interferometric phase  $\Delta\phi_{int}$  is given by the difference  $\phi_S - \phi_M$ :

$$\Delta\phi_{int} = \phi_S - \phi_M \quad (2.11)$$

$$= \frac{4^1 \cdot \pi \cdot R_S}{\lambda} + \phi_{scatt-S} - \frac{4 \cdot \pi \cdot R_M}{\lambda} - \phi_{scatt-M} \quad (2.12)$$

if the incidence angle and azimuth, respectively the sensor's position between both acquisitions is very similar it can be assumed that the scattering phase shift  $\phi_{scatt}$  of the same target is equal for both images. In this case the interferometric phase simplifies to:

$$\Delta\phi_{int} = \frac{4^1 \cdot \pi \cdot}{\lambda} \cdot (R_S - R_M) \quad (2.13)$$

---

<sup>1</sup>The constant 4 applies for repeat pass only. For single pass it is a factor of 2.

or

$$\Delta\phi_{int} = \frac{4\pi}{\lambda} \cdot \Delta r \quad (2.14)$$

and is proportional to the target-position distance difference between both acquisitions  $R_S - R_M$  respectively  $\Delta r$ , which is fundamental for DSMs generation, e.g. to estimate the topography of the observed scene (Bamler and Hartl, 1998). The sensitivity to topography depends on the perpendicular projection of the baseline  $B$  or  $\overline{SM}$  onto the LOS which is depicted with  $B_\perp$  in Figure 2.12. The relation between  $\Delta\phi$  and  $\Delta r$  depends on  $\lambda$ . The phase measurements and therefore also the determination of  $\Delta\phi$  can be made with a degree level of accuracy. For common wavelengths in space-borne SAR systems (see Table 2.1), this corresponds to a millimeter accuracy. The bigger this wavelength, the more accurate  $\Delta r$  can be obtained.

The geometrical relationship between the terrain height  $h_0$  of the target, the master satellites orbit height  $H$ , and the distance to the target  $\sigma$  is shown in Figure 2.12. For DSM generation, the unknown  $h_0$  has to be found. The cosine theorem leads to the following relationship:

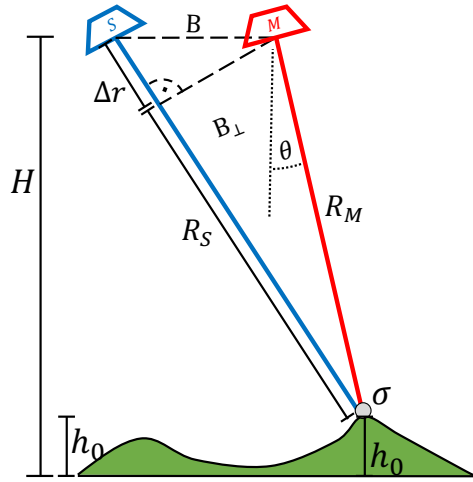


Figure 2.12: Geometrical configuration of baselines in cross-track InSAR

$$(R_M + \Delta r)^2 = R_S^2 + B^2 - 2R_M B \cos\left(\frac{\pi}{2} + \theta\right) \quad (2.15)$$

which can be solved for the unknown local incidence angle  $\theta$  with the following:

$$\sin(\theta) = \frac{(R_M + \Delta r)^2 - (R_S^2 - B^2)}{2R_M B} \quad (2.16)$$

The unknown local height  $h_0$  can be set in trigonometric relationship with the LOS distance to the master image's acquisition position  $R_M$  and the orbital height  $H$ :

$$h_0 = H - (R_M + \Delta r) \cdot \cos(\theta) . \quad (2.17)$$

The three non-linear equations (2.14), (2.16) and (2.17) can be combined to calculate  $\theta$ ,  $\Delta r$  and  $h_0$  for each pixel of the interferogram.

### 2.1.8 Differential Interferometric Synthetic Aperture Radar

Differential Interferometric Synthetic Aperture Radar (DInSAR) techniques exploit the information from the radar phase of at least two complex SAR images acquired at different times over the same area. The two images always form an interferometric pair or interferogram. By repeatedly acquiring images over the same area with the same sensor system or multiple sensors with the same characteristics, a stack of coherent images can be built up. For a stack of  $N$  images, a large number of interferograms, precisely  $(N - 1)!$ , can be formed and analyzed. Redundant measurements over a long time enable the compensation of atmospheric influence. This principle was initially described by Gabriel et al. (1989) and is still under development. Rosen et al. (2000) give a general review over the development of SAR interferometry.

In the following subsection, the focus will be laid on one class of techniques, namely the Persistent Scatterer Interferometry (PSI).

### 2.1.9 Persistent Scatterer Interferometry

In this section, the basic principles and ideas of Persistent Scatterer Interferometry (PSI) are explained, followed by an overview of the relevant contributions in the last two decades. In the second half, the different commercially available PSI software implementations are listed. In the end, an overview of applications in geophysics, civil engineering, and geodesy is given and the limitations and strengths are discussed.

PSI is a powerful SAR evaluation technique and belongs to the family of DInSAR algorithms. Especially for built-up areas, highly accurate deformation time series can be derived from a stack of coherent SAR images. In contrast to InSAR techniques, which by only analyzing a pair of images and are strongly influenced by the atmosphere and suffer from temporal decorrelation, the PSI technique focuses on the evaluation of single persistent backscatters, that show a coherent signal over time and through out many subsequent SAR images. It is worth mentioning here that the term Persistent Scatterer Interferometry (PSI) commonly describes several similar radar interferometry algorithms that have been developed over time by different commercial and scientific institutions and will be used in the following in exchange for the potentially original names. A review by Crosetto et al. (2016) is available that details the most important contributions to the PSI method. The work points out the valuable inputs for the PSI development and shows examples for the acceptance at scientific, technical, and commercial levels.

**Measuring Principle** In a stack of SAR images (typically more than 20 images), that are taken from the same position in space over a certain time span, some targets in the scene and therefore some pixels can be considered persistent scatterers. The physical scattering of these characteristic pixels stays constant over time and they reflect the radar signal in a deterministic way. The phase difference of all images in the stack relative to a master image is considered. Similar to the InSAR principles described in Sec. 2.1.7, individual factors that have an influence on the measured phase differences  $\Delta\phi$  can be identified:

$$\Delta\phi = \Delta\phi_{FlatEarth} + \Delta\phi_{Topography} + \Delta\phi_{Deformations} + \Delta\phi_{Errors} \quad (2.18)$$

The terms  $\phi_{FlatEarth}$  and  $\phi_{Topography}$  describe the influence on the measured phase due to the earth's surface shape. They are separated into the influence of the ellipsoid and the topography on top of that for processing reasons. The  $\phi_{FlatEarth}$  can be simulated and subtracted relatively easily by assuming a topography free ideal ellipsoid, the topography has to be measured beforehand, either with InSAR or other classic surveying techniques.

The  $\Delta\phi_{Errors}$  term summarizes all kinds of influences such as orbit and positioning errors, atmospheric influence, temporal decorrelation, system noise, and errors in other terms. All of these errors have to be carefully modeled and eliminated, in order to achieve the possibly high accuracies that the PSI technique offers.

The term  $\Delta\phi_{Deformations}$  describes the phase change that is induced by a deformation between the acquisition of two images. Figure 2.13 schematically shows a target  $\sigma$  that moves to the position  $\sigma'$  between the acquisition of the first image  $M$  and the second  $S$ . This movement results in a line-of-sight change in length  $\Delta r$ . It can be related to measured phase difference with the following equation:

$$\Delta r = \Delta\phi_{Deformations} \cdot \frac{\lambda}{4\pi} . \quad (2.19)$$

For a wavelength  $\lambda$  of 3 cm and a phase resolution of  $1^\circ$  Persistent Scatterer Interferometry can detect movements with millimeter accuracy.

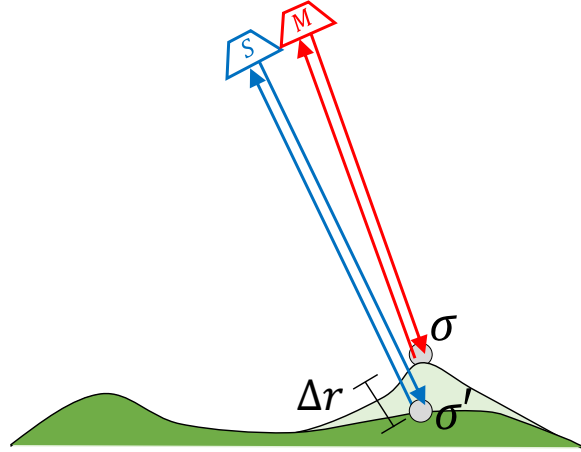


Figure 2.13: By comparing the back scattered phase of a target in consecutive SAR acquisitions, the deformation along the line-of-sight (LOS) of the satellite can be estimated.

**Processing overview** The Persistent Scatterer Interferometry (PSI) approach is a pipeline of a series different processing steps. Several different PSI variants have been described since the original work by Ferretti et al. (2000, 2001). However the following steps always apply generally in all variants:

- **Pre-processing:** The single SAR images have to be co-registered. In case of high Doppler rates, the co-registration needs to be accurate in the order of  $1/1000$  pixels in azimuth. Several authors proposed

a two-step process: a coarse pre-alignment, followed by a fine registration (Scheiber and Moreira, 2000; Prats-Iraola et al., 2012):

(i) Pixel-level co-registration is performed by using orbit information or cross-correlation methods; then

(ii) next, an accuracy refinement is carried out by using the spectral diversity. Unlike conventional co-registration methods, this technique does not need any interpolation or cross-correlation procedures. Furthermore no coherence or fringe optimization must be performed.

After the images are co registered, the optimal master image has to be found. Here the temporal and spatial (perpendicular) baselines have to be considered and it has to be insured that the spectrum of the master image has a maximum overlap with the spectra of all other images.

Finally, the interferograms from the master to all other images can be computed. For  $M$  images, this results in  $M - 1$  interferograms.

- **Selection of the set of Persistent Scatterer (PS) candidates:** In this step, the stack of SAR images is analyzed over time. Potential candidates for PS points are made out, which can be considered in the following processing steps. Commonly the Dispersion of Amplitude (DA) criterion is used for candidate selection, but other PSI algorithms might suggest different methods (see Tab. 2.3). The DA criterion ensures that the PSs are characterized by a moderate spatial phase variation (neighboring pixels) and thus a correct phase unwrapping (Devan      et al., 2014).
- **First phase unwrapping:** The so-called 2 + 1D phase unwrapping is a spatial 2D phase unwrapping. The Minimum Cost Flow method (Costantini et al., 1999) is an example method utilized to obtain the unwrapping. Phase unwrapping is performed over the down-sampled or multi-looked interferograms, so each interferogram has a continuous phase. This spatial phase unwrapping then is followed by a 1D phase unwrapping for each pixel over time in full resolution, so throughout all interferograms.
- **Atmospheric filtering:** Using the unwrapped interferograms, an estimation of the atmospheric and orbital phase screen (APS) is performed using a set of spatio-temporal filters (Berardino et al., 2002; Ferretti et al., 2001). The APSs are then removed from the original interferograms. This is conducted under the assumption, that the atmospheric influence is varying from image to image and can thereby be removed by a low-pass filter. Other approaches try to bring external information about the atmospheric conditions into this step.
- **Inversion:** In this step, the deformation time-series and the Residual Topographic Error (RTE) are estimated using a deformation model. The deformation over time and the RTE are estimated from the wrapped APS-free interferograms. Commonly, a linear model is assumed leaving the unknowns as the velocity and the RTE. An extension of this two-parameter model can be used to account for non linear movements e.g. for thermal expansion (Monserrat et al., 2011; Ogushi et al., 2019, 2021). The RTE phase component is then removed from the wrapped APS-free interferograms. The same operation can be carried out for the deformation component, which then, in a later stage, is added back to the deformation time series. As quality metric the *model coherence* is used. This metric describes how well the deformation model fits the observations.
- **Second phase unwrapping:** Now, the second stage of the 2 + 1D phase unwrapping is performed. This step, which uses the APS- and RTE-free interferograms, generates the final deformation time series for each processed pixel. The time series generation is influenced indirect by the deformation model via the previous step. For PS points with a low model coherence value, the resulting time series might not represent the actual deformation and might just a be model-fit through the observed phases.
- **Geocoding:** The final step is the geocoding of the PSI results. In addition to the classic SAR geocoding and terrain correction based on a DEM and orbit parameters (Johnsen et al., 1995; Wegm     , 1999), the Residual Topographic Error (RTE) can be utilized to achieve an approximate accuracy in the order of the ground pixel extent.



Reference	Pixel selection criterion	Deformation Model
Ferretti et al. (2000, 2001)	Amplitude dispersion (Amp. dis.)	Linear deformation in time
Werner et al. (2003)	Amp. dis. and Spectral phase diversity	Linear deformation in time
Hooper et al. (2004)	Amplitude and phase criterion	Spatial smoothness
Kampes (2006)	Amp. dis. and Signal to clutter ratio	Various types of deformation models
Costantini et al. (2008)	Amplitude dispersion	Linear deformation in time
Ferretti et al. (2011)	Single master after triangulation	Linear deformation in time
Van Leijen (2014)	Amplitude dispersion	Various types of deformation models
Lv et al. (2014)	Statistical homogeneity test	Linear deformation in time

Table 2.3: Overview of important PSI algorithms over the last two decades. They mainly differ in the pixel selection criterion and the used deformation model.

**The history of PS Algorithms** The pioneering work by Ferretti et al. (2000, 2001) described the first PSI technique. Their specific algorithm was patented and led to a spin-off company created by Politecnico di Milano named Tele-Rilevamento Europa ([www.treuropa.com](http://www.treuropa.com)). The first commercial implementation of PSI was named PSInSAR™. Later the original algorithm from Ferretti et al. was implemented by SARmap ([www.sarmap.ch](http://www.sarmap.ch)) in the software packet SARscape which is an add-on for ENVI. The approach of Ferretti et al. is surely the most important. It presented the first complete pipeline for the PS selection, including the temporal and geometrical decorrelation, and the estimated deformation and position by separating the signal from the APS and RTE. It represented a significant improvement over previous DInSAR techniques and led to countless new applications for the PSI technology, especially in urban contexts.

In the years followed by the first PSI algorithm, several other contributions suggested improvements or slight changes from the original algorithm, also to differentiate themselves from the original patent (See Table 2.3). Werner et al. (2003) introduced the Interferometric Point Target Analysis (IPTA) method that analyzed the spectral phase diversity as a pixel selection criterion. This led to another commercial implementation by Gamma Remote Sensing ([www.gamma-rs.ch](http://www.gamma-rs.ch)). Kampes and Hanssen (2004); Kampes (2006) improved the unwrapping network by adapting the Least-squares AMBIGUITY Decorrelation Adjustment (LAMBDA) method from GPS processing and suggested to use the signal-to-clutter ratio as a selection criterion along with a non-linear deformation model. Hooper et al. (2004) proposed a novel PS candidate selection based on a phase criterion rather than on the amplitude like the previous implementations. This work developed into one of the most widely used software packets Stanford Method for Persistent Scatterers (StaMPS) (Hooper and Zebker, 2007; Hooper, 2008). Crosetto et al. (2005) described a simplified PSI approach based on step-wise linear deformation functions and least squares adjustment. Costantini et al. (2008, 2014) proposed a PSI method that only exploits the relative properties of neighboring pairs of Persistent Scatterers. Ferretti et al. (2011) proposed an extension of their original PSInSAR™ algorithm called the SqueeSAR™ algorithm by jointly processing PSs and Distributed Scatterers (DSs) taking into account their different statistical behavior. The results of the SqueeSAR™ method is an improved quality and density of PS points, especially in non-urban areas. A similar PSI approach that also exploits the coherence information of neighboring pixel stacks was proposed by Lv et al. (2014) and Goel and Adam (2013).

Since the estimation of the unknown atmospheric phase component (See Eq. (2.18)) is a crucial step in all PSI processing methods, several groups have developed different approaches to predict the APS from additional measurements. Leighton (2010); Catalão et al. (2011); Fornaro et al. (2014); Alshawaf et al. (2015) were analyzing the phase-delay of Global Navigation Satellite System (GNSS) signals to construct accurate maps of the atmospheric water vapor. While Liu (2012); Jung et al. (2013) use numerical weather forecasting models to predict such atmospheric phase delay effects and use them in the PSI processing.

Another aspect of the PSI processing chain, that influences the quality of the results, is the underlying deformation model. If the cause of the deformation process is known, a suitable model has to be chosen. Van Leijen and Hanssen (2007) described the use of adaptive deformation models to increase PS density.

Colesanti et al. (2003) proposed an extension of the PSInSAR<sup>TM</sup> to monitor seasonal ground deformation phenomena. A similar approach was used to model the displacements caused by thermal expansion by Gernhardt et al. (2010). A more accurate model for thermal expansion is described in Monserrat et al. (2011). Most recently Ogushi et al. (2019, 2021) implemented a non-linear non-parametric approach which showed robustness for general displacement monitoring.

#### 2.1.9.1 Limitations of PSI

PSI has certain limitations that should be considered before it is used for deformation analysis.

**Line of Sight** The only part of a movement that can be measured is a projection onto the line-of-sight (LOS) of the satellite, or in other words the motion towards or away from the satellite. Therefore under certain conditions, movements such as landslides cannot be detected if they occur perpendicular to this direction. Theoretically, this can be countered by using several observation directions. However, the polar orbit configuration limits this to an east-to-west and a west-to-east observation and therefore the full three-dimensional movement can not be resolved. In practice, most relevant deformations are gravitational induced, and therefore up-down movements. For a known movement directions one observation direction is often sufficient.

**Number of Images** The minimum number of SAR images for a PSI analysis is 15 - 20 (Crosetto et al., 2016). The usual repeat orbit for common satellites is one to two weeks (Table A1). Therefore, a PSI analysis can only be performed several months after the first image acquisition. One possibility to overcome this is to scan all potentially interesting areas in advance so that images from the archive can be analyzed up to the target date, if necessary. The Sentinel-1 mission does this globally with a GSD of  $20\text{ m} \times 5\text{ m}$ . For a limited amount of smaller areas of high interest, like major cities, high-resolution data can be captured in advance and is available in archives.

**Temporal Coherence** The PSI method only deliver results for areas that show a temporal coherent scattering behavior. It is a opportunistic method, meaning that before a PSI analysis is completed it is difficult to predict where PS points will be located in the result. This is especially the case for medium-resolution data. Even in urban scenes, it cannot be assumed that a resolution cell will show a stable backscattering behavior over time. For high-resolution data, it can generally be assumed that man-made structures have a high density of Persistent Scatterer.

**Fast Changes** Only long-term deformation that happens over the course of several acquisitions can be detected. Especially fast changes like quick jumps can not be detected as they can be seen during the rupture of earthquakes. No valid PS points can be detected for surfaces experiencing such rapid change.

**Different Processing Algorithms** The PS distribution and especially the estimated time series are affected by the processing methods used to analyze the data. Different algorithms and pipelines lead to slightly different results due to their specific pixel selection criteria and deformation models.

#### 2.1.10 Other Mentionable DInSAR Techniques

Besides from Persistent Scatterer Interferometry (PSI) other DInSAR evaluation techniques exist and have been developed in parallel. The Short Baseline Subsets (SBAS) approach (Berardino et al., 2002), which

generates interferograms only between two SAR images with small spatial and temporal baseline, can reduce both spectral and temporal decorrelation using a data set of SAR images acquired subsequently. Its potential lies mainly in the evaluation of areas where dominant scatterers are not omnipresent, such as vegetated or bare soil landscapes. Similar to PSI it can be used to detect ground motion and derive accurate time series (Lanari et al., 2007; Yin et al., 2011; Arangio et al., 2013; Crosetto et al., 2016).

Tomographic Synthetic Aperture Radar (SAR) or TomoSAR (Reigber and Moreira, 2000) can improve deformation sampling as it has the ability to resolve layovers by separating the interfering scatterer. Both PSI and tomography inevitably require a means to detect coherent scatterers, i.e., to perform hypothesis testing to decide whether a given candidate scatterer is coherent. The potential of TomoSAR is in the 3D reconstruction of cities and in the generation of deformation time series has been shown (Zhu and Shahzad, 2014; Montazeri et al., 2015; Wang and Zhu, 2015; Siddique et al., 2018).

### 2.1.11 DInSAR Analysis Software

DInSAR processing and especially Persistent Scatterer Interferometry (PSI) is a complex sequence of computation steps. In the last decades, a handful of implementations have become popular and gained acceptance. Some have been created as academic projects and are now public, but have the disadvantage that they are maintained on a volunteer basis or not at all. Others offer the convenience of a coordinated and efficient computing process. Licenses for such commercial software packages are costly. There are also processing pipelines from various scientific institutions. These have the advantage that they are actively developed by leading experts that contribute their knowledge. Generally, however, it is not possible to access the source code of these pipelines. Some institutions also provide DInSAR analysis as a service. Here, the processing chain is done by experts and only the results are delivered to the customer.

In Table A2 an overview of the pricing, advantages and disadvantages of some popular PSI capable software is given.

Comparisons between different software packets have been made by Simonetto and Follin (2011); Sousa et al. (2011); Osmanoglu et al. (2016); Minh et al. (2020). In conclusion, each software shows different results, due to varying processing approaches e.g. the orbit refinement, selection criterion, phase unwrapping, or the deformation model. In general, it can be said that the results are consistent.

### 2.1.12 Interferometry Capable SAR-Missions

Within the last fifty years, several spacecraft carried SAR sensors into space. The earlier military and intelligence missions focused on using SAR for all-weather imaging. The first civil SAR Mission "SEASAT" (Born et al., 1979) showed the potential of interferometric evaluation of the data. In the following decades several SAR sensors were launched. Processing capability and processing methods were developed along for the data of these space missions. Several national and international satellites were designed and launched, with the focus on repeat orbit interferometry. Due to cheaper launch costs in recent years, the amount of satellites with SAR sensors is increasing and several constellations are planned and brought into orbit. The use of multiple satellites as one system, so called constellations, allows to bring down the repeat orbit time to a few days and enabled a seamless observation of all landmasses.

In Table A1, an overview of the significant interferometric SAR missions is given.

The trend toward private SAR satellite constellations will very likely lead to the wide availability of high-resolution SAR images for all urban areas. The interferometric capability of those micro satellites is often questionable because of the lack of orbit control systems. The evaluation and interpretation of this data will be a challenge for the future and stays an active field of research.

## 2.2 Using Persistent Scatterer Interferometry for Deformation Analysis and Monitoring

**Pioneering work** The first relevant contributions in this field have been carried out before the introduction of the Persistent Scatterer Interferometry (PSI) algorithm through Ferretti et al. (2000, 2001) where Differential Interferometric Synthetic Aperture Radar (DInSAR) was used to monitor the earth's surface changes. For example, Gabriel et al. (1989) used three SEASAT images to estimate the deformations of water-absorbing clays in the soil that cause ground swelling and shrinking in the magnitude of a few centimeters per year. The authors foresaw its application in the detection of pre-eruptive swelling of volcanoes and the monitoring of long-term motion in earthquake areas. Hanssen (2001) described the underlying stochastic and functional models for the deformation model via DInSAR in detail. He also conducted several experiments and case studies on large-scale subsidence phenomena using the ERS-1/2 missions. Hanssen also investigated the use of artificial corner reflectors (CRs), which provide sufficient scatterer if needed.

**Landslides and Sinkholes** After the development of the PSI and SBAS algorithms, large attention has been given to disaster monitoring. Slowly progressing landslides and sinkholes are the optimal target for PSI since the direction of the motion is mostly known and often linear. Colesanti and Wasowski (2006) show the possibility of PSI for the wide-area qualitative distinction between stable and unstable areas and qualitative hazard zonation of large, slowly moving landslides, based on the identification of segments characterized by different movement rates.

Farina et al. (2006) coupled PSI with the interpretation of aerial photos and optical satellite images for landslide investigations. The PS analysis was applied at a regional scale to support landslide inventory mapping and at a local scale aid in the monitoring of single well-known slope movements.

Herrera et al. (2010) used different SAR datasets acquired by ERS-1, ERS-2, ENVISAT, and TerraSAR-X satellites to analyze a landslide area. The use of different SAR images acquired by satellite radar sensors operating at different microwave lengths allowed for a comparative assessment and illustration of the advantages and disadvantages of these satellites for landslide detection and monitoring. They conclude that the PS density of the TerraSAR-X dataset is remarkably greater than that offered by ERS and Envisat. Furthermore they stated that the displacement time series of the X-band is better than the C-band due to the shorter revisiting time (11 days for TerraSAR-X and 35 for ERS) even if some variance errors are present. This facilitates the detection of the non-linear trends that are characteristic of landslide kinematics (e.g. the rainfall influence on the landslide acceleration).

Tofani et al. (2013) used archived ERS and ENVISAT data in combination with recent in-situ measurements to redefine the boundaries of a landslide and the state of activity. While the InSAR time series analysis permitted a better understanding of the deformation pattern and its relation with the causes of the landslide itself, the integration of ground-based monitoring data and PSI data provided accurate results for landslide characterization.

Crosetto et al. (2013) discussed the fundamental aspects of PSI-based deformation monitoring in a landslide context and provide the key elements needed to fully understand and correctly interpret its results. Several technical and logistic aspects related to the use of corner reflectors (CRs) are also addressed including: an analysis of the suitability of DInSAR data to monitor a specific landslide, a discussion on the choice of the type of CRs, suggestions for the installation of CRs and a description of the design of a CR network.

Chang and Hanssen (2014) demonstrated the feasibility of satellite radar interferometry to detect a migrating cavity under the city of Heerlen, the Netherlands. The appeared sinkhole led to foundation instability and the near-collapse of a part of buildings in the surroundings. Chang and Hanssen were using the archives of radar images before and after the damage on the building was noticed.

For local ruptures, like sinkholes and landslides, the three dimensional nature of the underlying deformation is of interest. The measurements that are done by PSI only show the projection of the true velocity vector onto the line-of-sight (LOS) direction. Therefore, it is not possible to retrieve the full displacement vector from a single InSAR measurement. In many cases, a simple model is sufficient to describe the actual movement: down the slope for a landslide and bowl-like crater for sinkholes. Such models have been explored by Samiei Esfahany et al. (2009). Via et al. (2012) decomposed the motion of an earthquake from two DInSAR stacks with different LOS directions into vertical and east-west horizontal components. Goel and Adam (2014) presented a new technique for mapping mean deformation velocity in highly decorrelated areas with known deformation patterns.

**Construction Induced Deformation** The investigation of damage caused by construction activities has been the driver behind many DInSAR applications. Liu et al. (2014) use TerraSAR-X scenes to monitor a underground construction process. This work aimed to detect the deformation of the ground surface and structures above a new subway line during the tunnel excavation. Both surface uplifting and subsidence were observed during this tunneling process, by a leveling survey which was then validated by PSI observation. Liu et al. concluded that sub-centimeter accuracy observations are achievable for process-related monitoring in urban areas, using the open source software package Stanford Method for Persistent Scatterers (StaMPS).

When carrying out underground activities, the status quo must be captured before starting any construction. This is mainly done to be able to justify any claims for damages in retrospect. The availability of archived SAR data allows us to go back in time and process an area of interest. For example, Scoular et al. (2020) investigated patterns of deformation before, during, and after the construction of a subway tunnel using archived data. This study states that if eight years of ERS Persistent Scatterer Interferometry (PSI) data had been analyzed before tunneling, the unusual pattern of displacement may have been recognized, and further targeted borehole investigations could have taken place before the launch of the tunnel boring machine. Results also show that areas of different land use, including housing, cemeteries and historic landfills, exhibit different settlement behaviors, compared with surrounding terraced housing. This research highlights the challenges in interpreting PSI results in an urban area with ongoing construction and the value of a long archive of data. Long records are however becoming less of a problem as almost three decades of archived data from the ERS and Sentinel-1 exist for many urban areas around the world.

Similar to tunneling, mining activities under the earth are always accompanied by above-ground movements and must therefore be monitored in detail. Archived SAR data can be analyzed to find the cause of a fatal event, giving civil engineers insight into the pre-failure patterns. Grebby et al. (2021) study the failure of a tailings dam at an iron ore mine complex in Brazil. They show that the timing of the dam collapse would have been foreseeable based on this observed precursory deformation. Milillo et al. (2019) revealed that a large bridge in Italy was undergoing an increased magnitude of deformations over time prior to its fatal collapse.

**Infrastructure Monitoring** Infrastructure Monitoring is traditionally a very time and resource-consuming task. Extensive infrastructure grids such as railway tracks for high-speed trains, pipelines, and waterways should be continuously surveyed, since a collapse or structural failure would come with unacceptable consequences.

Chang et al. (2017) showed that InSAR can monitor railway tracks and embankments with millimeter-level precision over wide areas. They state that PSI it is one of the most powerful and economical means for monitoring the safety and stability of the infrastructure on a weekly basis.

Bayramov et al. (2020) quantitatively assessed the ground deformation velocities and rates and their natural and man-made controlling factors as the potential risks for oil and gas pipelines in Azerbaijan using PSI technique. The diverse spatial distribution and variation of ground movement processes along pipelines

demonstrated that the general geological and geotechnical understanding of the study area is not sufficient to find and mitigate all the critical sites of subsidence and uplifts for the pipeline operators.

**Motions of Single Buildings** If detected early, adversarial deformations on buildings can be effectively countered. The wide availability of high-resolution SAR data makes PSI a relatively cost-efficient way to detect such motions early, considering that any method can be extended to a city-wide single building monitoring. Intensive studies on where on buildings PS points occur were carried out by Gernhardt et al. (2010); Gernhardt and Bamler (2012). They provide insight into PS densities in urban structures. From a comparison between ascending and descending tracks of TerraSAR-X data, it can be shown that the main orientation of a building has significant influence and should be considered for maximizing the number of scatterers in a scene. The optimal orientation of building facades is parallel to the flight track. An encouraging example for a large building was presented conducted on the Berlin central railroad station, which experiences a seasonal deformation due to the thermal expansion of the steel structure. By using nonlinear displacement model in the PSI processing, those seasonal effects were observed.

Schunert and Soergel (2016); Schunert et al. (2012) showed that the majority of PS points on buildings are caused by facade structures. In particular, regularly spaced rows of windows lead to salient grids of similar appearance in TerraSAR-X data. By comparing PS points, derived from high-resolution X-band data, to 3D models, it has been shown that the affiliation of PS points to facades is quite unproblematic, due to the utilized building models compare quite well with the actual building surfaces at frontages. They could show that the locational accuracy of the PS points is sufficient for such an assignment.

Crosetto et al. (2015) also investigated on the thermal expansion patterns of PSI time-series. Three examples are discussed in detail: a viaduct, a set of industrial buildings, and two skyscrapers. The thermal maps can be used to derive the thermal expansion coefficient of the observed objects and allow to gain information on the buildings static structure.

Guo and Zhu (2014) used TerraSAR-X data to map urban areas in high detail using many advanced interferometric techniques such as PSI and TomoSAR processing. These multi-pass interferometric techniques are based on a great number of images and achieve to extract features of high rise buildings.

Sanabria et al. (2014) proposed a method to produce subsidence activity maps based on the geostatistical analysis of PSI displacement data. These maps permit them to identify widespread subsiding areas and buildings where damages could be produced. This result provides a tool for the planning and management activities of the local authorities.

Bianchini et al. (2015) used two COSMO-SkyMed image stacks to investigate the damage of slow landslides on single buildings. By finding a geometric relationship between the distance of PS points and their displacement a per-building risk assignment is carried out. The findings are backed up by in-situ validation campaigns and geological knowledge. Accordance between the estimated building deformations and on-field damage evidence was found.

Costantini et al. (2018); Zhu et al. (2018) presented a method for the detection of anomalous deformations in the spatial or the temporal dimension of PS points. The method takes in InSAR deformation measurements. In the spatial dimension, in order to reduce the dataset size, they utilize a hierarchical clustering method to obtain convergence points that are more trustful to detect spatially in-homogeneous deformations. In the temporal dimension, they use a signal processing method to decompose the input into two main components: regular periodic deformations and piece-wise linear deformations. They tested the method on different cases, and they report the results obtained on PS measurements from high-resolution X-band COSMO-SkyMed data on various cities. The in-field survey confirmed that the proposed method is very promising. The here proposed approach enables the detection of deformation anomalies that could cause building or infrastructure stability problems.

Using supervised and unsupervised machine learning, Toma et al. (2019) examine the potential for identifying aberrant deformation profiles. Using canonical functions to represent various deformation situations unique to potential hazardous events in an urban context, they generate a simulated data set containing deformation profiles for this purpose. Using a clustering method and a classifier trained on simulated deformation profiles, they provide findings for identifying anomalous profiles in the simulated data set and in real data.

**Web Based Platforms** The previously mentioned use cases of the PSI technique demonstrate its broad spectrum of applications. From wide-area mining-induced sinkhole monitoring to three-dimensional single building scenes. The various application of PSI show complex movement patterns with their underlying time-series and non-uniformly distributed scatterer. The interpretation of such results is often only possible with expert knowledge from various other fields such as geophysics or civil engineering. To present the DInSAR results to such experts, they commonly have to be simplified or condensed so they can be presented in traditional printouts, figures, graphs, and tables. Such experts rarely have the required software or computational power to deal with the raw data, like 3D PS point clouds and their time series. A solution to this problem is the development of specialized web platforms. Here the entry level is quite low since only a web browser is required to access the data. The presentation of DInSAR results in such an environment is not limited to two-dimensional static views of the scene and the user can decide which part of the data set is relevant. The handling of the large database is done by the server. Such experts geographic information systems (GISs) are currently helping to provide solutions to complex problems that need human expertise (Lukashev et al., 2001).

One example for such a expert GIS is the Ground Motion Service Germany (BBD) (<https://bodenbewegungsdienst.bgr.de/>) (Kalia et al., 2021; Lege et al., 2019; Kalia, 2017). It provides access to nationwide InSAR evaluations and can be used by authorities for improved security, space and urban planning. The core dataset of the BBD is based on nationwide Copernicus Sentinel-1 data, which was processed using the Persistent Scatterer Interferometry (PSI) procedure. For the interactive visualization of the ground motion data, a WebGIS can be used in which the PSI points are superimposed with various base maps and the linear velocity trend is color coded to give a quick overview of the general behavior. If single points and time series are of interest they can be displayed along with additional information about the source data.

Similar regional projects have been realized in other European countries. The European Ground Motion Service (EGMS) (<https://egms.land.copernicus.eu/>) (Crosetto et al., 2020; Costantini et al., 2021; Crosetto et al., 2021) unifies and standardizes those efforts continent-wide. The EGMS constitutes the first application of the InSAR technology for monitoring of ground deformations over an entire continent, based on full-resolution processing of all Sentinel-1 (S1) satellite acquisitions over most of Europe (Copernicus Participating States). EGMS monitors, with millimeter-scale precision, ground motion caused by phenomena, such as subsidence, landslides, tectonic effects, earthquakes, or volcanic activities, with impacts on the stability of slopes, mining areas, buildings, and infrastructures. It is seen as a public service that can be used and accessed free of charge.

## 2.3 Bottom Line

The aforementioned applications of Persistent Scatterer Interferometry (PSI) can be generally categorized into two classes: the monitoring of large-scale phenomena and the evaluation of individual buildings with complex 3D extensions.

Large-scale deformations occur from earthquakes, landslides, or widespread settlements due to cavities, sinkholes, or construction activities. Nowadays, the PSI technique is widely developed and used in practice.

Usually, the PS points are considered as single measurements instead of examining patterns as a whole. It is important to move from points to grids of time series that can be evaluated as ensembles, rather than looking at single points. Methods from other fields such as weather forecasting should be used and different PS point sources can be combined from different viewpoints to make this transition. Some methods and best practices for this are introduced and evaluated in Chapter 3.

The second major application area is the monitoring of individual buildings and other complex structures. With the advent of cheaper and more widely available high-resolution SAR data, even relatively small buildings can be observed. An open question is how to automatically monitor entire neighborhoods. This starts with deciding which PS point is on which building and continues with how to extract redundant groups and patterns from the many individual measurements. The question also arises of how existing city models and BIM data can be linked to such SAR measurements. In Chapter 4, a workflow for this is presented and evaluated on different test areas by also using in-situ measurements.

With either application, the information gained in this way must be communicated to decision-makers and other stakeholders. Especially for building monitoring, it is not practical to print large complex 4D data sets and display them as 2D projections. Approaches need to be developed in order to better present SAR data. Web-based tools or the integration into industry standard programs are two approaches, that help decision-makers and other experts to get a greater picture of the situation. In Chapter 5, this problem is discussed and addressed, using different exemplary implementations.



## Chapter 3

# Investigation into Deformations of Large Surfaces

Persistent Scatterer Interferometry (PSI) is best suited for the monitoring of deformation events over a large area, such as subsidence due to mining operations or ground water flow through cavities. PSI provides an overview over the deformation process and DInSAR techniques offer the unique possibility to monitor a wide area with a millimeter accuracy and temporal resolution of a few days. Through the analysis of the results from the PSI evaluation, it is possible to recognize and identify underlying patterns of deformation. In this chapter, methods for the identification of such patterns in Persistent Scatterer (PS) points that cover a wide area are discussed. It will be explained how different observation directions can be used to decompose a motion vector in its horizontal and vertical components. For this, the necessary transitioning to a raster representation spatial and temporal interpolation is explained. Furthermore, a method is presented that analyzes a field of PS points and their time series and separates them by their underlying motion patterns.

### 3.1 Grid-Base Representation

Since distribution of the Persistent Scatterer can not be predicted, a deformation phenomenon can only be a sample at certain points, as such a grid-based representation is desirable to further process the results. Especially for large amounts of PS points measurements, the computational effort significantly decreases if the points are interpolated to a grid. If the data of multi-modal sources needs to be fused or if one set of PS points has to be combined with another set from a different orbit perspective (Sec 3.3), such a grid-based representation simplifies the data processing.

#### 3.1.1 Spatial Interpolation

To convert from a point-based representation to a grid, several methods exist. In general, this conversion can be considered a two-dimensional interpolation problem. The most intuitive and also fastest methods are nearest neighbor, bi-linear, or bi-cubic interpolation. In the distribution of PSI data from a real-world scenario, there are densely sampled areas, such as houses, streets, or other infrastructure and man-made objects, and there are areas with nearly no PS points like on dense vegetation or water bodies. Therefore sampling can be very in-homogeneous. The gaps have to be bridged with interpolation and can lead to unreliable information about the undergoing deformation process. A buffer mask that does not consider the

interpolated values from far away sampling points can be implemented to avoid this problem. Figure 3.1 shows the difference between a smooth distribution in which the sample points are distributed homogeneously and a more heterogeneous distribution that was sampled unevenly.

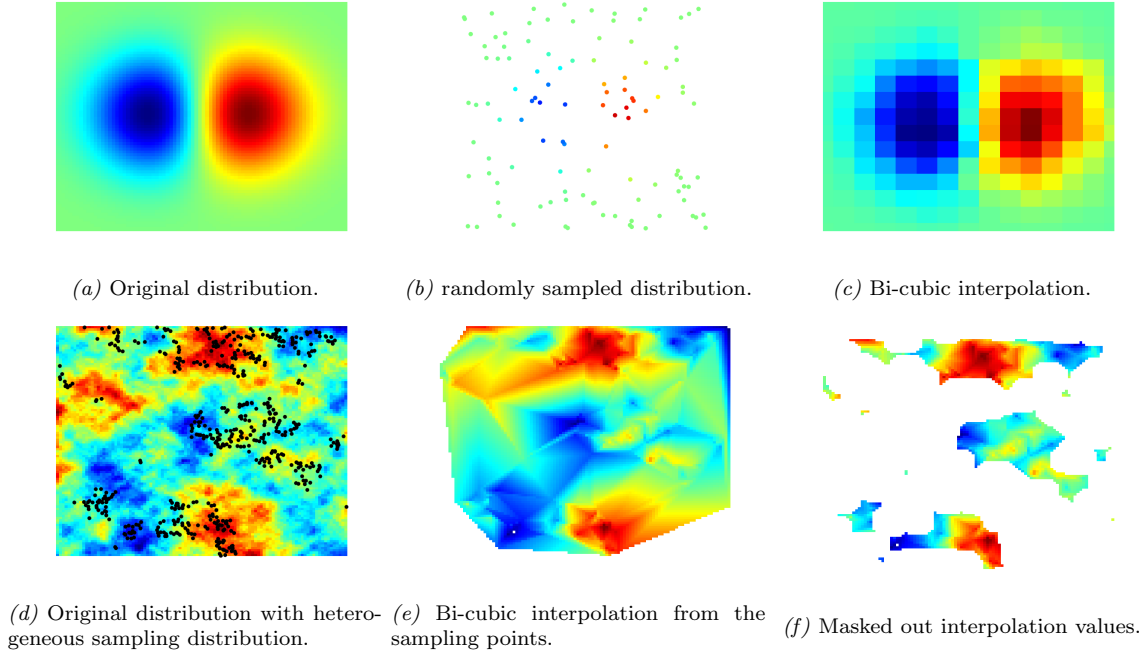


*Figure 3.1:* Difference between homogeneous (top) and heterogeneous (bottom) sampling and reconstruction of a signal. If a relative simple signal (a) is sampled homogeneously (b) the original distribution can be reconstructed (c). A complex signal, sampled heterogeneously, like shown in (d) cannot be properly reconstructed, as shown in (e). Masking out the grid cells far from sampling points can help better define the valid reconstruction areas (f).

## 3.2 Temporal Interpolation

Differential Interferometric Synthetic Aperture Radar (DInSAR) methods like PSI process a stack of coherent SAR images to derive the movement or deformation over time for certain pixels. This leads to a discrete-time series that describes the line-of-sight movement towards or away from the SAR antenna for each of these points. When analyzing a complex deformation behavior, a second observation from a different direction is necessary to decompose the line-of-sight projections into vertical and horizontal components (see Section 3.3). If the two-time series need to be combined, their different sampling dates have to be considered. For common interferometric SAR missions, the repeat cycle is 6 to 20 days (Table A1). The time difference to acquisition of the second stack is independent of this and solely depends on the chosen repeat orbit. It can however have an offset of a few days. This means that the deformation is sampled at two different points in time. If the two observations need to be combined, the time steps have to be interpolated. When decomposing such movements, the noise on the deformation signal impacts the results as the decomposition procedure is sensitive to any small differences in the two observed signals (see Section 3.3). Hence, a smoothing or filtering is often carried out. This allows for approximation of the entire time series by a polynomial. If the data is spatially interpolated onto a grid, the temporal interpolation has to be carried out for each grid cell.

### 3.2.1 Polynomial Approximation for Resampling

In the case of grid-based representations a 3rd-degree polynomial can be defined for each cell, for example, with latitude and longitude coordinates  $d(\lambda, \phi, t)$  over time  $t$  such as:

$$d(\lambda, \phi, t) = a_3(\lambda, \phi) \cdot t^3 + a_2(\lambda, \phi) \cdot t^2 + a_1(\lambda, \phi) \cdot t + a_0(\lambda, \phi) \quad (3.1)$$

The unknown polynomial coefficients have to be estimated for each grid cell. A functional relationship between the polynomial coefficients  $a_n$  the time steps  $t_m$  and the deformation at this time  $d(t_m)$  can be made by:

$$y = A \cdot x \quad (3.2)$$

where  $y$  is the vector of the observed time series:

$$y = [d(t_1) \quad d(t_2) \quad \dots \quad d(t_m) \quad \dots \quad d(t_M)] \quad (3.3)$$

$A$  is a matrix with the time steps:

$$A = \begin{bmatrix} 1 & t_1 & t_1^2 & t_1^3 \\ 1 & t_2 & t_2^2 & t_2^3 \\ \vdots & \vdots & \vdots & \vdots \\ 1 & t_m & t_m^2 & t_m^3 \\ \vdots & \vdots & \vdots & \vdots \\ 1 & t_M & t_M^2 & t_M^3 \end{bmatrix} \quad (3.4)$$

The polynomial coefficients can be estimated via the least squares method:

$$\hat{x} = (A^T A)^{-1} A^T \cdot y \quad (3.5)$$

such that the optimal solution for the 4 coefficients is:

$$\hat{x} = [a_0 \quad a_1 \quad a_2 \quad a_3] \quad (3.6)$$

Polynomial approximation is suitable for slow movements of low acceleration. The use of polynomials also allows for very simple differentiation of the given data. This helps to find areas and intervals in time that undergo a rapid change. However, polynomials cannot be used to extrapolate a time series, since they will always tend towards infinity. If abrupt movements are expected in the data, this procedure should not be applied.

## 3.3 Using Multiple Observations for Decomposition

From a given deformation process, analyses of a single SAR image step with PSI will only measure the projection of this deformation  $D_{REAL}$  onto the line-of-sight (LOS) as shown in Figure 3.2a. This projection varies based on the inclination angle  $\theta$ . If different observation directions from an ascending orbit and a descending orbit are considered for example, the resulting projection can vary. This is shown in Figure 3.2a as the  $D_{ASC}$  and the  $D_{DSC}$ . If the incidence angle  $\theta_{DSC}$  and  $\theta_{ASC}$  is known, the original movement can be reconstructed, by decomposing it into a horizontal and a vertical component  $D_{horiz}$  and  $D_{vert}$ . If the east-west is of interest instead of the horizontal component between the two orbits, the azimuth of the two

observation directions  $\alpha$  has to be considered. In practice, the difference is small since SAR satellites are on polar orbits meaning that they fly with an azimuth close to  $0^\circ$  respectively  $180^\circ$ .

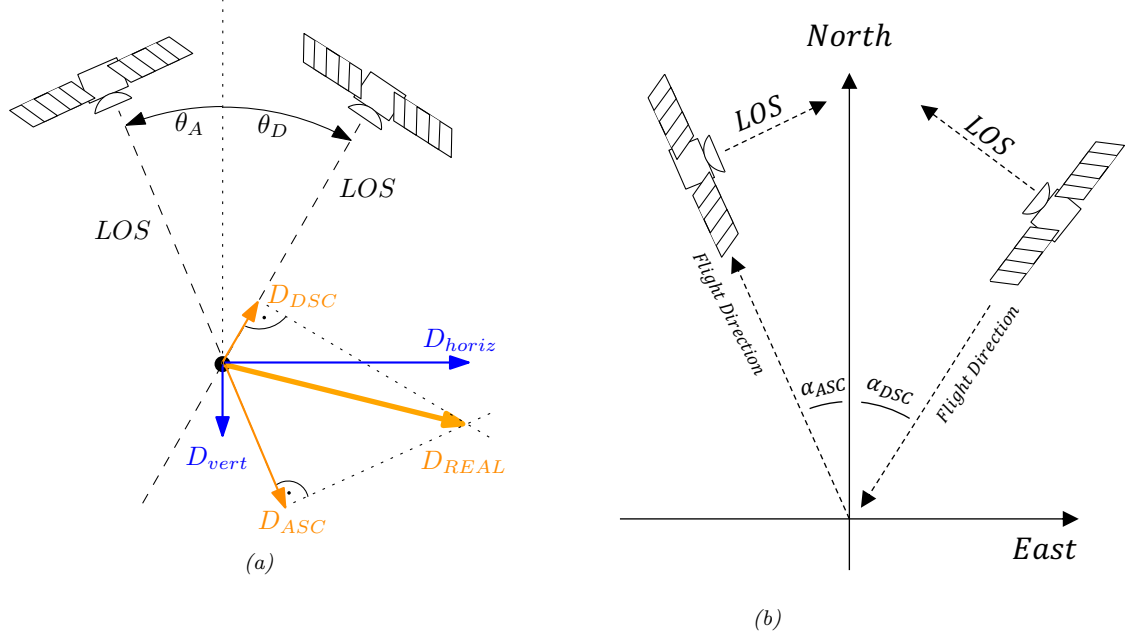


Figure 3.2: Two Orbit Decomposition. (a) Side view with the projected and decomposed deformation. (b) Top view on configuration with azimuth of the satellites orbit  $\alpha_{ASC}$  and  $\alpha_{DSC}$ .

The relationship between the observed deformation  $d_{los}^{ASC}$   $d_{los}^{DSC}$ , the vertical (up-down) component  $d_{vert}$  and the horizontal (east-west)  $d_{east}$  is as follows:

$$\begin{bmatrix} d_{los}^{ASC} \\ d_{los}^{DSC} \end{bmatrix} = \begin{bmatrix} \cos(\theta_{ASC}) & -\sin(\theta_{ASC}) \cdot \cos(\alpha_{ASC}) \\ \cos(\theta_{DSC}) & -\sin(\theta_{DSC}) \cdot \cos(\alpha_{DSC}) \end{bmatrix} \cdot \begin{bmatrix} d_{vert} \\ d_{east} \end{bmatrix} \quad (3.7)$$

In practice, this has to be solved for every grid cell (Section 3.1).

Note that this observation geometry can not detect movements that are perpendicular to both LOS vectors. Usually this is the north-south direction.

### 3.4 Spectral Analysis of Time-Series Fields

The result from PSI analysis is a point cloud with the position of each Persistent Scatterer (PS). In fact, the points contain their deformation history so the point cloud could be also considered as field of time series. In this section, a method is shown that allows to evaluate the entire field and find underlying patterns in the time series. The spatial extension of a deformation pattern of interest can then be further investigated.

### 3.4.1 Empirical Orthogonal Functions for the Analysis of a Field of Time-Series

A method to find underlying patterns, also known as modes, in an ensemble of PS points is the Empirical Orthogonal Functions (EOF) analysis. Similar to Principal Component Analysis (PCA), this method aims to decompose the signals into a set of orthogonal functions. Unlike other harmonic analysis methods, such as the Fourier Transformation, the base functions of EOF are not predetermined and are found empirically for the given data, as the name suggests. This method originates from the analysis of distributed weather stations in oceanography (Preisendorfer, 1988), but it can be used for all kinds of time series fields, such as PS points. Typical, it helps to identify an underlying pattern and can further separate superimposed movements, like the seasonal oscillation and a linear trend. This method can also find spatial patterns by analyzing the maps of the coefficients. A tutorial on the topic, including a mathematical and a hand-waving explanation, is given by Bjornsson and Venegas (1997). In the rest of this subsection, the process for the EOF the computation is outlined in a way that it can be implemented for a given data set.

The process can be summarized into four steps:

1. Form a matrix  $F$  from the time series (3.8).
2. Calculate the Singular Value Decomposition (SVD) in the form  $C \cdot \Lambda \cdot V^T = F$ .
3. Find the biggest singular values (the trace of  $\Lambda$ ) and the corresponding eigenvectors (row or column of  $C$ ). These are the EOF.
4. Visualize the maps of the so-identified interesting EOF.

In step 1, the set of  $N$  PS points, each with a time series of length  $M$ , are arranged in a Matrix  $F$  so that each column represents a time series and each row a (deformation) map at a certain time  $t_m$ .

$$F = \begin{bmatrix} d_1(t_1) & d_2(t_1) & \dots & d_n(t_1) & \dots & d_N(t_1) \\ d_1(t_2) & d_2(t_2) & \dots & d_n(t_2) & \dots & d_N(t_2) \\ \vdots & \vdots & \ddots & \vdots & \ddots & \vdots \\ d_1(t_m) & d_2(t_m) & \dots & d_n(t_m) & \dots & d_N(t_m) \\ \vdots & \vdots & \ddots & \vdots & \ddots & \vdots \\ d_1(t_M) & d_2(t_M) & \dots & d_n(t_M) & \dots & d_N(t_M) \end{bmatrix}_{M \times N} \quad (3.8)$$

In step 2, for this  $M \times N$  matrix a singular value decomposition can be carried out:

$$C \cdot \Lambda \cdot V^T = F \quad (3.9)$$

which can be solved using many algebraic libraries. Since there are often more points than time steps in the time series ( $N > M$ ), the economic variant is used here.

In step 3 the singular values and eigenvectors are analyzed. The  $\Lambda$  is a  $M \times N$  containing the  $M$  singular values  $\lambda_m$  on its primary diagonal.

$$\Lambda = \begin{bmatrix} \lambda_1 & 0 & \dots & 0 & \dots & 0 \\ 0 & \lambda_2 & \dots & 0 & \dots & 0 \\ \vdots & \vdots & \ddots & \vdots & \ddots & \vdots \\ 0 & 0 & \dots & \lambda_m & \dots & 0 \end{bmatrix}_{M \times N} \quad (3.10)$$

The column vectors of  $C$  are the eigenvectors or in other words the Empirical Orthogonal Functions (EOF).

$$C = \begin{bmatrix} EOF_1 & EOF_2 & \dots & EOF_n & \dots & EOF_M \end{bmatrix}_{M \times M} \quad (3.11)$$

Each EOF is a vector that should be considered and analyzed as a time series. The relative magnitude of the singular values is an indicator of the amount of variance in the data that can be explained by the corresponding EOF. It is helpful to focus on the analysis of the most important EOFs in the next steps as not all EOFs will be explainable, meaning they are likely be noise artifacts. By looking at the plots of these EOFs found as being of interest, often deformation characteristics like linear trends or periodic annual movements can be identified. It is important to notice that the EOFs do not have a magnitude or sign.

From (3.9) it is clear that each time series can be restored by the weighted sum of all EOF:

$$d_n = \sum_{m=1}^M EOF_m \cdot v_{mn} \cdot \lambda_m \quad (3.12)$$

Therefore, the first  $N \times M$  block in  $V$  can be considered as the weights per time series and EOF.

$$V = \begin{bmatrix} \mathbf{v}_{11} & \mathbf{v}_{12} & \dots & \mathbf{v}_{1M} & \dots & v_{1N} \\ \mathbf{v}_{21} & \mathbf{v}_{22} & \dots & \mathbf{v}_{2M} & \dots & v_{2N} \\ \vdots & \vdots & \ddots & \vdots & \ddots & \vdots \\ \mathbf{v}_{n1} & \mathbf{v}_{n2} & \dots & \mathbf{v}_{nm} & \dots & v_{nN} \\ \vdots & \vdots & \ddots & \vdots & \ddots & \vdots \\ \mathbf{v}_{N1} & \mathbf{v}_{N2} & \dots & \mathbf{v}_{NM} & \dots & v_{NN} \end{bmatrix}_{N \times N} \quad (3.13)$$

This decomposition can be used to detect characteristic movements. It can also be used to selectively filter out a modes, by not considering them in the synthesis step (3.12).

The interesting Empirical Orthogonal Functions (EOF) that are found can be visualized by plotting them over time. Typically, the most relevant modes are linear trends and seasonal oscillations. The method can also find other patterns like those induced by a single common event.

In step 4, if interesting patterns are identified in the EOFs their spatial pattern can be investigate in by plotting the corresponding weights in the spatial domain. Using this map, it is possible to find PS points with time series that, for the most part, consists of this mode. The weights also contain information about the sign of the EOF. An EOF that shows an annual oscillation with the maximum in summer can become one with a maximum in winter by using a negative weight. Similar to this, lowering can become uprise by using a negative weight.

The analysis of the temporal depends on spatial patterns and vice verse. Sometimes an interesting mode has to be plotted in the spatial domain and paired with external knowledge about the underlying processes for it to be interpreted.

## 3.5 Experiments

In this chapter, some methods for the investigation of surface deformation phenomena have been presented. In this final section, these methods are applied to three DInSAR data sets.

**Dataset 1** The first data set consists of 39 high-resolution SAR images from an ascending orbit and 46 from a descending orbit. The data was captured by the TerraSAR-X satellite between January 2018 and September 2019 using High Resolution SpotLight mode and has a ground sampling distance (GSD) of  $1\text{ m} \times 1\text{ m}$ . The scene shows a lock on the river in southern Germany. Previous studies and geophysical surveys have revealed undermining and subsidence of the lock area (Kauther and Wolf, 2018; Haala et al., 2022).

**Dataset 2** shows the same area as *Dataset 1*. In fact it is an addition to the descending data set. In total 106 images were captured during March 2015 and September 2019 but with a significant acquisition gap of more than one year between November 2016 and January 2018.

**Dataset 3** is an example for the medium resolution Sentinel-1 data. In this scene the motions of a tailing dam in El Soldado, Chile are analyzed. The GSD of this Interferometric Wide Swath (IW) Mode is  $5\text{ m} \times 20\text{ m}$ .

**PSI Software** ENVI version 5.5 with SARscape version 5.5.3 (SARMAP, 2014), was utilized to obtain the results.

### 3.5.1 Interpolation and Decomposition

In Figure 3.3b, Persistent Scatterer (PS) points from *Dataset 2* are superimposed with an orthophoto. This shows nicely how the scatterers appear along man-made structures, such as the houses, the streets and the lock structure in the river. PSs do not appear on areas that undergo a significant surface change over time, such as vegetation like fields and forest, the river, and the construction site in the lower left part of the scene.

The points in Figure 3.3b are color coded in order to show the velocity of the line-of-sight displacement. Figure 3.3c shows the same scene but with bi-cubic interpolation onto a  $5\text{ m} \times 5\text{ m}$  grid. To avoid interpolation artifacts, grid cells that are further than two grid cells or 10 m away from a PS point are masked out.

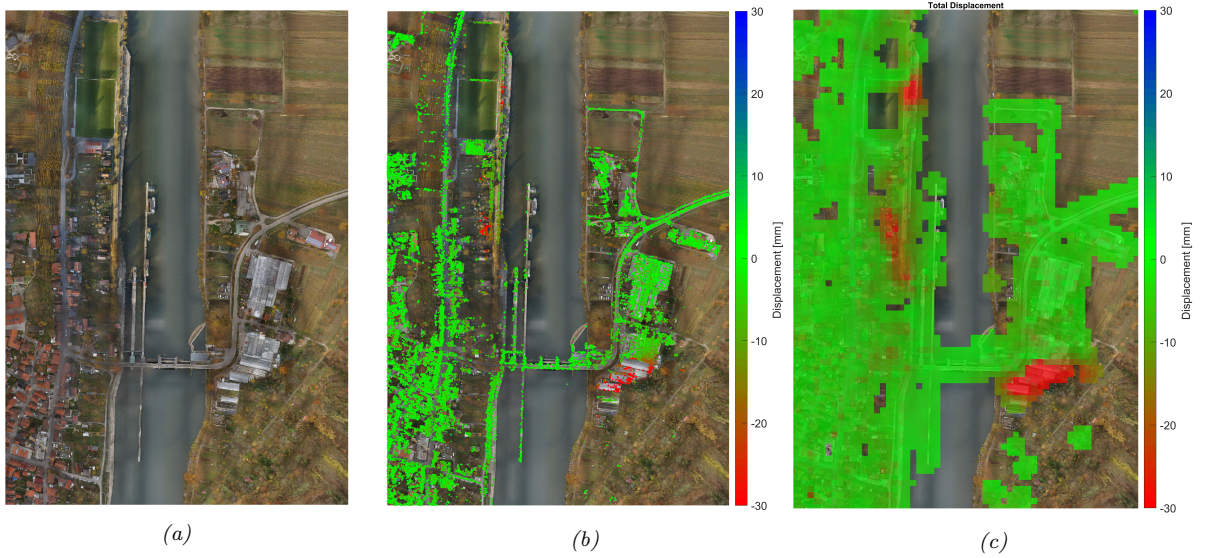


Figure 3.3: (a) Overview over the scene. (b) Distribution of PS points. (c) Bi-cubic interpolation on a grid. The interpolated representation (c) points out the subsidence areas clearly.

This representation helps with the interpretation of the deformation pattern. For example the subsidence areas in the upper left are hard to grasp in the point representation but can easily be distinguished in the raster.

In addition to the advantages of better interpretability, the grid representation offers the possibility that data from different directions of observation can be processed together. Figure 3.4a shows the PS points from the two different orbits or viewing directions of *Dataset 1*. The line-of-sight motion was also interpolated onto a common grid.

In Figure 3.4b, the two scenes from *Dataset 1* are combined as suggested in *Sec.3.3* to derive the vertical and horizontal components of the deformation process.



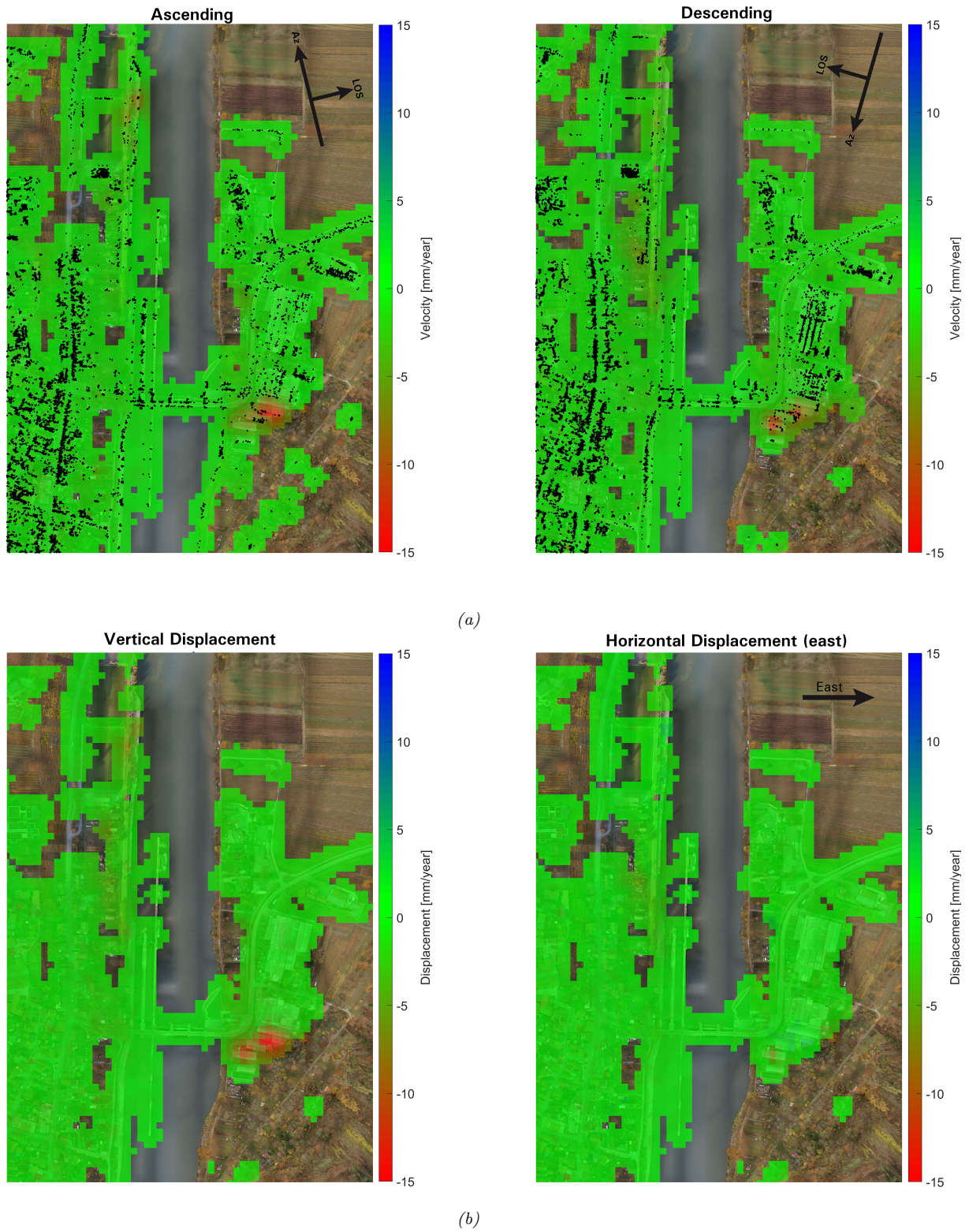


Figure 3.4: (a) PS points for two observation directions (ascending/descending) from *Dataset 1* interpolated on a grid. The line-of-sight velocity is color-coded. (b) Decomposition of the two observations into a vertical and a horizontal component. Valid values can only be obtained for grid cells that have a measurement in the ascending and descending orbit.

### 3.5.2 Temporal Interpolation and Time Series Decomposition

Besides the velocity, each grid cell can also be assigned to a deformation value over time, respectively a point in a time series. To carry out the decomposition (Sec. 3.3) at the same time, the ascending and descending results have to be interpolated in time. Figure 3.5 shows two interpolated time series for one grid cell in *Dataset 3*, along with their decomposition into a vertical up-down and a horizontal east-west component.

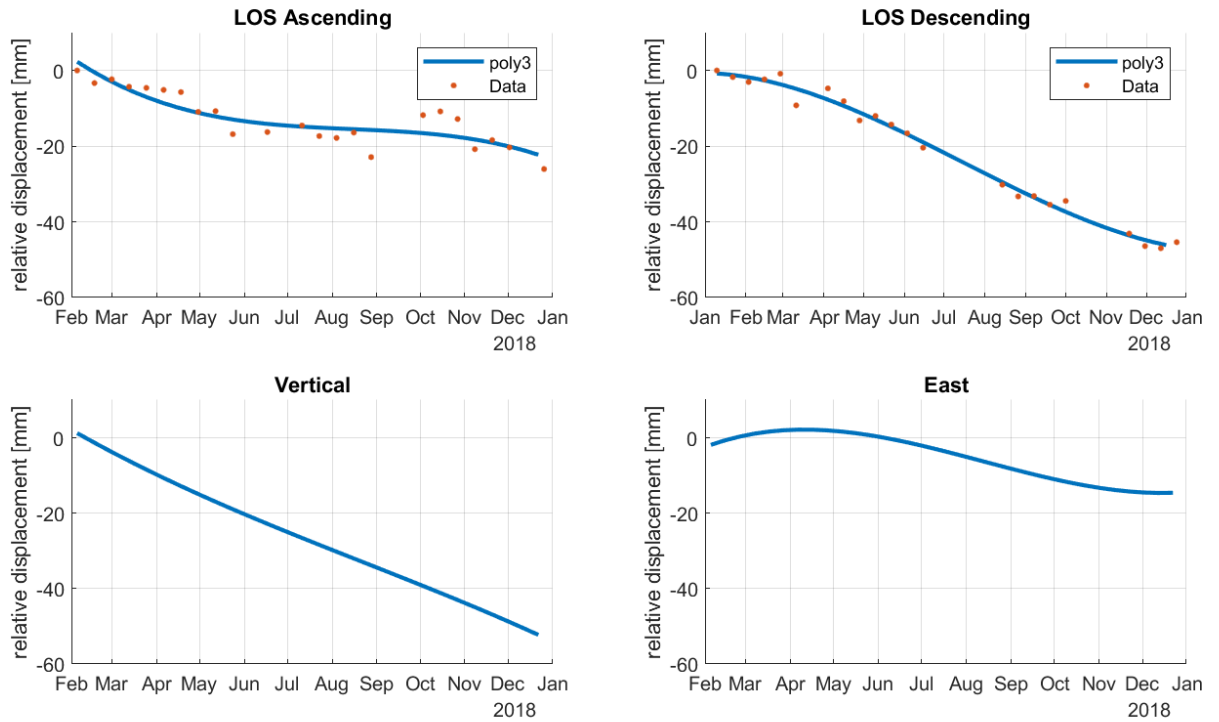


Figure 3.5: Top: Temporal interpolation of a time series via a 3rd degree polynomial. Bottom: Decomposition of these time series into the vertical and horizontal component

The temporal and spatial interpolation of DInSAR results can also be useful when visualizing such data. In Figure 3.6, the DInSAR measurements from two orbits were interpolated on a common grid, for each grid cell a polynomial approximation was carried out. The vertical component of the deformation is combined with a digital surface model (DSM) and an orthophoto. This enables an overemphasized animation of the underlying deformation behavior for visualization purpose.

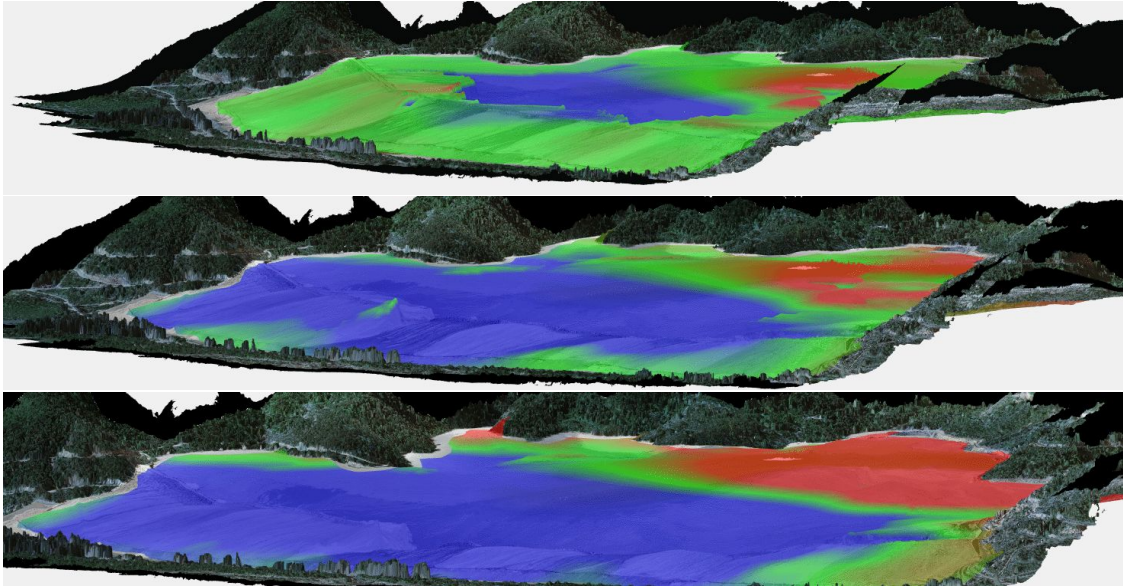


Figure 3.6: Three time steps from the animation of the deformation at a tailing dam in *Dataset 3*. The vertical movements can be combined with a DSM and a digital orthophoto of the scene, to create an animation of the plastic deformation.

### 3.5.3 Spectral Analysis

Spectral analysis is a tool to find Empirical Orthogonal Functions (EOF) that make up the deformations in a field of PS points more specifically, it helps to separate annual movements from linear trends. In the following example, this method is applied to PS points from the analysis of a stack of 106 High-Resolution Spotlight TerraSAR-X images (*Dataset 2*). The deformation data covers a time span of almost 5 years, with a significant acquisition gap of one year. The ground sampling distance (GSD) of the original image is approximately  $1\text{ m} \times 1\text{ m}$ .

In Figure 3.7, an overview of the distribution of the PS points in the scene is given. The scene shows a river lock structure with domestic houses on the left side of the river and a plant nursery with large greenhouses on the right-hand side. PS points can be found along streets, on the houses, on the lock structure, and on the steel structure of the greenhouses.

The velocity of the PS points shows subsidence in some areas, as depicted in Figure 3.3b.



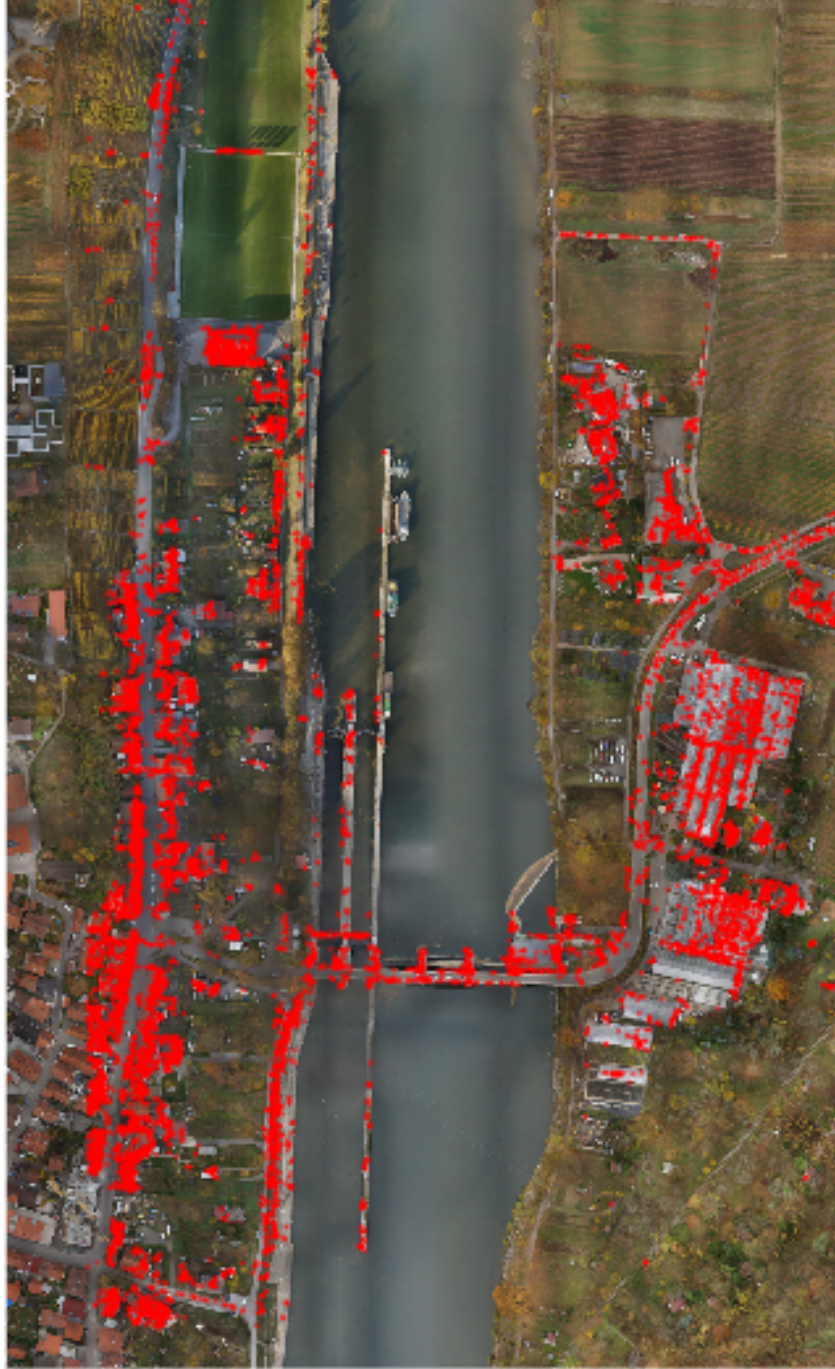


*Figure 3.7:* Overview of the distribution of the PS points. The points lay mainly on the houses and on the river lock structure.

By applying the Empirical Orthogonal Functions (EOF) decomposition workflow described in Sec. 3.4.1, 106 modes or *EOF* can be derived from the data set. The first 5 EOFs are shown in Figure 3.8.

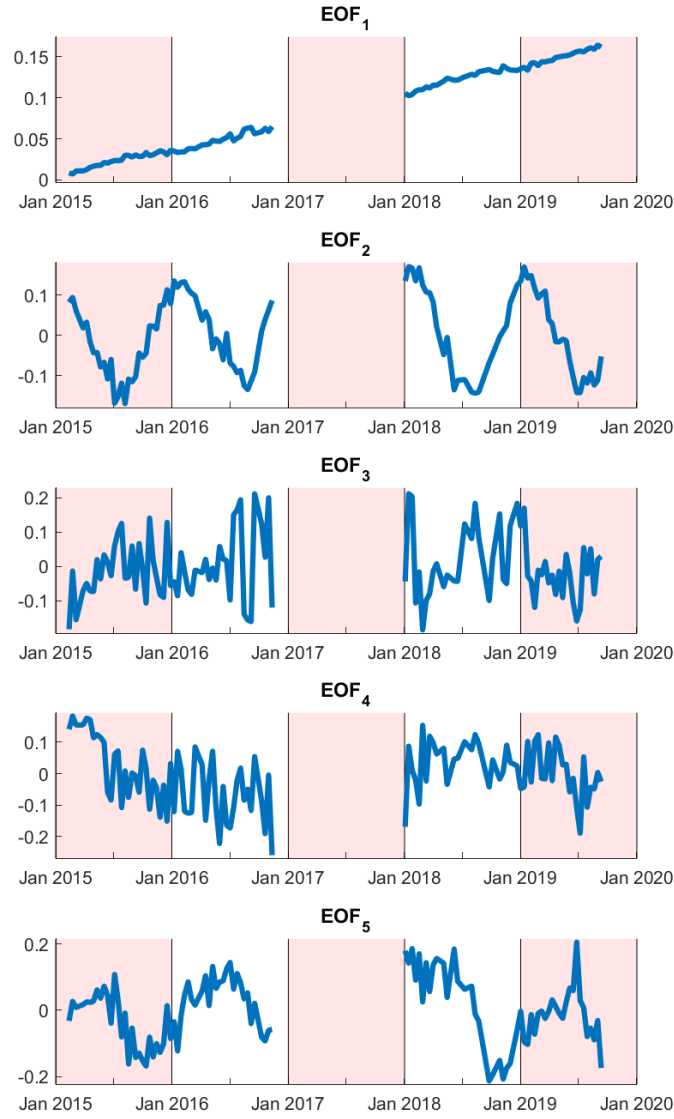


Figure 3.8: The first five EOFs or modes for a field of PS points. The acquisition time gap does not affect the analysis.

One interpretation for  $EOF_1$  and  $EOF_2$  is evident: A linear trend and an annual mode with peaks in summer, respectively in winter. The other modes do not follow a here known pattern. Analyses of the normalized trace of the  $\Lambda$  matrix in Eq. (3.10) can give an insight into how the variance in the original time series is explained by the corresponding mode.

Figure 3.9 shows the  $M = 106$  normalized singular values.

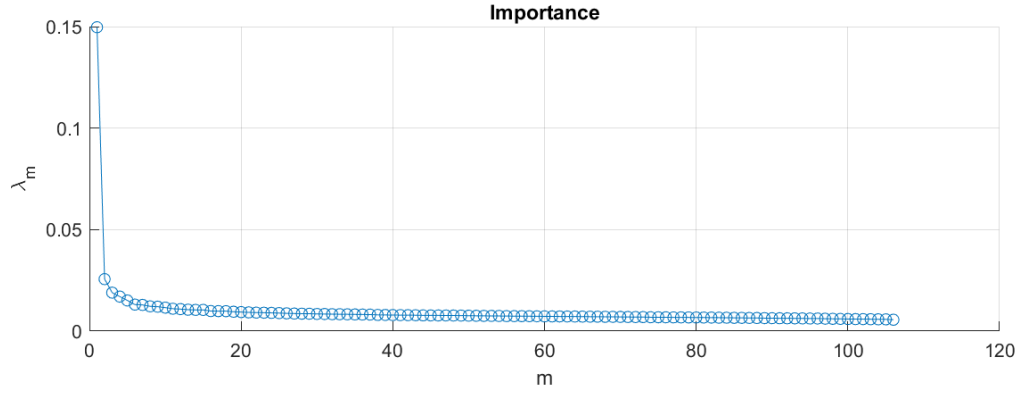
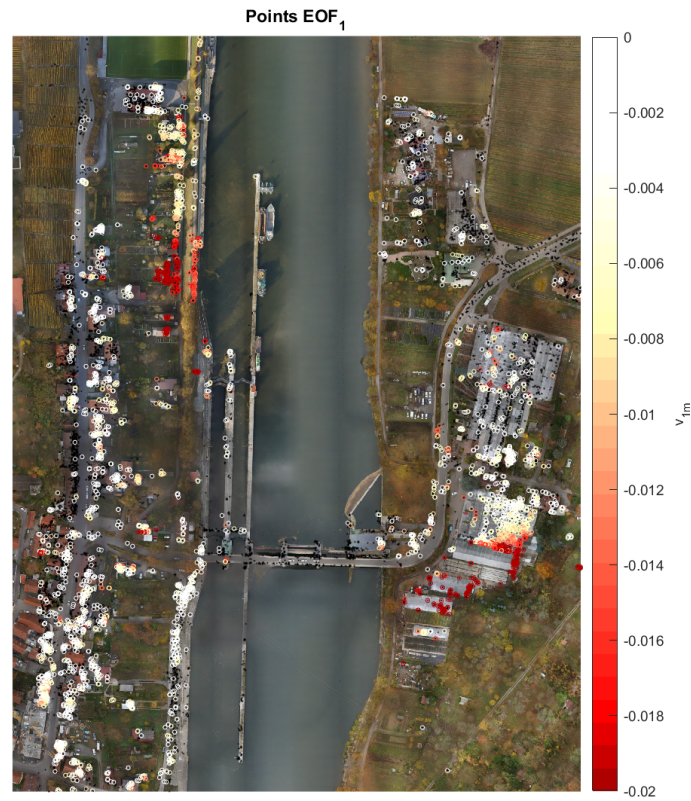


Figure 3.9: Primary diagonal of  $\Lambda$  (3.10)

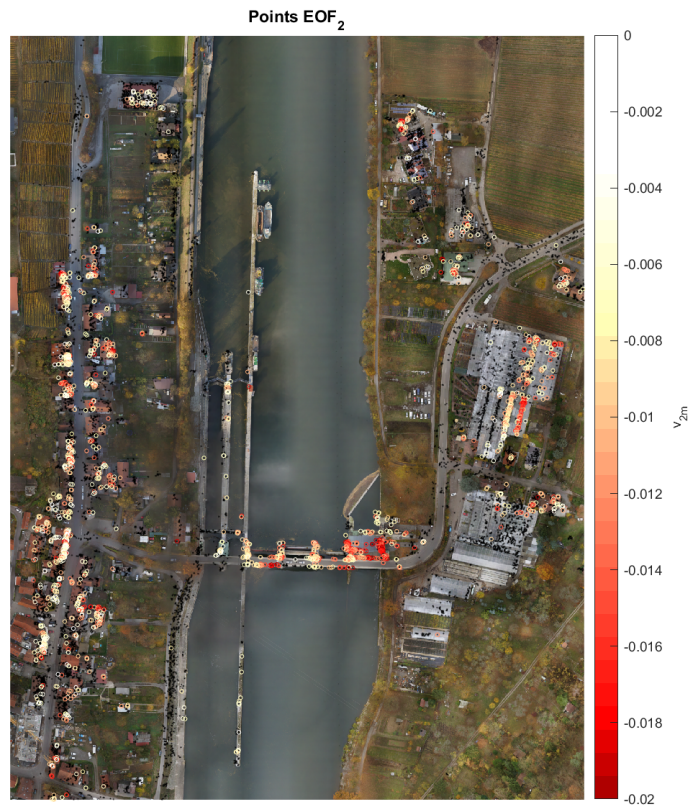
The the sharply decreasing graph shows that most of the variance can be explained by  $EOF_1$ . The significance of the other EOFs drops rapidly.

To spatially map out which mode is most dominant, the weight matrix  $V$  from Eq. (3.13) is analyzed. In Figure 3.10 the PS points that mainly consist of the  $EOF_1$  and  $EOF_2$  are plotted. The magnitude of the corresponding weights is color coded. Note that the absolute value is considered here. Only by weighing the  $EOF_1$  with a negative value, the subsidence can be modeled.

The linear trends in Figure 3.10a are consistent with the known subsidence areas. This can also be seen in Figure 3.3. The annual modes in Figure 3.10b are dominant for the lock structure, the domestic houses, and parts of the greenhouse.



(a)



(b)

Figure 3.10: (a) Points which can be described mainly by the "Linear Mode" ( $EOF_1$ ). (b) Points that can be described mainly by the "Annual" mode ( $EOF_2$ ). The columns of  $V$  in Eq. (3.13) were analyzed as described in Section 3.4.1. The points were color coded with the absolute amount of their weights. A high negative value is represented as a high value.





## Chapter 4

# Monitoring of Single Buildings

Schunert et al. (2012) and Gernhardt and Bamler (2015) intensively investigated the distribution and cause of Persistent Scatterer (PS) points on buildings and other man-made structures. Costantini et al. (2014); Bianchini et al. (2015); Zhu et al. (2018) and Costantini et al. (2018) have carried out single building deformation monitoring based on various space-born Synthetic Aperture Radar (SAR) sources. Through this research it is evident that single building monitoring, is possible with high-resolution SAR satellites. Such SAR missions with a ground sampling distance (GSD) of approximately  $1\text{ m} \times 1\text{ m}$  can not observe every point on the earth continuously. However, the wide availability of SAR images in archives and the upcoming SAR constellations of SAR satellites (see Table A1) make it possible for dense urban areas to be sampled continuously and affordable.

The so collected SAR data can be analyzed with standard Persistent Scatterer Interferometry (PSI) procedures. Due to the complex three-dimensional nature of buildings and their dynamic behavior, the PSI results have to be interpreted differently from the previously described wide areas in Chapter 3. As such, it is desirable to look at single houses rather than at the whole city in ones. The challenge of automatically segmenting a city-wide PSI point cloud into single houses is not trivial. With single houses, it can be assumed that some PS points lay on the same rigid structure and therefore move as an ensemble. Such points that show a correlated behavior can be grouped and treated as a redundant measurements of the same underlying deformation. The relative movement of such groups can be analyzed and compared. Such an investigation can reveal potentially dangerous movements, that can lead to ruptures or damage. Therefore possible interventions or other conflict resolutions can be discussed. If highly semantic models or digital twins of a building, such as Building Information Modeling (BIM) models are available, the found groups of PSI points can be assigned to specific parts of the building, such as single columns or slabs.

In the first section of this this chapter, a method for extracting PS points on individual buildings, based on OpenStreetMap (OSM) data is introduced. In the following sections, the focus is on the analysis of such single buildings. A pipeline to group PS points into clusters that show a correlated behavior over time is introduced. Followed by an algorithm that finds the optimal assignment between such groups and single parts from a structured 3d model e.g. from a BIM model. Finally we present some ideas on how to integrate the PS points, as a remote sensing source for building monitoring, into the Industry Foundation Classes (IFC) standard.

At the end of this chapter, experimental results using the proposed methods are shown. Here, the prior described methods are evaluated on actual data and a further comparison to ground-based measurements is conducted.

## 4.1 Extracting PS Points on Buildings

When looking at PS points on a single building, the first step is to identify the points that lay on the building of interest. This can be done manually by selecting the PS points in the city-wide PS point cloud. Limits are given by the accuracy of the estimated scatterer's lateral positions which is usually in the order of the pixel size. The height component is however typically less accurate (Chang and Hanssen, 2014). For relatively big buildings, a manual selection is feasible, but for an automated segmentation of the PS point cloud into single building instances for an entire city other approaches have to be considered.

The utilization of publicly accessible information is helpful in this situation. It can be generally stated that for most cities, map data exist that shows the outlines of individual buildings. In addition to the official cadaster files, it is also possible to use free data such as OSM.

### 4.1.1 City-wide Based on OpenStreetMap Footprints

OpenStreetMap (OSM) is a collaborative project to create a free editable map of the world (Goodchild, 2007). The map is made up of information from a variety of sources, including GPS devices, aerial photography, and government mapping surveys. The data is combined and made available under a Creative Commons license, allowing anyone to use, edit, and redistribute the data. OpenStreetMap has good coverage in cities around the world (Brovelli et al., 2016). In many cases, the documentation is more accurate and up-to-date than data from commercial providers (Fan et al., 2014). The OpenStreetMap community is constantly working to improve the map.

The data can be accessed by anyone who wishes to use it, provided that the source of the data is attributed and the OpenStreetMap Foundation's guidelines on data usage are followed. The data is available in several formats. Buildings usually contain, in addition to the perimeter, the height and the name of the facility. A unique assignment to each building is possible via the so-called OpenStreetMap ID.

To assign PS points to single buildings, OSM building footprints were used. Those are polygons that describe the outer perimeter of a building. Since the PS algorithm can determine a lateral position for each scatterer, a straightforward method to find PS points in a building's polygon would be a simple *in-polygon* query for each PS. This approach is shown in Schneider et al. (2020) by considering a buffer around each building.

In the following section, a more accurate approach is described. Here the building footprints are transferred into the SAR image geometry, where PS points can be easily associated with the buildings.

### 4.1.2 Reverse Geocoding of OpenStreetMap Footprints

To overcome the inaccuracy and issues of falsely assigned points from a simple *in-polygon* query, a *Reverse Geocoding* approach can be utilized. The goal hereby is to transfer the geodata, specifically the building footprints, into the SAR geometry. An overview of the workflow is shown in Figure 4.1. The main idea hereby is to use an existing commercial geocoding pipeline (SARMAP, 2014) to geocode two Look-up Tables (LuTs). The LuTs contain a series of unique identifier, one for each range and the other for each azimuth cell. After geocoding with a precise digital surface model (DSM), the so generated LuTs are used to transfer labels, respectively building footprints, into the master image range-azimuth geometry. This allows precise assignment for each PS point, without the need for the estimated UTM coordinates.

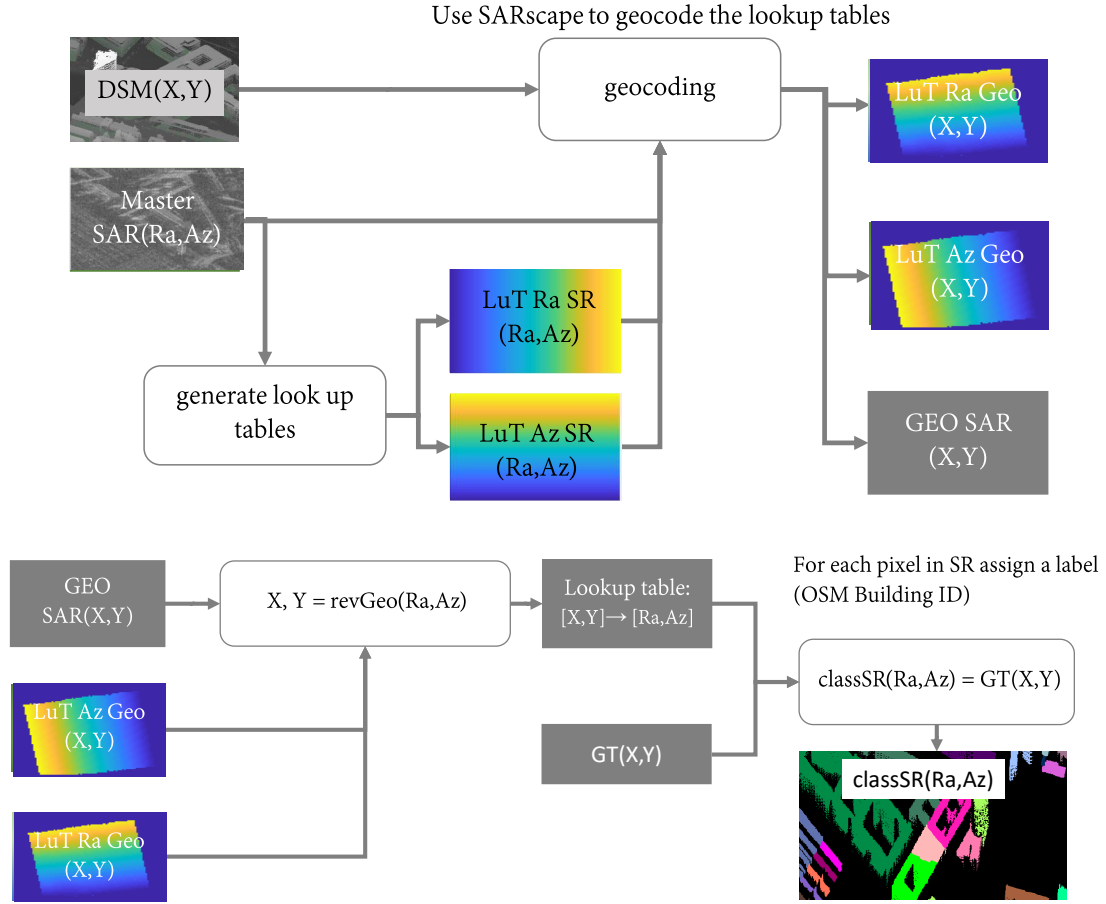


Figure 4.1: Workflow for Reverse Geocoding: Look-up Tables (LuTs) for Range and Azimuth are geocoded using the master image's SAR properties and a precise DSM. The geocoded LuTs are used to transform the ground truth (GT) from UTM to Slant-Range (SL) geometry, including SAR characteristics like foreshortening and layover.

The advantage of this pixel-wise method is that the distinction between neighboring buildings is sharper as compared to the *in-polygon* or buffer methods. It is worth mentioning that this approach is suitable to transform any geo-referenced data into range-azimuth geometry, for example, to generate training data for land classification applications with the advantage of using the undistorted SAR images.

Some experimental results for this reverse geocoding workflow are shown Section 4.5.1 in Figure 4.6. In Figure 4.7, the application of such slant-range data is demonstrated in a deep-learning-based land cover application that uses the undistorted slant-range SAR images.

## 4.2 Finding Groups of PS Points on a Building

When looking at the PS points on a building it can be assumed that some points lay on the same rigid structure. For example points on a wall or all the points on the same part of a roof. Such groups of points

can be expected to show a correlated deformation history. The amplitude of the movement might vary, but the overall time series should be similar since they originate from the same underlying process (e.g. thermal expansion and contraction or a more severe cause). Looking at such groups of points does have the benefit that they represent a redundant measurement of the mechanism that drives the behavior. Additionally, the spatial distribution of such groups gives insight into the rigid segments of a building. The boundaries of such neighboring groups are the spots where physically the most stress occurs, if adjacent groups move in different directions. At these boundaries, particular vigilance is required as tensions can occur.

In the following subsections, a technique that enables the detection of such groups or clusters of PS points is described. The consideration of the high-dimensional points in a deformation space with a custom distance metric combined with a non-linear dimension reduction and clustering allows for an automatic clustering process, that robustly can be transferred between different buildings and PS data sets.

#### 4.2.1 Deformation Space

The deformation histories or time series of the PS points are treated as points in a  $M$ -dimensional space, with a dimension for each acquisition date. The example in Figure 4.2 shows the embedding of such an exemplary deformation history with  $M = 3$ . Each point  $d_n \in \mathbb{R}^M$  is defined by the  $M$  measurements  $d$ :

$$d_n = [d_1^n \quad d_2^n \quad \dots \quad d_{M-1}^n \quad d_M^n]. \quad (4.1)$$

In order to have a metric for the Euclidean distance, also the Cartesian coordinates of the PS points are used. For the following steps, the coordinate tuple for each point is defined as:

$$X_n = [x_n \quad y_n \quad z_n]. \quad (4.2)$$

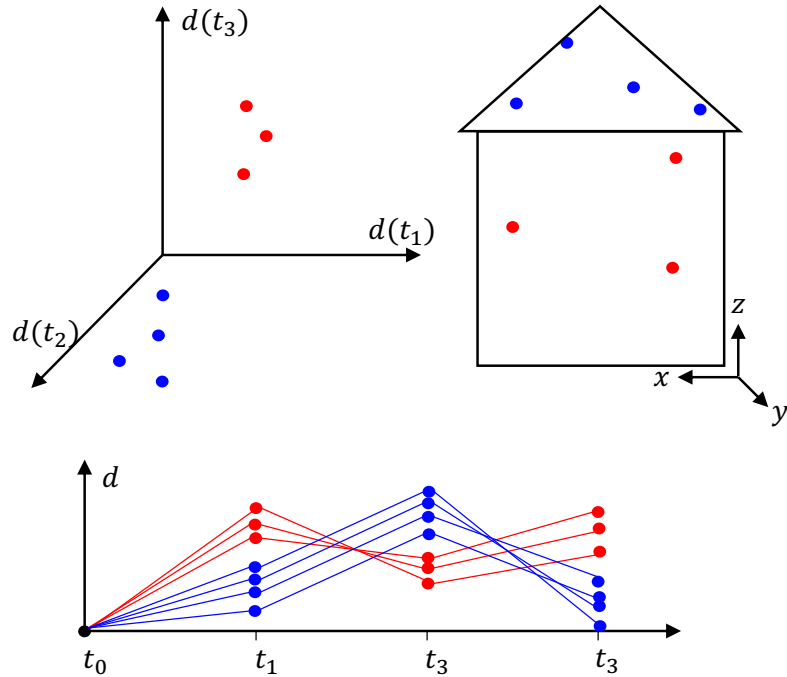


Figure 4.2: Representations of PS points. **Top right:** On building. **Bottom:** Deformation time series. **Top left:** In deformation space. The assumption is that points that lay on a rigid structure (e.g. the roof) show similar deformation behavior and therefore form clusters in deformation space.

### 4.2.2 Distance Metric

We use a combined distance  $D$  to describe the similarity of two PS points  $d_a$  and  $d_b$  in the  $M$ -dimensional deformation space.  $D$  is composed of the correlation distance  $D_C$  which is “1- minus the sample correlation” (see Eq. (4.4)) and the normalized Euclidean distance  $D_E$  between the PS points coordinates  $X_a$  and  $X_b$ . The normalization is achieved by dividing all distances by the maximum (See Eq. (4.6)). We combine  $D_E$  and  $D_C$  as follows:

$$D = \sqrt{D_C^2 + D_E^2 \cdot \lambda}. \quad (4.3)$$

The weight factor  $\lambda$  gives control over the cluster size on the object. This allows for an easy way to change the influence of the Euclidean distance in the implementation. For most experiments we set it to  $\lambda = 1$ .

The correlation distance  $D_C$  considers two points,  $d_a$  and  $d_b$ , to be close if their deformation behavior is correlated:

$$D_C = 1 - \text{corr}(d_a, d_b) \quad (4.4)$$

$$= 1 - \frac{(d_a - \bar{d}_a)(d_b - \bar{d}_b)^T}{\sqrt{(d_a - \bar{d}_a)(d_a - \bar{d}_a)^T} \cdot \sqrt{(d_b - \bar{d}_b)(d_b - \bar{d}_b)^T}} \quad (4.5)$$

where  $\bar{d}_a = \frac{1}{M} \sum_m^M d_m^a$   
 $\bar{d}_b = \frac{1}{M} \sum_m^M d_m^b$   
 and  $d_{a/b}$  as in Eq. (4.1).

Two time series display similar movement when their points lie close to each other in the  $D_C$  metric, regardless of different magnitudes of their amplitudes.

The normalized Euclidean distance  $D_E$  is the length of the line segment between the two points  $X_a$  and  $X_b$  divided by the maximal overall distance between all points:

$$D_E^2 = \frac{(x_a - x_b)^2 + (y_a - y_b)^2 + (z_a - z_b)^2}{D_{max}^2} \quad (4.6)$$

where  $D_{max}$  is the maximal Euclidean distance between all other points, with  $X_a$  defined as in Equation (4.2). This can be considered a normalization to account for different building sizes.

This hybrid definition of the distance considers points that show a similar deformation behavior and are not far in Euclidean space as close to each other.

### 4.2.3 Non-linear Dimension Reduction Based on a Hybrid-Distance Metric

As Allaoui et al. (2020) has shown, dimension reduction can drastically improve the performance of a subsequent clustering and minimizes the need for hyper-parameter tuning. We are aware that such dimensionality reduction might lead to an artificial split of bigger clusters. This however is an acceptable trade-off since we are interested in reliably finding clusters on a city-wide scale and can therefore not do hyper-parameter tuning for each individual building. This issue can be addressed by regrouping clusters as shown in Schneider and Soergel (2021b), however, these previous studies do not suggest a large benefit since they add more hyper-parameters to the workflow. Another advantage of this dimension reduction is the fixed amount of dimensions for the following steps, regardless of the length of the input time series.

The non-linear dimension reduction technique Uniform Manifold Approximation and Projection (UMAP) (McInnes et al., 2018) is used to reduce the  $(M + 3)$ -dimensions drastically into a two-dimensional space,

while preserving local neighborhoods. We use the distance metric  $D$  as defined in Equation (4.3) to model the relationship of the PS points in  $(M + 3)$ -dimensions.

For the UMAP hyper-parameter, we use random initialization so the initial embedding starts off with a random distribution and then iteratively finds a representative embedding from there on.

The *n-neighbors number* can be set between 5 and 20 as suggested in the original publication by McInnes et al. (2018). This parameter controls how UMAP balances local versus global structure in the data. It does this by constraining the size of the local neighborhood UMAP will analyze when attempting to learn the manifold structure of the data. This means that low values of *n-neighbors* will force UMAP to concentrate on very local structures (potentially to the detriment of the big picture), while large values will push UMAP to look at larger neighborhoods of each point, losing fine detail structure for the sake of getting the broader view of the data.

We empirically found a *minimum distance* of 0.3 suitable for this kind of data. The *minimum distance* parameter controls how closely UMAP is allowed to pack points together. It sets the minimum distance apart that points are allowed to be in the low-dimensional representation. This means that low values of minimum distance will result in clumpier embeddings. The low value chosen here preserves small clusters and finer topological structures.

As a distance metric in high dimensional space, we use the in Section 4.2.2 described hybrid distance metric. We found that an iteration of 5000 epochs reliably converges towards a stable embedding.

Other non-linear dimension reduction techniques such as t-distributed stochastic neighbor embedding (t-SNE) (van der Maaten and Hinton, 2008) yield similar results. The 2D deformation space can also be used to visualize the results of a clustering if the clustering was carried out in the high dimensions right away as shown by Schneider et al. (2020).

#### 4.2.4 Clustering Workflow

The low-dimensional embedding can be used as an input for a clustering pipeline. Since the exact number of clusters to be expected is not known, the density-based spatial clustering of applications with noise (DBSCAN) is used (Ester et al., 1996). The difficulty here is that the embedding is dimensionless and random, therefore the hyper-parameters of the clustering algorithm must always be determined anew. In the following subsection, it is described how the density level can be estimated via the core distance to arrive at a reliable automatic clustering procedure for this data. Each point in the embedded result is characterized by the core distance (CD) density estimator (Ankerst et al., 1999). All points that have a bigger CD than twice the median overall CD are excluded. This has the advantage that single points are sorted out very early and can not form *bridges* between the clusters in the following step. The remaining points are clustered with the DBSCAN with  $minPts = 5 + \lceil \frac{N}{1000} \rceil$  ( $N$  is the total number of PS points on the building). This choice of *minPts* has the effect that each cluster has a minimum size of 5. The hyperparameter  $\epsilon$  is set to the overall median of CD times 1.5. After the clustering is carried out, we remove points from each cluster if their correlation distance  $D_C$  (as defined in Eq. (4.4)) to the mean of the cluster is bigger than 0.3. This step removes points that do not show a correlated behavior but are physically very close to others. A schematic workflow with exemplary interim results is presented in Figure 4.3.

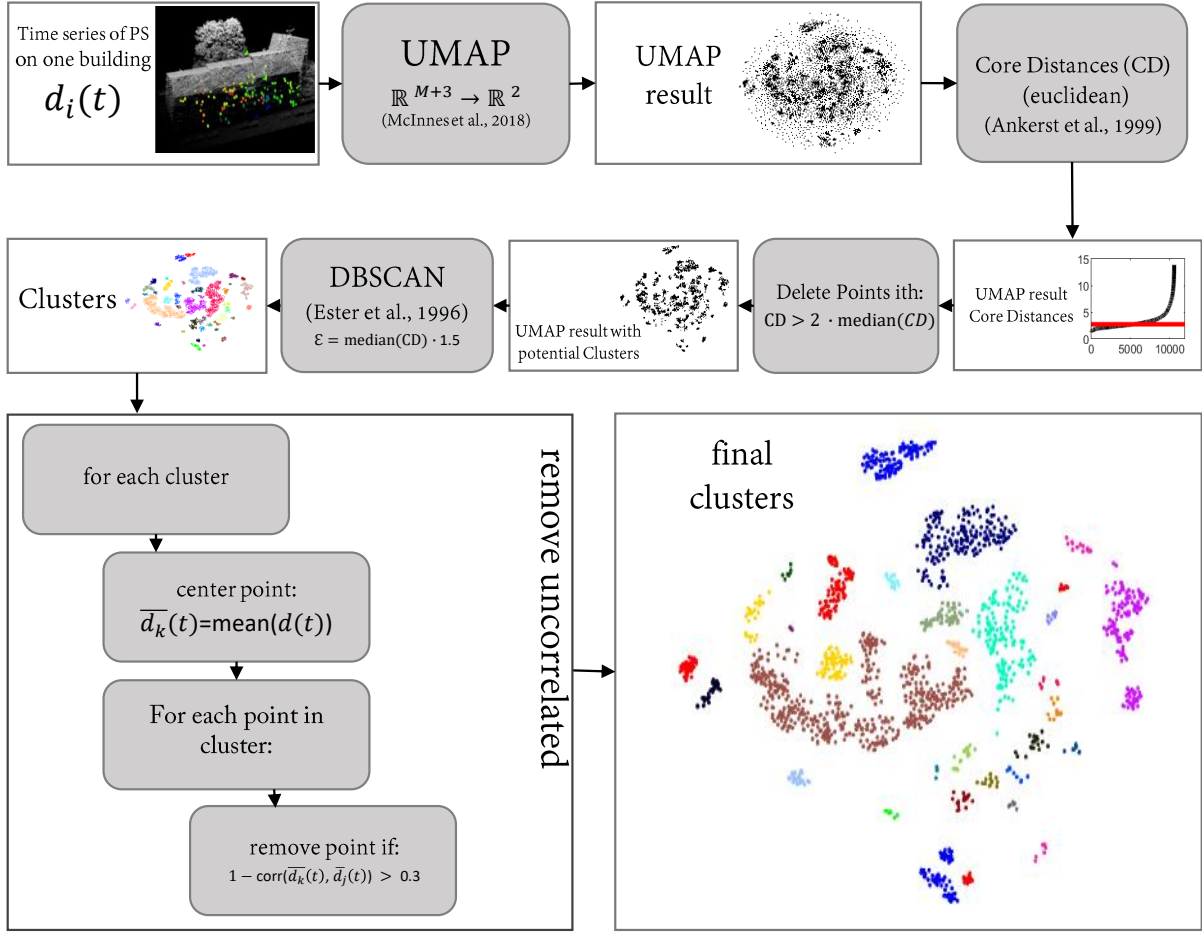


Figure 4.3: Schematic workflow of the clustering process. The  $(M + 3)$  dimensional PS points on a single building are embedded into a 2D space via UMAP. For all points in this embedding, the core distance  $CD$  is estimated. Points that have a  $CD$  greater than twice the overall median are then excluded. DBSCAN is then performed on the remaining points ( $\text{minPts}=5$ ,  $\epsilon = \text{median}(CD) \cdot 1.5$ ). For each point in each cluster, the distance to the cluster's center of gravity in the original  $M$ -dimensional deformation space is then calculated using the correlation-based distance  $D_C$ . Based on this metric, points are excluded from a cluster if their correlation distance is greater than an empirical threshold ( $D_C = 0.3$ ).

The final result of this clustering is a list of clusters. Each cluster can be interpreted as a set of similar time series. Results from experiments on different buildings are shown in Section 4.5.2.1 and 4.5.3.

#### 4.2.5 Influence of Different PSI Processing Chains

The here presented clustering method can be considered as a post processing to the actual PSI analysis. Thus it depends on the results of the PSI processing chain. The deformation model, the atmospheric and orbital phase screen (APS) removal step and the choice of interferogram pairs influences the resulting time series. To make sure that our approach works with different PSI sources some experiments were carried out with two different processing chains: SARscape 5.5 (SARMAP, 2014) and PSIG (Cuevas-González et al.,

2015) (see Tab. A2). Overall, it can be concluded that the post-processing technique described here produces results that are comparable when applied to data from various PSI implementations.

### 4.3 Comparing PS Groups to Ground-based Measurements

To evaluate the plausibility of PS groups found with the proposed methods, they can be compared with a ground bases monitoring method. This can be repeated leveling or automated total station measurements that are carried out every day. To compare the line-of-sight (LOS) measurements from PSI with such data, the leveling and total station data have to be projected to compensate for the effects of the one-dimensional observation of the PSI method.

#### 4.3.1 Line-of-Sight to Vertical Deformation

As illustrated in Figure 3.2a, the displacement time series represent the projection of the real deformation onto the satellite's radial LOS. As we want to compare the deformation to the precise leveling results, the assumption of a purely vertical movement is a suitable deformation model (Sanabria et al., 2014). Under these conditions, the LOS deformation time series  $d_n(t)$  can be transformed into the vertical deformations  $\Delta d_n(t)$  by scaling it with the cosine of the incidence angle  $\theta$ :

$$\Delta d_n = \frac{d_n(t)}{\cos(\theta)} . \quad (4.7)$$

The results of some experiments in which repeated leveling results are compared to the deformation histories of PS groups, are discussed in Section 4.5.2.2.

#### 4.3.2 Projection of 3 Dimensional Deformation to Line-of-sight Deformation

To compare the 3D measurements (e.g. a total station's continuous measurements with the PSI deformation histories) the 3D deformation vector has to be projected onto the line-of-sight (Vollrath et al., 2017).

The measured 3D movement for a given time is the vector  $d_{ts}(t) = [d_x(t) \ d_y(t) \ d_z(t)]$ , which can be projected onto the LOS to compare it with the PSI measurements. If the LOS is described by a vector  $r_{LOS}$  of the length 1, a dot product for each time step gives the projected time series:

$$d_n(t_i) = d_{ts}(t_i) \cdot r_{LOS} . \quad (4.8)$$

The results of some experiments are discussed in Section 4.5.2.2, in which continuous total station measurements are compared to the deformation histories of PS groups.

### 4.4 Integrating PS Points into Building Information Systems

In the previous section, we presented a workflow how to cluster PS points that represent different parts of a building. In this section, we discuss how to link these clusters to actual structures of the building using a Building Information Modeling (BIM). BIM offers a semantic model of a house, including static features like walls, beams, and slabs. BIM allows the creation and association of all kinds of information with such a building part. In the following, we will explain an approach that links the previously extracted PS clusters



to such structural elements from a BIM model. First, we need to create a correspondence between the point cloud and the BIM model. For example, a cluster of points that represents a wall can be linked to the corresponding wall in the model. This could be done by manually matching points from the point cloud to elements in the BIM model. Alternatively, we suggest use a registration algorithm to automatically align the point cloud and the BIM model and find the optimal assignment. Once we have a correspondence between the point cloud and the BIM model, we can link the clusters of points to the corresponding structural elements in the BIM model and store it in the industry-standard format IFC for further use.

#### 4.4.1 Building Information Systems

Building Information Modeling (BIM) is a process involving the generation and management of digital representations of physical and functional characteristics of places. These representations can be used to support a variety of tasks, such as planning, design, construction, and operation (Volk et al., 2014). The use of BIM technology can help organizations to improve the quality of their buildings, as well as reduce their construction and maintenance costs. BIM systems help to create and manage digital representations of physical places and their associated functional characteristics. These representations can be used to support a variety of tasks, such as planning, design, construction, and operations. There are a number of potential benefits of using BIM, such as improved communication and collaboration, increased accuracy and efficiency, and enhanced decision-making (Desogus et al., 2021; Khudhair et al., 2021; Delgado et al., 2017).

BIM is not exclusively used during and before the construction phase but also provides the foundation for a digital twin that accompanies the building throughout its lifetime. For our application such an *as-build* model is interesting. Such a digital twin can keep track of single parts and sensor data assigned to them, for example, to help with maintenance or to improve the efficiency of the building.

#### 4.4.2 Structured Meshes

A building's physical extension can be modeled as a polyhedral object. Polygon meshes are widely used in computer graphics to describe such objects. Meshes generally consist of vertices and faces. Vertices are defined by points in 3D space. Faces are described by at least 3 combined vertices. Additionally more per-face and/or per-vertex attributes, like material, color, or texture, can be defined. For geospatial data, meshes have several applications, such as a lean representation of densely textured city models or the appearance of buildings, for example in a BIM. In BIM, these 3D meshes represent the physical and functional characteristics of a building. Depending on the use case of the BIM, parts like walls, beams, pipes, segments and windows are modeled. By this semantic layer, it differentiates from an unstructured mesh. Such a structured mesh represents individual parts of a building. A model of this kind can be used to monitor a structure over its lifespan, by assigning measurements to parts and analyses of their interactions. Nowadays the existence of such *as-build* BIM data is still rare but in the near future BIM-based design, construction and maintenance will be the standard for complex projects (Isikdag, 2015).

In the following subsection, an approach that links PS clusters (Section 4.2.4) to single parts of the building is described. The main challenge here is that there might be multiple building parts covered by a single cluster. Therefore, their optimal assignment must be found.

#### 4.4.3 Cluster to Segment Assignment

Cluster to segment assignment aims to link each PS cluster to parts or segments of a structured mesh that describes the building.

The cluster-to-segment assignment workflow aims to treat the task as a one cluster to many segments (one-to-many) assignment problem. The goal is to assign each of the  $J$  segments to one of the  $I$  clusters. This means that one cluster can be assigned to multiple parts of a building. This is depicted in Figure 4.4.

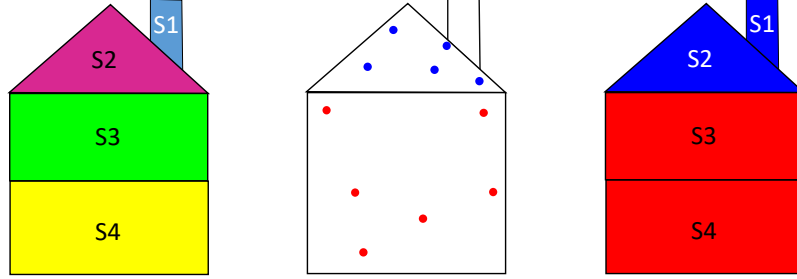


Figure 4.4: An example for the PS points clusters to building segments assignment problem. **Left:** A building with 4 segments. **Middle:** 2 PS Clusters are found on the building. **Right:** The optimal assignment.

To find the optimal assignment, we use a variant of the Hungarian algorithm (Kuhn, 1955). Generally speaking, this algorithm finds the optimal one-to-one assignment for a given bipartite graph. The graph is described by a qualification matrix  $Q$  that models the cost for each association. For our method, the original approach is altered to allow the mapping of one cluster to many segments.

For the qualification or cost matrix  $Q$ , we use “one minus the normalized vertex neighbor count”  $1 - ||C||$  for each segment. For each vertex in the mesh, we count the class (cluster) appearance in the 10 closest PS points ( $k = 10$ ). For each segment, this count is normalized by the total count.

To achieve a one-to-many assignment, we concatenate the qualification matrix  $Q$  several times.

A short example for  $I = 3$  clusters and  $J = 5$  segment is given in the following (Eq. (4.9) to (4.14)):

The vertices in  $Segment_1$  have 50  $k$ -closest neighbors to  $Cluster_1$ , 20  $k$ -closest neighbors to  $Cluster_2$  and no neighboring PS points to  $Cluster_3$  etc. this leads to the connection Matrix  $C$ :

$$C = \left( \begin{array}{c|ccccc} & Segment_1 & Segment_2 & Segment_3 & Segment_4 & Segment_5 \\ \hline Cluster_1 & 50 & 0 & 30 & 60 & 0 \\ Cluster_2 & 20 & 20 & 10 & 30 & 0 \\ Cluster_3 & 0 & 10 & 10 & 40 & 60 \end{array} \right) \quad (4.9)$$

By dividing the columns of  $C$  through the sum to normalize them, we can compensate for parts with higher vertex counts in the normalized cost matrix connection matrix  $||C||$ :

$$||C|| = \left( \begin{array}{c|ccccc} & Segment_1 & Segment_2 & Segment_3 & Segment_4 & Segment_5 \\ \hline Cluster_1 & 0.71 & 0.0 & 0.60 & 0.46 & 0.00 \\ Cluster_2 & 0.29 & 0.67 & 0.20 & 0.23 & 0.00 \\ Cluster_3 & 0.0 & 0.33 & 0.20 & 0.31 & 1.00 \end{array} \right) \quad (4.10)$$

If we would use  $1 - ||C||$  as the qualification matrix in the Hungarian algorithm, we would not be able to assign one cluster to multiple segments. We overcome this limitation by concatenating the  $||C||$  vertically multiple times (two times in this example):

$$Q = 1 - \begin{bmatrix} ||C|| \\ ||C|| \end{bmatrix} \quad (4.11)$$

$$= 1 - \begin{pmatrix} & Segment_1 & Segment_2 & Segment_3 & Segment_4 & Segment_5 \\ Cluster_1 & 0.71 & 0.0 & 0.60 & 0.46 & 0.00 \\ Cluster_2 & 0.29 & 0.67 & 0.20 & 0.23 & 0.00 \\ Cluster_3 & 0.0 & 0.33 & 0.20 & 0.31 & 1.00 \\ Cluster'_1 & 0.71 & 0.0 & 0.60 & 0.46 & 0.00 \\ Cluster'_2 & 0.29 & 0.67 & 0.20 & 0.23 & 0.00 \\ Cluster'_3 & 0.0 & 0.33 & 0.20 & 0.31 & 1.00 \end{pmatrix} \quad (4.12)$$

Following Kuhn (1955), the optimal assignment for this example is:

	<i>Segment</i> <sub>1</sub>	<i>Segment</i> <sub>2</sub>	<i>Segment</i> <sub>3</sub>	<i>Segment</i> <sub>4</sub>	<i>Segment</i> <sub>5</sub>
<i>Cluster</i> <sub>1</sub>	0	0	1	0	0
<i>Cluster</i> <sub>2</sub>	0	0	0	0	0
<i>Cluster</i> <sub>3</sub>	0	0	0	0	1
<i>Cluster'</i> <sub>1</sub>	1	0	0	0	0
<i>Cluster'</i> <sub>2</sub>	0	1	0	0	0
<i>Cluster'</i> <sub>3</sub>	0	0	0	1	0

(4.13)

By considering the assignments for the concatenated rows, the final result becomes:

	<i>Segment</i> <sub>1</sub>	<i>Segment</i> <sub>2</sub>	<i>Segment</i> <sub>3</sub>	<i>Segment</i> <sub>4</sub>	<i>Segment</i> <sub>5</sub>
<i>Cluster</i> <sub>1</sub>	1	0	1	0	0
<i>Cluster</i> <sub>2</sub>	0	1	0	0	0
<i>Cluster</i> <sub>3</sub>	0	0	0	1	1

(4.14)

Note how the number of concatenations (2 in the above example) allows multiple assignments of each cluster to different segments. In our experiments in Section 4.5.4, we set this number of concatenations to 10, but suitable values are depending on how detailed the building is modeled. However, the detailed model used in our experiments in Section 4.5.5 was processed with this value set to 50.

#### 4.4.4 Quality Metric

The quality of the assignment depends on how well the mesh segments represent the borders of the clusters. If multiple clusters fall on one segment, the corresponding column in  $||C||$  (4.10) would have a wide distribution. Such a histogram of class affiliation can be described by entropy. We calculate a per segment-entropy from  $||C||$  as follows:

$$H(Segment_j) = - \sum_{i=1}^I ||C_{i,j}|| \cdot \log_2(||C_{i,j}||) \quad . \quad (4.15)$$

High entropy values indicate poor cluster-segment allocation, whereby low values indicate a good match.

Some experiments that link a structured mesh with extracted PS clusters are presented in Section 4.5.4.

#### 4.4.5 Industry Foundation Classes

The Industry Foundation Classes (IFC) data model is the international convention for Building Information Modeling (BIM) (Vanlande et al., 2008; Laakso et al., 2012). It defines a standard schema for the description of the geometry and metadata of building objects. The geometry of the building components can be represented as triangulated surfaces or as boundary representation (BREP) solids. The IFC data model has a rich set of attributes for describing the geometry of the building components. For example, there are attributes for defining the wall thickness, the exact 3D shape of the wall, the material properties of the wall, etc. The IFC schema is designed to be independent of any particular software or BIM system.

The IFC data model is a structural data model that captures the geometry, topology, and semantics of a building. The model is based on the concept of a *spatial structure element*, which is an entity that has a spatial extent and a set of properties. The properties of a spatial structure element can be other spatial structure elements, in which case the element is a *container* for other elements.

We use the IFC format to model the structural elements of a building. Structural elements in a building include walls, floors, columns, beams, slabs, and roofs. We create our on SAR specific *Property Sets* to integrate the PSI measurements into the IFC file format.

#### 4.4.6 Integration with Industry Foundation Classes (IFC)

The benefit of incorporating satellite-based monitoring data into the IFC format is that all stakeholders involved in a building can access the monitoring data immediately and thoroughly. The previously found PS groups can now be assigned to individual elements. The IFC format offers a flexible data structure and allows the introduction of new data types such as monitoring data. Smarsly and Tauscher (2015); Delgado et al. (2017) and (Desogus et al., 2021) have carried out tests on the integration of structural monitoring data from ground-based sensor networks. They proposed to create a new property set for these data types. IFC offers the possibility to add such property sets afterward for elements of the building. We follow a similar approach.

The workflow to do this starts with a clustered PS point cloud as specified in Section 4.2.4. Ideally, only points that are on the building should be included in this point cloud (Section 4.1.2). In addition, there is a BIM model in IFC format, which describes the individual statically relevant components of the building. Through an optimal assignment, as specified in Section 4.4.3, the relationship between each cluster to one or more building components is established. The result is then saved as a new property set for each part of the building. Figure 4.5 shows an overview of this workflow.

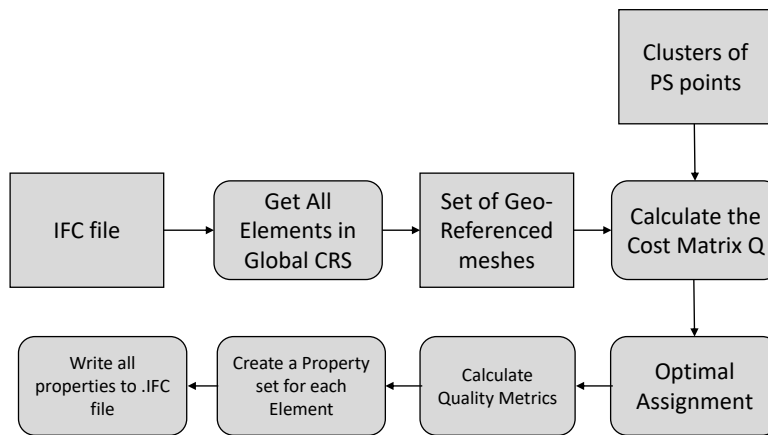


Figure 4.5: Schematic workflow of the optimal assignment process. After the assignment, the characteristics are saved as a new property set in the IFC file.

IFC allows custom property sets to be defined, which can be attached to objects in a model. These properties are stored in an IFC file and can be used to exchange information about the objects between different applications. To combine clusters of persistent scatterers with a BIM model, we suggest creating a new *InSAR Property Set* that contains the following attributes:

**Meta Data about the SAR data** Information about the mission such as name, acquisition mode and the start and end date along the PSI processing algorithm. Also, a single flag, that indicates if valid SAR data is available has proven to be useful.

**Line-of-sight** The direction from where the scene was observed. This is important to interpret any movements.

**Velocity** The line-of-sight (LOS) velocity is a simplified metric that shows the linear regression of the deformation history.

**Time Series** The actual deformation history as a time series. Since we assigned a cluster of similar moving PS points to the building part, the centroid in deformation space, respectively the mean time series of a cluster, is used here.

**Quality metric** The quality metric to describe the uncertainty of the assignment as described in Section 4.4.4.

**Cluster and PS IDs** For each cluster, the ID of the PS points it consists of is also stored. This enables visualization of the original PS point cloud superimposed with the building.

## 4.5 Experiments

In this chapter, a workflow to automatically extract PS points on single buildings was introduced. Further, it was discussed how points on a rigid structure form clusters in a *deformation space* due to their correlated deformation behavior. We described a workflow that uses non-linear dimension reduction techniques to structure the deformation space to cluster more reliably without parameter tuning. Finally, we present an algorithm that allows the assignment of PS clusters to a structured mesh e.g. a BIM model, that represents the structural elements of a building.

In the following subsections, we want to show the application of the methods presented in this chapter on some actual examples.

### 4.5.1 Reverse Geocoding

Section 4.1.2 described the reverse geocoding approach. It offers the possibility to use an existing geocoding pipeline for SAR images, to transfer any two-dimensional data into the range - azimuth geometry of a SAR the images. The data set we use for the experiments is a High-Resolution SpotLight image from TerraSAR-X with a GSD of  $1m \times 1m$ . We use Airborne Laser Scanning (ALS) data with more than 1 point per  $m^2$  to create a digital surface model (DSM) of the same urban scene. The (forward) geocoding algorithm is from *SARscape 5.5* was utilized.

#### 4.5.1.1 Unique Mapping of PS Points to Buildings

Figure 4.6 shows an example for this. Here building footprints from OSM data are transferred into the SAR geometry. Since we have the exact range-azimuth coordinate for each Persistent Scatterer (PS), this can then be used to extract all PS points that lay on an individual building without any ambiguity.

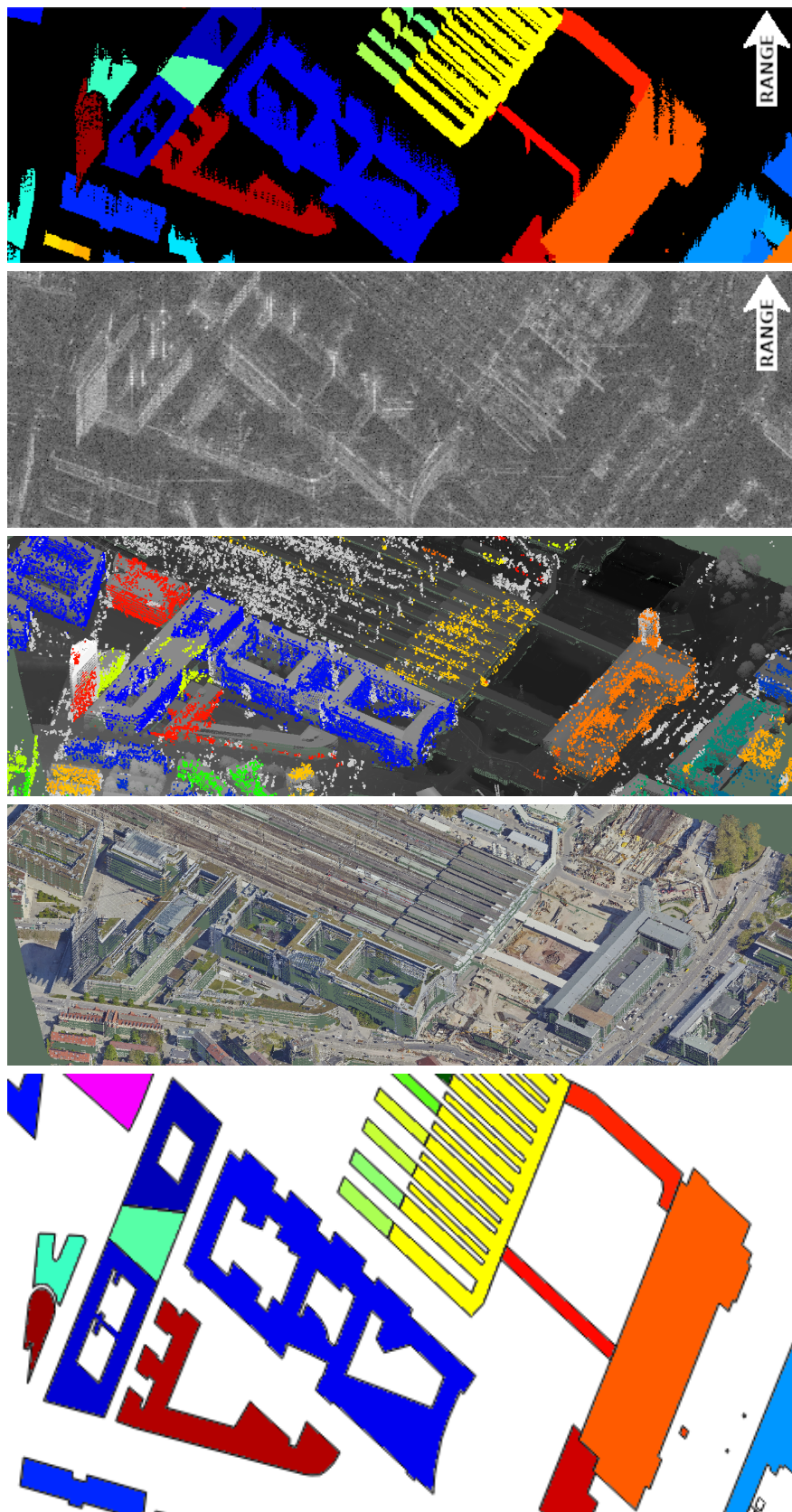


Figure 4.6: Examples of reverse geocoding. From top to bottom: Building instances in Slant-Range (SL) geometry; Amplitude SAR image in SL; 3D view of DSM with PS points (one color per building); 3D view of RGB ALS point cloud; Building footprints from Open Street Map.



#### 4.5.1.2 Labels in Slant-Range Geometry

For deep-learning-based land cover classification applications, the availability of training data is crucial. Land cover ground truth such as the footprints of buildings is widely available, for example, in OSM. However, they are in a geographic coordinate system and can not serve as ground truth in a SAR image. The in Section 4.1.2 presented workflow allows transferring such labels into the SAR geometry. This enables the raw SAR data to be used for the training but more important for the inference. In the inference stage, no precise DSM is needed. The HED-UNet proposed by Heidler et al. (2022) is an openly available state-of-the-art segmentation framework. This architecture can be considered as a standard approach to such a task. Here it was trained on a  $4\text{ km} \times 5\text{ km}$  High-Resolution-Spotlight TerraSAR-X image with a GSD of  $1\text{ m} \times 1\text{ m}$ . The target domain is a binary image of OSM building footprints in the slant-range geometry.

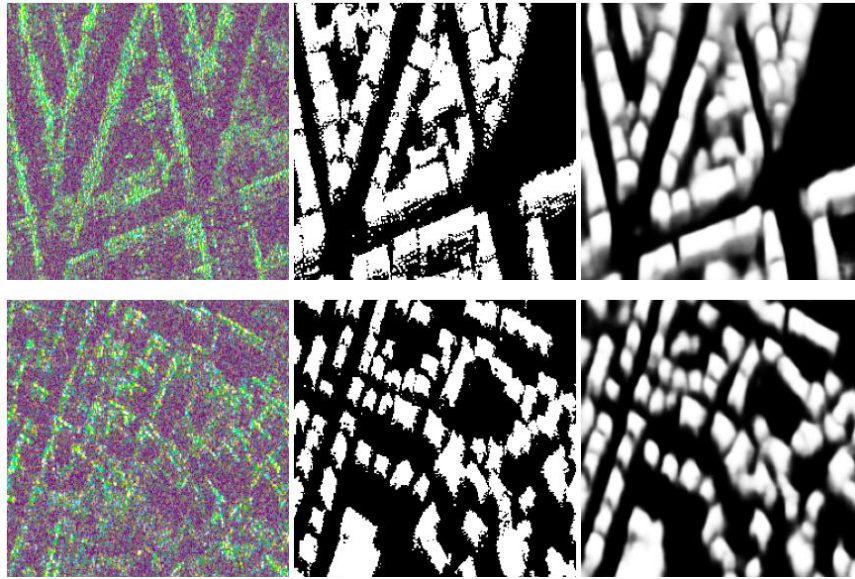


Figure 4.7: Application of the unaltered HED-UNet approach on SAR images in slant-range geometry to segment buildings. Left: SAR image (dB of amplitude), middle: ground truth, right: prediction.

The focus of this experiment was on simple proof of concept. The validation accuracy for this pixel-wise classification is about 88%.

#### 4.5.2 Comparing PS Groups to Ground-based Measurements

For our case study, we chose a building close to the construction site of a new underground train station. Due to the construction work, continuous precise leveling and 3D total station measurements been executed over several years at this site. In Figure 4.8, we show the PS point cloud next to the LIDAR representation of the building and the positions of the leveling points and the 3D total station prism on the building.

The data set here was a stack of 88 High-Resolution SpotLight images from TerraSAR-X with a GSD of  $1\text{ m} \times 1\text{ m}$ . The SAR data was captured between fall 2016 and summer 2019. We used *SARscape 5.5* for the PSI processing.



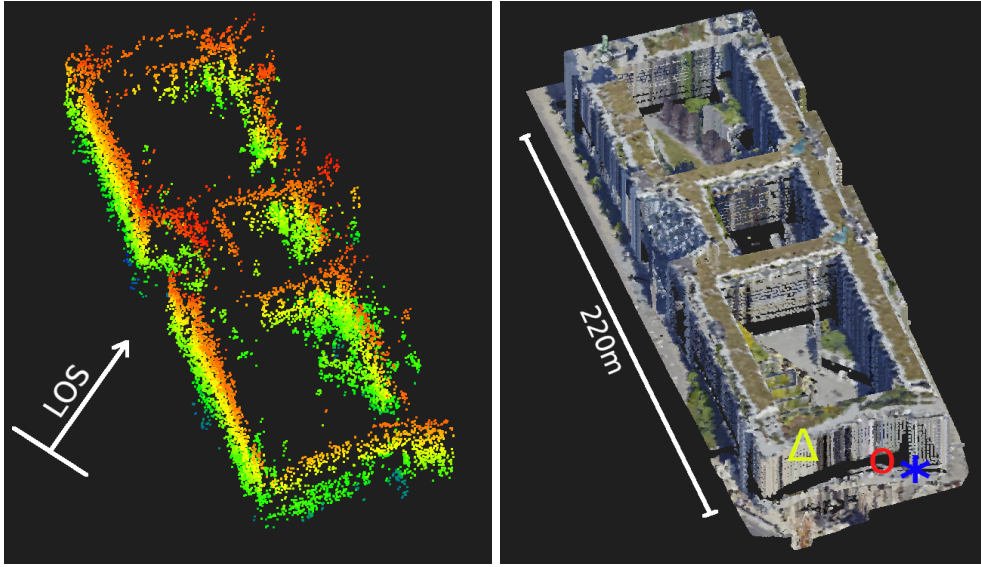


Figure 4.8: Left: 13000 PS Points on the building (height-color-coded, segmented from OSM footprint). Right: ALS point cloud of the building. The leveling points are marked by  $\circ$  and  $*$ , and the position of the 3D total-station's prism is marked by  $\Delta$ . The corresponding time series are shown in Figure 4.12 and 4.11a, along with the deformation histories of the closest PS point clusters.

#### 4.5.2.1 Clustering of PS Points

Clusters in deformation space are visualized via a t-SNE embedding in Figure 4.9b, one can nicely see the difference between embedded clusters and the results from DBSCAN. Figure 4.9a shows the position of the extracted clusters on the building. Even though no spatial information has been considered in the clustering process, the clusters segment the building into rigid structures. The choice of DBSCAN parameter  $\epsilon$  has a big impact on the segmentation results and has to be estimated for each building via the k-distance graph. Figure 4.10 shows the corresponding time series of each cluster, as well as a temperature profile on the building. The single displacement histories show a clear correlation with the temperature, but also linear trends and single change events can be detected for some clusters. The clusters in Figures 4.9a and 4.9b correspond to the time series in Figure 4.10 and should be considered in respect to each other.

It must be noted here that the clustering process shown was done directly on the high dimensional data and not in the embedding as proposed in Section 4.2.4. The dimension reduction by t-SNE is only used to visualize the clusters. This is also the reason why some of the clusters were not found in 2d and others appear very large. This experiment visualized the advantages and downside of a preliminary non linear dimension reduction: more clusters can be found but they might be split into sub groups by the embedding.

In Figure 4.12 we compare the ground truth to the closest cluster to the leveling points (Figure 4.10c). Both, the deformation history extracted from PSI and the measured deformation on the ground correlate in the overlapping time window. The difference in amplitude, especially from the fast movement in December 2018 can be explained by a non-vertical deformation direction.

In Figure 4.11a, we show the 3D total station results. The 3D deformation measurements have been projected from a local reference frame onto the LOS (see Figure 4.11b). The resulting deformation matches the cluster on the corresponding part of the building.

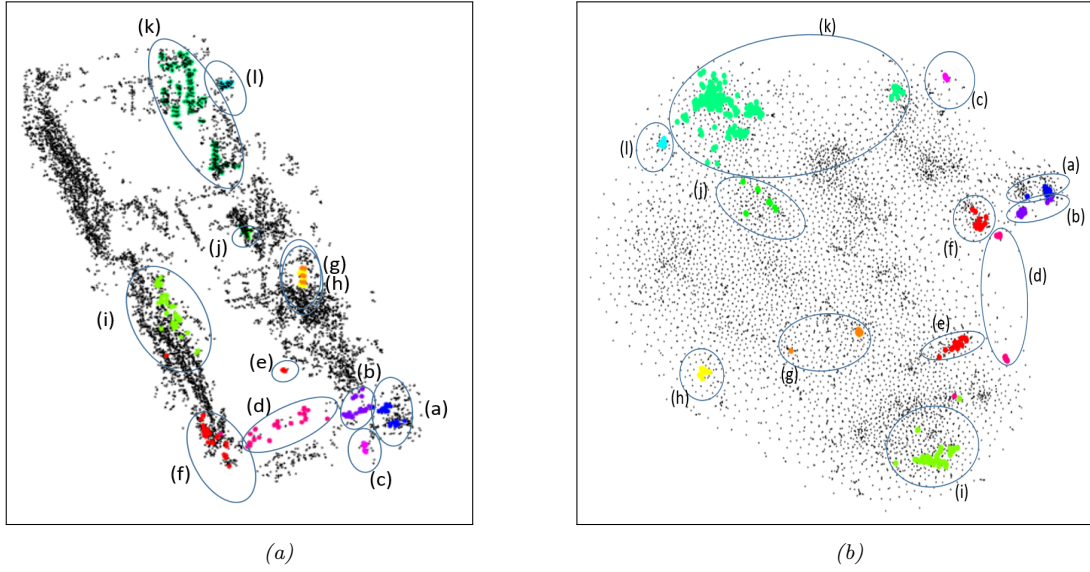


Figure 4.9: (a) Distribution of clusters on a building. Each group and color indicates a different cluster. (b) Clusters from DBSCAN in the 2D t-SNE embedding. The related time series for each cluster are shown in Figure 4.10. The PS point distribution on the building is shown in Figure 4.9a.

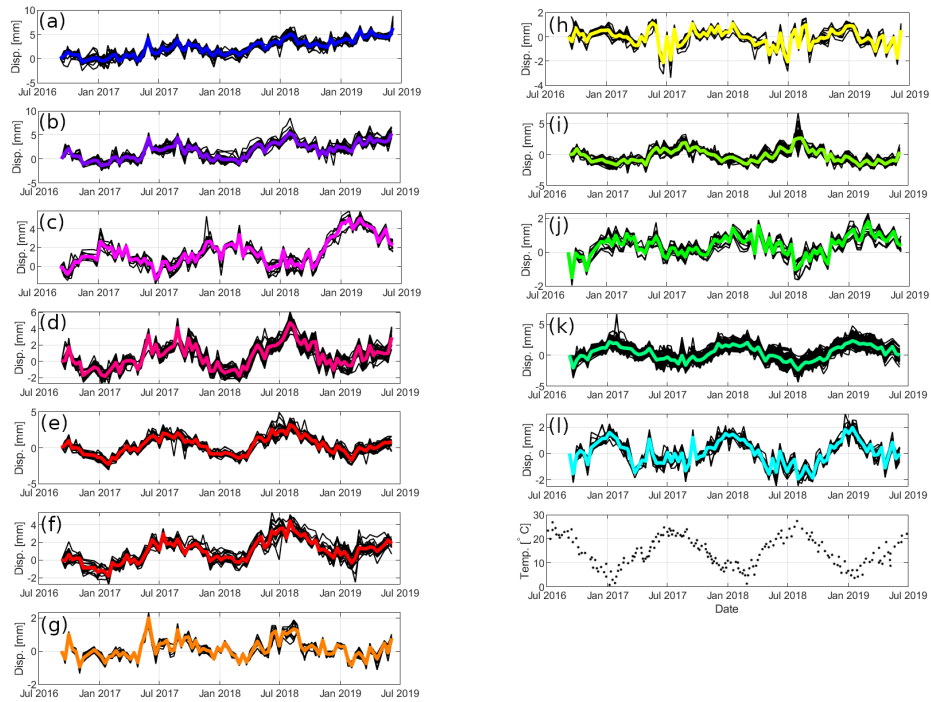
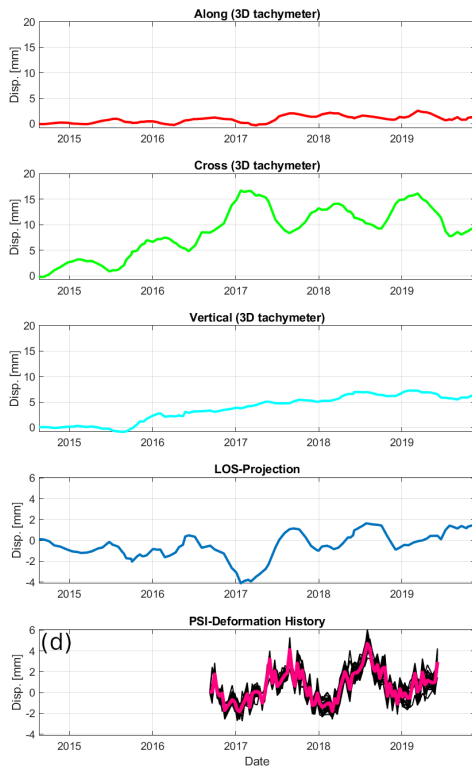


Figure 4.10: Center points of the clusters in Figure 4.9a as time series in the matching color. This center represents the average of all members of the cluster, which are showed in black. The temperature of the building is shown in the right bottom plot. Plot (c) is compared to the precise leveling ground truth in Figure 4.12. Plot (d) is compared to the LOS projection of the 3D tachymeter in Figure 4.11a.

#### 4.5.2.2 Comparison with Total Station Measurements

Continuous 3D total station measurements were carried out for the front part of the building (See Figure 4.8). By projection this movement onto the LOS of the satellite as outlined in Section 4.3.2, we can compare it to the closest cluster.



(a)



(b)

Figure 4.11: (a) Deformation time series from the 3D total-station. The location of the prism is shown in Figure 4.8. The direction *cross* points towards the wall, *along* indicates horizontal movements along the wall and *vertical* shows the down-up movement (see (b)). *LOS-Projection* shows the projection of this displacement onto the satellite's line-of-sight direction. It matches the displacement history of the closest cluster (d) in Figure 4.10. (b) Top view on the PS point cloud and the orientation of the local reference frame used by the 3D total station. *LOS* indicates the direction of the satellite's line-of-sight (LOS).

Figure 4.11a shows a comparison to the closest PS cluster. It can be observed that the LOS projection of the total station correlates with the PSI measurements.

### 4.5.2.3 Comparison with Leveling

Weekly leveling campaigns were carried out to monitor the subsidence of the front part of the test building (See Figure 4.8). As outlined in Section 4.3.1, we can compare it to the closest cluster by scaling the closest cluster. This is done in Figure 4.12.

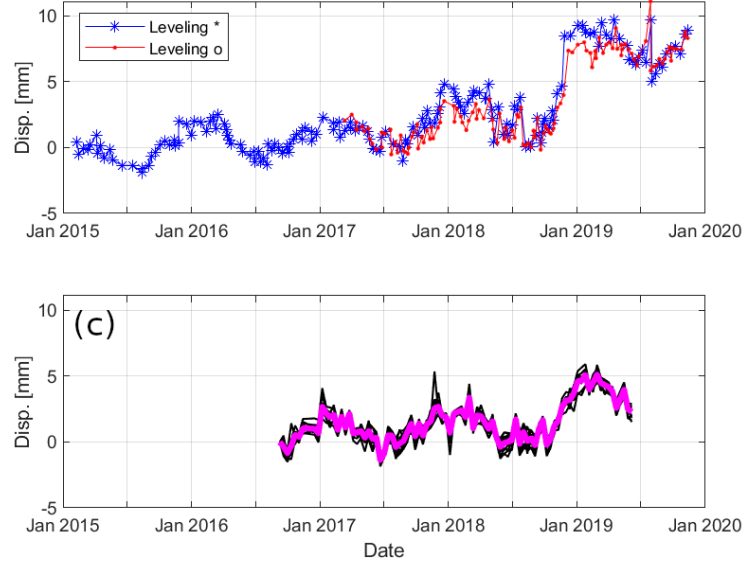


Figure 4.12: Top: Ground truth from two precise leveling points underneath the building (see Fig. 4.8). Bottom: Deformation of the (spatially) closest PSI cluster (c) to the leveling points.

For the overlapping time span, both measurements show the same behavior. The rise in the end of 2018 can be observed with both methods.

### 4.5.3 Detecting Damage

In the following subsection, an example of a building that shows a rupture on a date is shown. The consideration of groups of points gives an insight into which part of the building was undergoing which deformation. The SAR data is High-Resolution Spotlight with a 1 x 1 m. GSD The studied house consists of 3 adjacent multistory buildings.

To evaluate the benefit of looking at clusters instead of single points, we choose a building complex that suffers damage from underground construction activities. 185 PS points can be assigned to the building. The UMAP plot with the resulting clusters is presented in Figure 4.13, along with the PS points on the building and the corresponding time series. The clustering workflow shows that the deformation behavior can be grouped in several areas that follow unique deformation behaviors.

In the time series in Figure 4.13, we can observe a relief rupture (Fig. 4.14) in spring 2019 that coincides with reports about compression injections in late 2018 due to an ongoing tunnel project under this area (SWR, 2019). The time series also indicate a stabilization of these structures in the following year.

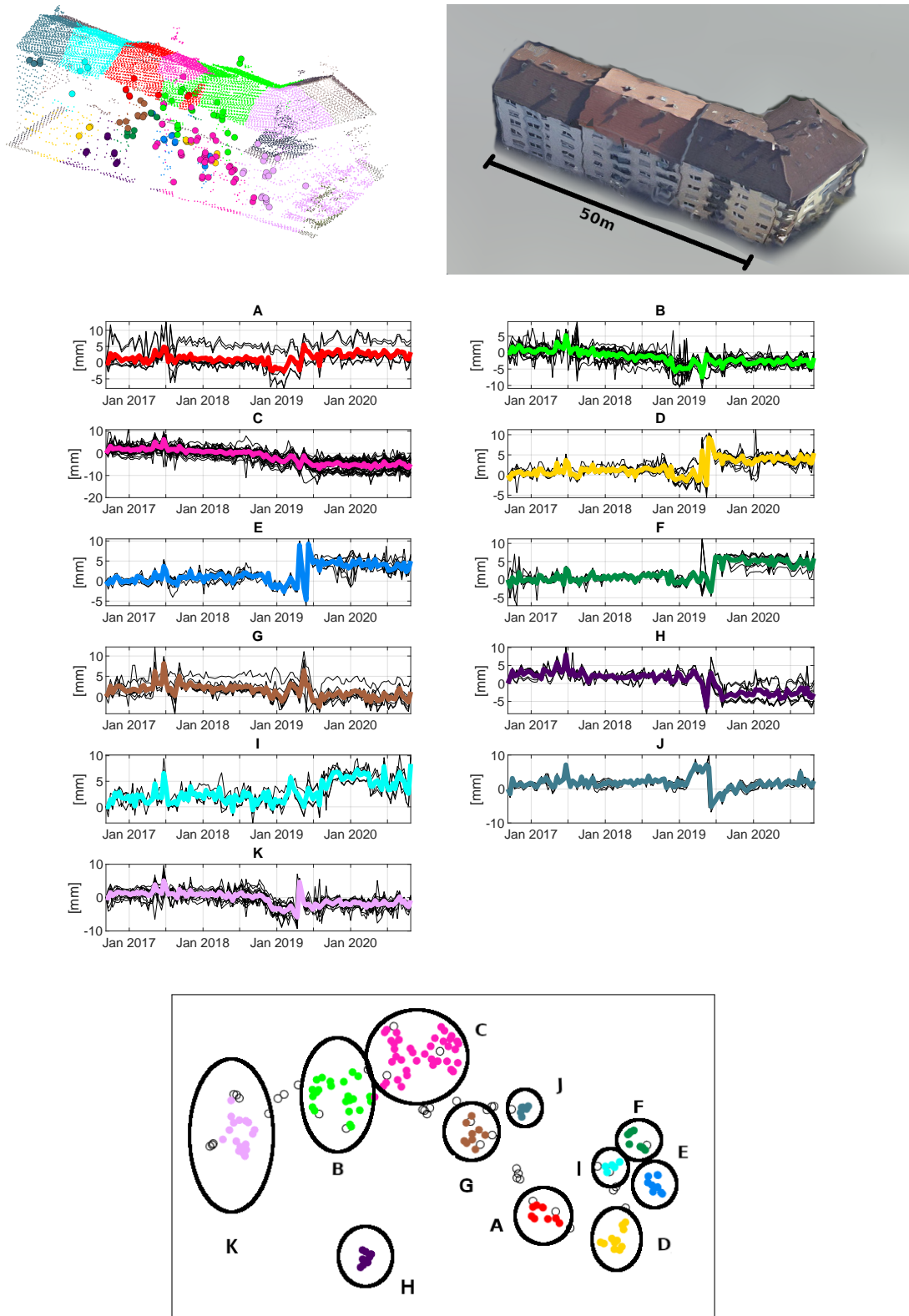


**Figure 4.13: Left: First from the top:** Spatial distribution of 144 PS points on a small urban building complex, superimposed with an ALS-point cloud. The colors indicate the membership to the extracted clusters. **Second from the top:** textured mesh representation of the same building complex. **The time series A to K** show the deformation behavior for each of the extracted clusters. The bold, colored graph represents the centroid of the cluster in deformation space as defined in Figure 4.2. **Bottom:** UMAP's low-dimensional embedding of all PS points. The color and letter correspond to the time series and spatial distribution above. Points that were excluded during the clustering process (see Section 4.2.4) are drawn in white.





Figure 4.14: Cracks in the building started to appear at the same time (May 2019) as the observed release rupture in the time series (Fig. 4.13).

The cracks observed shown in Figure 4.14 lay between cluster **D** and **H**. Those two PS clusters show a diametrical movement. The results of this experiment encourage the idea that the considerations of clusters and their potential movement gradients on borders can help to detect and predict damage on buildings.

The previously presented experiments suggest that individual building elements, which move independently of each other, can be represented by PSI groups. Such groups offer the possibility to have redundant measurements of one and the same deformation. In this way, it is also possible to decide which motion profiles are important and which only occur at individual locations and thus may not affect the entire structure. In general, it can be said that no unusual motion patterns, such as harmful deformations, are necessary to group PS points. The characteristic temperature-induced expansion is already sufficient for this. In the following, such PS groups are combined with mesh data.

#### 4.5.4 Linking Groups to Structures in Mesh

To leverage PSI measurements with the semantics from structured meshes, the optimal assignment has to be carried out. In the following example, two manually segmented meshes are combined with PSI data from HighResolution Spotlight TerraSAR-X images over Berlin, Germany. The Figure 4.16a shows the segmented mesh of the *Reichstag* building. Each segment is represented with a different color. In Figure 4.15, the found clusters are shown.

Figure 4.16 depicts the results and quality of the cluster to segment assignment, as described in Section 4.4.3. Figure 4.17 shows the time series for each cluster. No hazardous movements can be detected on the here analyzed building.

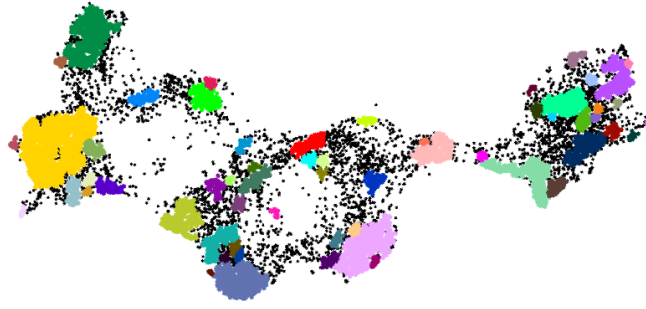


Figure 4.15: Embedding of the PS points in 2d deformations space. The extracted clusters are shown in different colors.

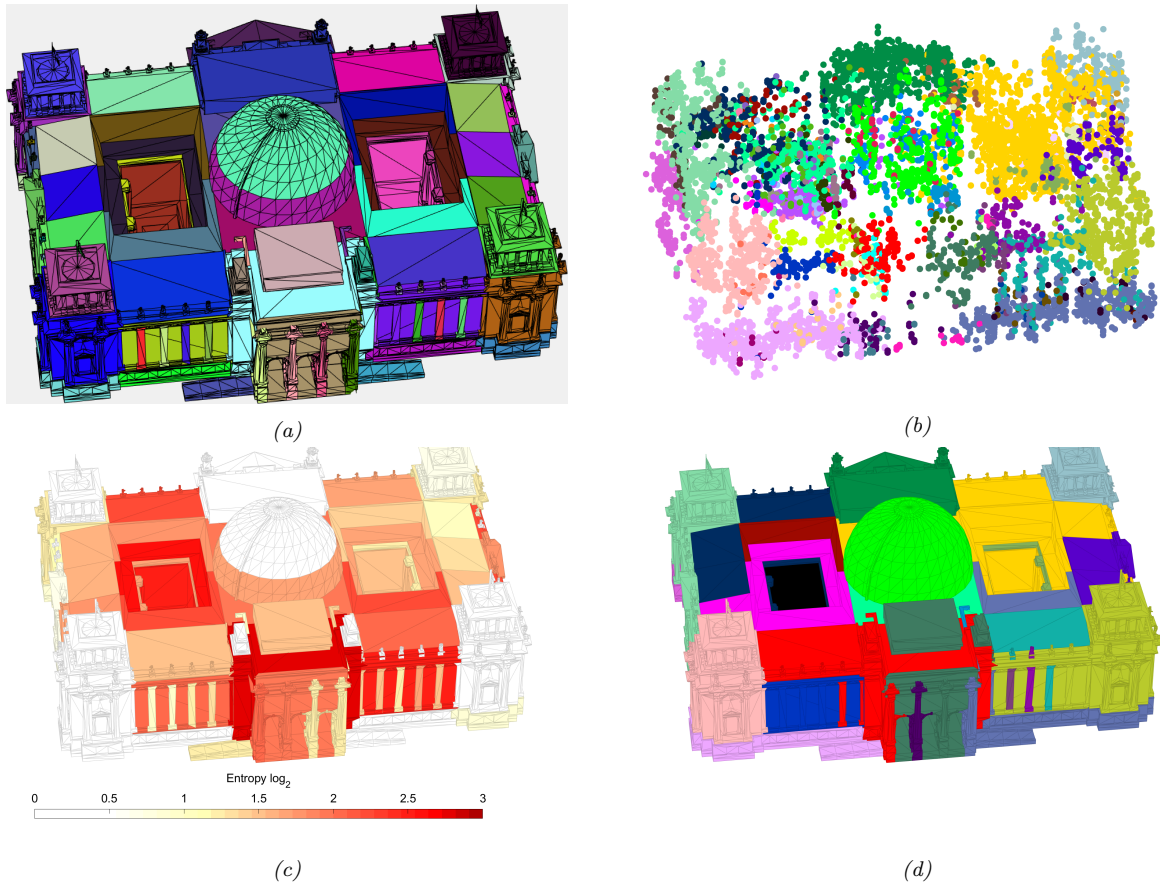


Figure 4.16: (a) Manually segmented mesh of the *Berlin Reichstag* - each color indicates an individual segment. (b) PS point on *Reichstag* all the colors correspond to Figure 4.15 and 4.17. (d) Mesh colored with the assigned PS cluster. (c) Entropy for each mesh segment. A lower entropy indicates a good match between the cluster and the segment.

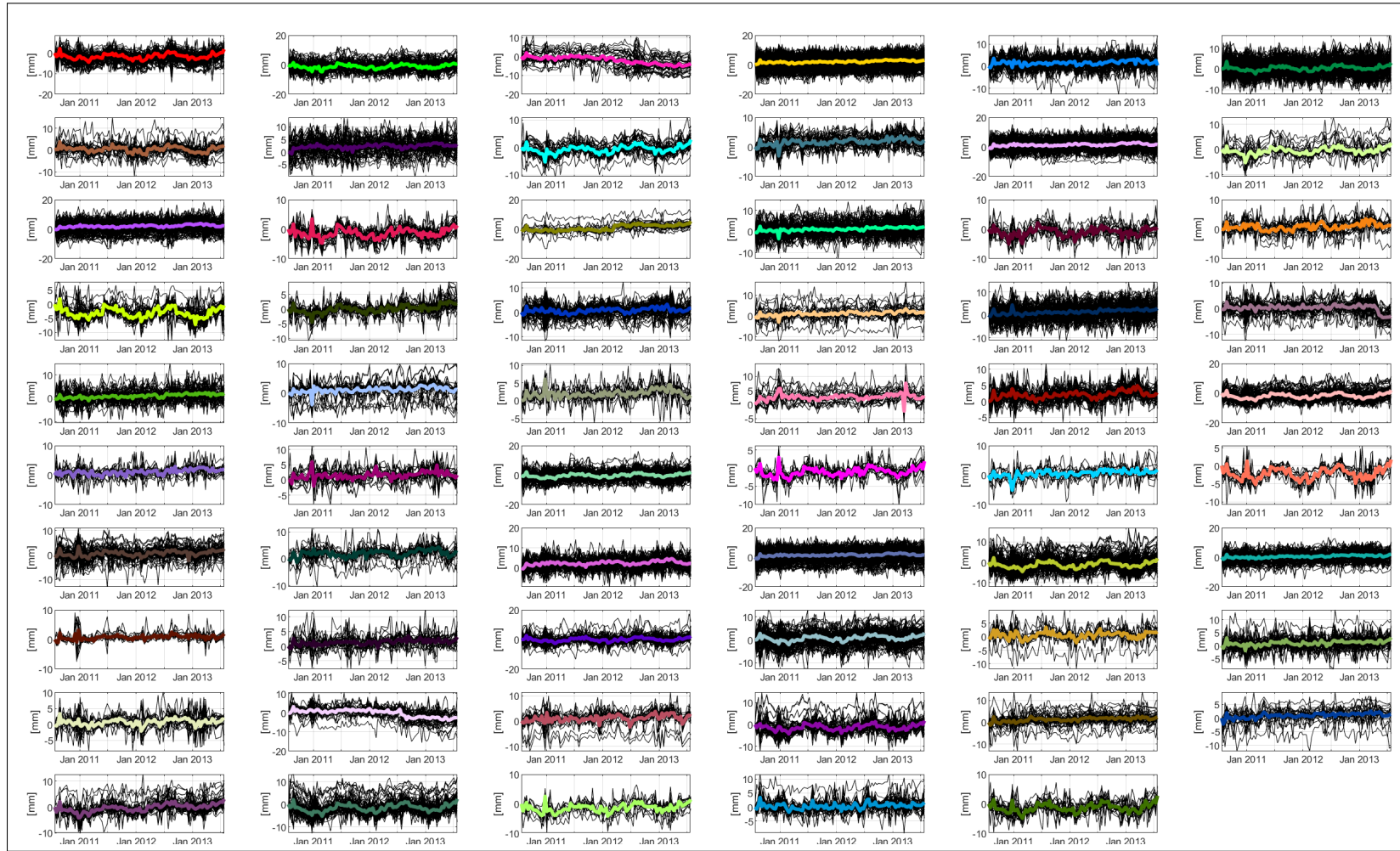


Figure 4.17: Time series for the extracted PS clusters. The colored line indicates the mean deformation for the cluster. The colors correspond to Figure 4.15 and 4.16.



In Figure 4.18 a second building, namely the *Berlin Central Station*, is shown along with a structured mesh. The PS clusters were assigned to the mesh.

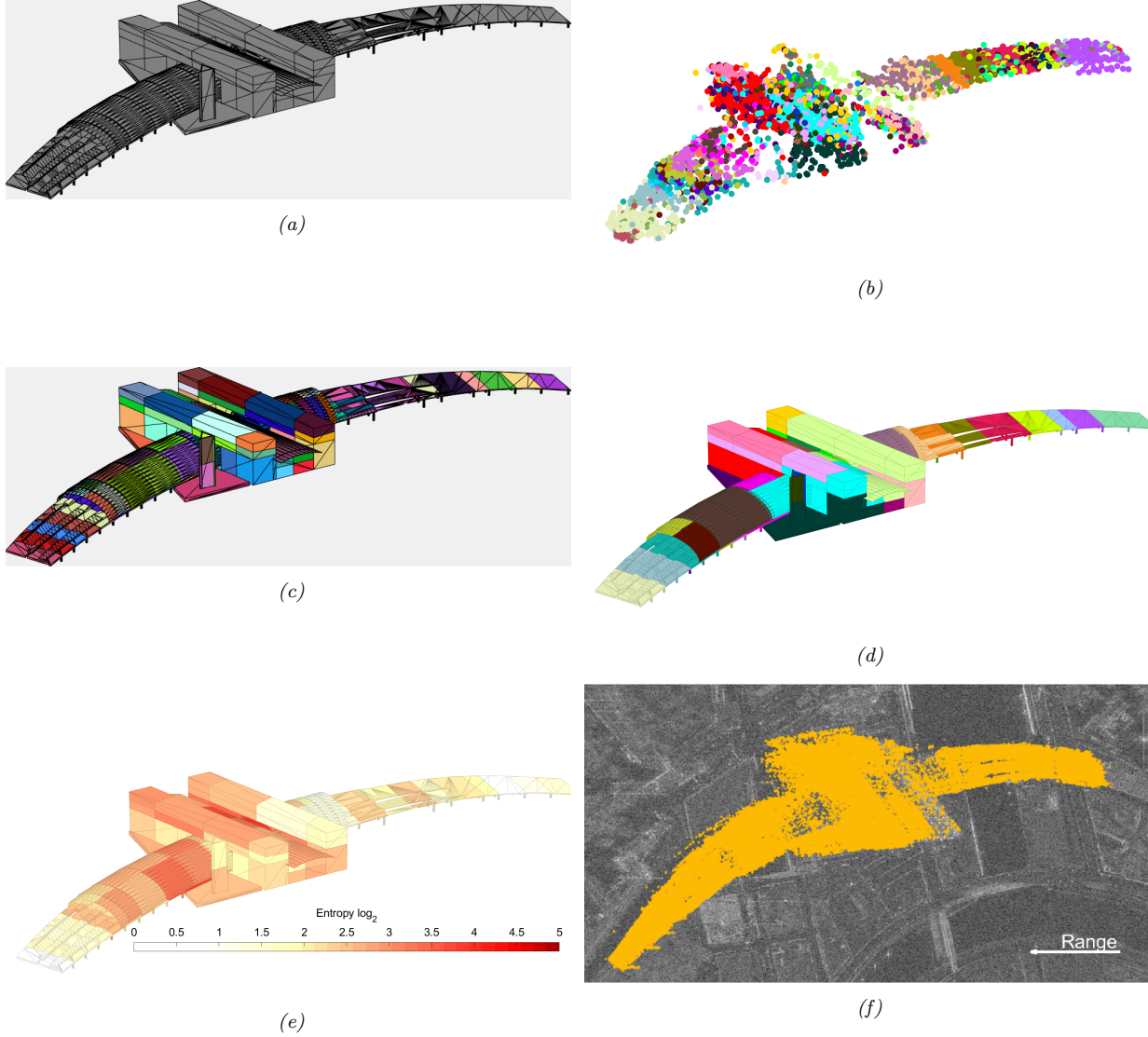


Figure 4.18: (f) shows the PS points on the building super imposed with the SAR image in slant-range geometry. (a) shows the mesh of the building and (c) the segments of the mesh. (b) shows the result from the clustering of the PS points. (d) shows the result from the cluster to segment assignment, whereby (e) depicts the quality of the assignment (lower values are better).

This second example demonstrates how the clusters effectively represent the individual components of the bridge on both sides of the building. By assigning each element to a cluster, the bridge is accurately depicted in the segments. The bridge presented in Figure 4.18 has expansion joints that enable a degree of freedom for thermal expansion. Those elements are also present in the resulting clusters. This assignment

works very well, as it allows the viewer to clearly identify each element of the bridge. Furthermore, the use of clusters helps to emphasize the overall structure of the bridge, making the representation of the bridge much easier to understand.

#### 4.5.5 Assigning Information to IFC File

In this last example of the chapter, the proposed workflow is demonstrated on an “as build” BIM model. This means that the model represents the actual state of the building. Structural elements like slabs, walls, and beams are represented as individual segments. The SAR data set is a stack of 28 High-Resolution SpotLight images from TerraSAR-X with a GSD of  $1m \times 1m$ . The SAR data was captured between spring 2018 and fall 2019. We used SARscape 5.5 for the PSI evaluation.

Figure 4.19b shows the building in an orthophoto, while Figure 4.19a shows the same scene in a SAR amplitude image.



Figure 4.19: (a) Amplitude SAR image of the building of interest. (b) An orthophoto of the same scene.

In Figure 4.20a, a visualization of the BIM model is shown. Figure 4.20b shows the PS points and cluster found on the building. The different colors indicate clusters of PS points that have a correlated deformation behavior (Section 4.2.4). In Figure 4.20c, the different segments of the model are shown. The BIM model was created based on the actual structural elements of the building. Each major roof part, slab, beam, and the wall is represented in the model. Figure 4.20d depicts the result of the assignment process. Each cluster from (b) was assigned to one or more segments in the in (c).

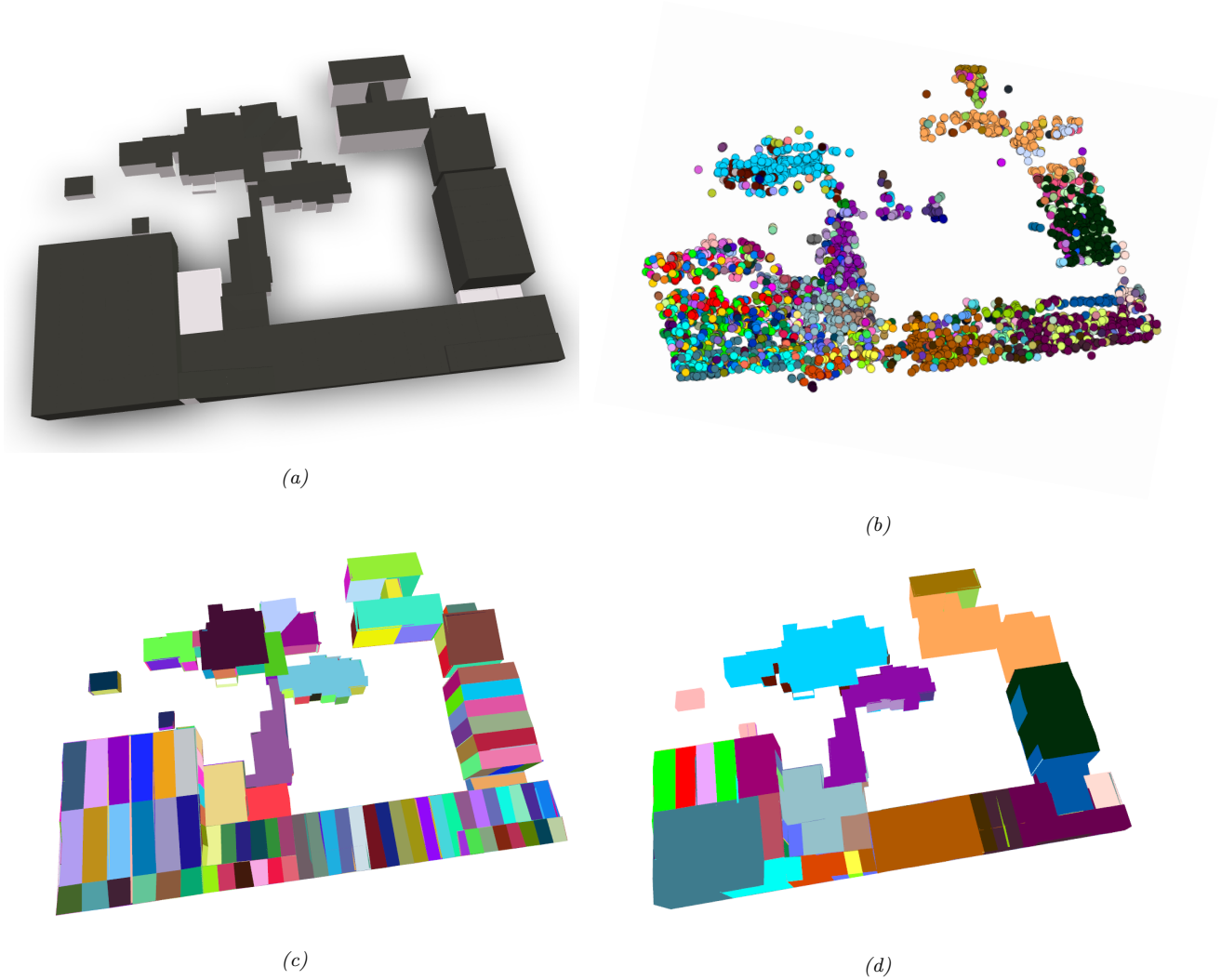


Figure 4.20: PS Points on the test site, a large sports facility in Germany. (a) shows the BIM model and (c) the individual segments. (b) shows the PS clusters and (d) the assignment to the segments.

#### 4.5.6 Conclusion

These experiments show that PS points from high-resolution SAR data form clusters of similar moving points in a deformation space. It is possible to use a non-linear dimension reduction technique and a robust clustering algorithm to group these points automatically without hyper-parameter tuning. An association between those groups of points and structural elements of the building can be made. A BIM model is particularly useful in this process, since it represents all building parts individually. The information from the PSI analysis can be integrated into the BIM, using the Industry Foundation Classes (IFC) file format.



## Chapter 5

# Web Platforms

In Chapter 3, we showed that Persistent Scatterer Interferometry (PSI) can be used to monitor large-scale deformations like mining or construction-induced subsidence. In Chapter 4 we showed that the PSI method is suitable to monitor single buildings. The resulting Persistent Scatterer (PS) point clouds can be grouped into points that show a correlated behavior. Such groups can then be combined with 3D models of a building, for example a Building Information Modeling (BIM) model. It is important to communicate the information gained from the Differential Interferometric Synthetic Aperture Radar (DInSAR) analysis to other stakeholders. Here non-SAR experts are involved in the process. This is especially true for building monitoring, as it is not feasible to print large complex 4D data sets and display them as 2D projections. It can also not be expected from every decision-maker to have the specialized software and computing power that is needed to display and analyze the augmented building models. Approaches need to be developed in order to better present DInSAR data, such as web-based tools or the integration into industry standard programs. This will help experts of other domains to get a better overall picture of the situation.

This chapter presents some possible solutions to these problems. The focus here is on browser-based decision support systems (DSSs). In contrast to a geographic information system (GIS), such a system is a specialized tool to present specific aspects of a data set and allows the user only a limited data input. DSS refers to a computer-based information system that supports decision-making activities. It integrates tools, models, and procedures, which communicate with an information processing system. According to Sharifi (1999); Boulila et al. (2017), in remote sensing, the challenge for DSS is not providing enough information, but how to screen the information and select which is relevant to the decision.

In the first section, some tools and frameworks are briefly introduced, that proved as helpful for the development of such a web-based platform. In the main part, some aspects of the visualization concepts are presented. It is discussed which elements of the data sets are presented in a way so that a good and intuitive user experience can be provided. The focus here is on the one hand on the presentation of PS points in a large area, along with other multimodal sensor data, that help to contextualize the PS points. On the other hand, the in Chapter 4 discussed method of linking PS points with 3D models is adopted here. Finally, we present some implementations of experimental DSSs.

### 5.1 Tools

When developing an application for the browser, certain standard tools, such as frameworks and processing concepts are used. In this section, some of those tools are introduced. This introduction does not claim to be a comprehensive guide. It rather should give an overview of some tools and concepts.

### 5.1.1 Web Development with HTML and JavaScript

The standard markup language for creating web pages is HyperText Markup Language (HTML). Using the scripting language JavaScript, one can make dynamic web sites. These two technologies can be combined to develop a web-based DSS.

Web pages can be built with HTML as their structure and JavaScript as their interactive component. Many specialized JavaScript libraries are available, enabling a wide range of applications. For instance, effective 3D graphics that allow users to view and interact with a building model in real-time or the efficient tiling of enormous geospatial data sets that allow only the necessary tiles and subsets to be streamed to the browser via a server.

### 5.1.2 Tiling of large Datasets

For large geospatial datasets such as point clouds with millions of points or orthophotos, it is not performative to initially download the entire data in order to display it. Tile-based mapping systems apply a logical tile scheme to map positions on the Earth to a two-dimensional surface. This surface is divided into a series of regularly spaced grids, which defines the discrete addressing of map tiles. The system also generates multiple zoom levels of tiles and provides a translation method between tile addresses and a continuous geospatial coordinate system (Sample and Ioup, 2010). The advantage of such a data representation is that it enables the system only to request and transfer the necessary data receptively to the currently displayed tile at an appropriate zoom level. In order to be able to have a tile-based representation of a data set, it has to be reprocessed and stored in tiles and zoom levels. One example of such a tiling scheme is the *Cesium JS* standard (Cozzi and Ring, 2011). It offers the possibility to store 3D data, such as point clouds, orthophotos, and 3D models as hierarchical tiles on a server and handles the tile streaming. The library allows the visualization of geo-data in 3D and is able to use the geo-reference of the data sets to display them in a common coordinate system.

### 5.1.3 Processing of IFC files

The Industry Foundation Classes (IFC) file structure is based on the STEP data modeling language. It is a hierarchical data structure, with the main header followed by a number of sections. The header contains information about the IFC file, including its version number, the date and time it was created, and a list of the sections that follow. The sections themselves contain the data for the IFC file, organized into a number of different types. The most common types are entities, which represent the objects in the IFC file, and properties, which contain information about those objects.

To query a specific property, like the shape of an element, the entire file has to be processed. When writing for example a new property set to a segment all relative references must be considered. *IfcOpenShell* is an open source software library that helps software developers work with the IFC file format (<http://ifcopenshell.org/>). The library can be used natively in C++ or in Python via a wrapper.

We use *IfcOpenShell* to do the actual interaction with the IFC file. We apply it to obtain the geometry of each relevant building component. Then, after we found the optimal assignment to PS groups the library is used to write the new property set (see section 4.4.6) to the file.

## 5.2 Important Properties and Graphical User Interface Elements

The here discussed decision support systems (DSSs) aim to provide certain aspects of PSI data to experts. In the case of the visualization of a large area, those users are usually civil engineers and geophysicists. The decision-makers in a building monitoring process are typically the building owner or manager, the architect or designer, civil engineers, and the occupants.

In this section, we suggest several graphical user interface elements and visualization concepts to display the PSI data, jointly with data from other sources in an informative fashion.

### 5.2.1 Single PS Points

Here, PS points are the core elements that represent the actual measured data. In large area applications like ground motion service or the display of subsidence areas, the single points can be displayed color coded with certain properties like their line-of-sight velocity or the deformation on a specific date.

#### 5.2.1.1 Velocity

The velocity with which a PS point moves towards or away from the satellite is one of the most important pieces of information that the PSI technique offers. When displaying a large field of PS points it is common to color code them with their velocity. This can show important areas, that undergo a sinking or uplift at a glance. However, non-linear movements can not be depicted by the velocity. For example, a point that is stable over many years and suddenly shows a rapid uplift in a few months would have a relatively low average velocity over the entire time span.

#### 5.2.1.2 Displacement on Date

Sometimes the deformation of a point on a certain date is of interest. A slider that represents the time enables the user to step through all available time steps. The visualization of the points changes accordingly this allows identifying points that change on the same date visually.

#### 5.2.1.3 Time Series

Each point has not only a position in space but also its deformation history, which can be described as a time series. In-ground deformation services like the European Ground Motion Service (EGMS) and the Ground Motion Service Germany (BBD) each point can be selected and its estimated deformation history can be displayed. It can also be that certain interesting points and areas are highlighted to guide the user's attention.

#### 5.2.1.4 Show Line-of-Sight Direction

For non-SAR experts the measurement of the line-of-sight (LOS) deformation (Section 3.3) might be not intuitive. They have to be informed and guided to interpret such data. For this purpose, the LOS vector can be superimposed on the 3D view. If several data sets from different observation directions are available, this can be emphasized by color separation.

### 5.2.1.5 Information from Other Sources

A sparse Persistent Scatterer (PS) point cloud might be hard to interpret. PSI is an opportunistic process. The exact position of the occurrence of PS points can not be predicted. In general, it can be said that the scatterers are mainly located on buildings and other man-made structures. When showing such a point cloud, some features like streets and houses are densely populated with PS points. Other parts of the scene like vegetation do only show a rare appearance of Persistent Scatterer, if at all. The interpretability of such a PS point cloud is enhanced if it is superimposed with other geo-data. This augmentation might allow new insight into deformation patterns that are depicted by the PS points.

**Base-map** When picturing PS points on a large area, it is good practice to draw them on top of the base map. Here an orthophoto of the area is useful since it shows all kinds of features and is relatively easy to interpret, even for not experienced users. If no orthophoto is available, a SAR amplitude image can be used. One has to be aware that a geo-coded SAR image is not always very clear to interpret by the users.

When working with such a base map in a web-based tool, a tiling of the data is inevitable. Orthophotos that cover a large area with a high ground sampling distance (GSD) exceed the hundreds of megabytes quickly.

**Mesh** The combination of a PS point cloud with a mesh that represents the scene allows the interpretation and exact localization of the scatters origin, for example on buildings and other complex structures. Such a mesh can originate from dense image matching of aerial photography or Airborne Laser Scanning (ALS). Another suitable option is the application of a 3D city model. Simple 3D city models with a low level of detail are often available for major cities. A *Level of Detail 1* model can also be derived from OpenStreetMap (OSM) building footprints and an average building height. The use of a non-detailed city model makes single houses distinguishable for a user. In the PS point cloud, the seam between two houses might not be recognizable. Here, applying a simple model is beneficial.

**Colorized Airborne Laser Scanning Point Cloud** Point clouds from Airborne Laser Scanning (ALS) are another readily accessible data collection for metropolitan regions. ALS campaigns are carried out regularly by authorities and are often available under a public data policy. By projecting the color information of an orthophoto onto the LiDAR data, an easy-to-interpret model of a city can be created. Such a model, when superimposed with the PS point cloud, enhances interpretability greatly.

When visualizing these data jointly, one possibility is to color the ALS points with features of the neighboring PS points, for example the LOS, velocity or a color that indicates the cluster. This directly links the PS points to the building and helps to interpret the spatial patterns of the appearance of some features. For example, if a certain deformation behavior is present on one side of the facade. The colorization can be done dynamically for example if the user selects a certain cluster, the linked ALS points change their color.

The storage size of ALS point clouds on the server can be large. Here the use of tiles and detail levels is inevitable if a responsive performance on the client side is desired.

## 5.2.2 Clusters and 3D Building Models

In Chapter 4 an approach was introduced that links groups of PS point to elements from a BIM model. We discussed the benefits of combining the semantics of a detailed model of a building with the deformation measurements from PSI. In Section 4.4.6 we suggested an approach to integrate such measurements into



the Industry Foundation Classes (IFC) file format. The IFC files can be interpreted by all standard CAD construction and BIM software. In industry-standard software, it is impossible to view the suggested custom SAR property set and its attributes, which are derived from the PSI data, in a sufficient manner. Therefore visualization tools have to be developed that are tailored to show the specific properties of the monitoring. In this section, we suggest and discuss some design elements of such a decision support system (DSS).

#### **5.2.2.1 The Geometry of the BIM**

Naturally, a DSS that is designed to show monitoring data linked to a BIM model, should be able to display the BIM model. The IFC file format contains the geometrical shape of a building. It is achieved in a hierarchical way by providing sub meshes or boundary representation (BREP) and transformations to the actual position of the parts. Parts also have a material description. When visualizing a BIM model, the parts should be drawn with different colors for different materials.

BIM models do not only model the outer hull. Load-bearing parts of a building like beams or pillars might be hidden under covering facade elements or ceilings. To allow the user to investigate here on a structural level, a visualization should allow filtering and hiding for a specific class of parts.

#### **5.2.2.2 Color Coding of Metrics**

Drawing the parts of a building model colored, according to their material is not always the goal. Instead one could indicate the properties of each part by drawing it in a different color. Important properties here are LOS velocity, the indication of what cluster they are part of, and the in Section 4.4.4 described quality metric that indicates how good the groups of PS points fit the segments of the model.

## 5.3 Examples

In this chapter, we discussed tools and design elements to create web-based platforms for the presentation of InSAR satellite-based monitoring. The aim of such decision support systems (DSSs) is to present only the important aspects of the data and allow for analysis in 3D. The combination with other data helps to interpret and contextualize the PSI results.

In the following, we are presenting exemplary implementations of such DSS. Here we have large area applications, such as a city-wide ground motion service and a project-related multi-modal platform. And the focus is on the presentation of PSI data on single buildings. The combination of complex building models and SAR-based deformation measurements requires tools that can visualize all the levels of information contained therein.

### 5.3.1 City Wide Ground Motion Service

In this example, we present an exemplary implementation for a city-wide ground motion service. A ground motion service is important because it provides data that can be used to improve security and urban planning. The data can also be used to assess the risk of damage to infrastructure or houses from natural or construction-induced deformations.

The here utilized dataset is a stack of 88 high-resolution SpotLight TerraSAR-X images over the city of Stuttgart, Germany. The images cover an area of  $4\text{ km} \times 5\text{ km}$ . The PSI analysis resulted in 3.3 million PS points in that area.

The point cloud is visualized in 3D. For better orientation, the points are drawn on top of a digital surface model (DSM) and an orthophoto. OSM data was used to draw single houses into the scene. This allows to distinguish the user which PS point is on which building. Due to an ongoing underground construction project, several parts of the city experience minor uplift or sinking. To visualize the dynamics of the deformation the user can scroll through time. The deformation for each point is color coded. This way of presentation makes it possible to make out temporal patterns, for example when certain tunneling processes started.

The here shown tool proved to be very informative. Before, the only way to communicate such findings would be either to share a large file with the point cloud to view in specialized software or to print out maps of certain areas.



(a)



(b)

Figure 5.1: (a) is an overview over a city-wide motion service. The PS points show the color-coded total line-of-sight deformation. The color corresponds to the bar on the left. The deformation on a specific day can be selected via a drop-down menu or the slider at the bottom. (b) shows a detailed closeup of some houses. The OSM buildings help to make out the points that lay on a house and enable an identification.



### 5.3.2 Project-Related Multi-modal Platform

This example shows a web platform that visualizes data from various sensors. Here ALS data and UAV-based photogrammetry are combined with PSI data to create a detailed picture of a river lock. The lock suffers from minor washouts and cavities and was chosen therefore as a study object. For the PSI evaluation, two multi-year stacks of high-resolution SpotLight TerraSAR-X images are available. The two image stacks observe the scene from two different directions. The combination of the sparse PSI data with the very dense LiDAR point cloud and an orthoimage, helps to understand and interpret the scene.

In Figure 5.2 the PS points from the ascending and descending orbit direction are superimposed with a digital terrain model. The color of each point indicates the orbit. The LOS direction is indicated by two arrows.

At the top, the web portal offers a short explanation of how to use the mouse to navigate through the data. On the right, different data sources can be enabled or hidden.

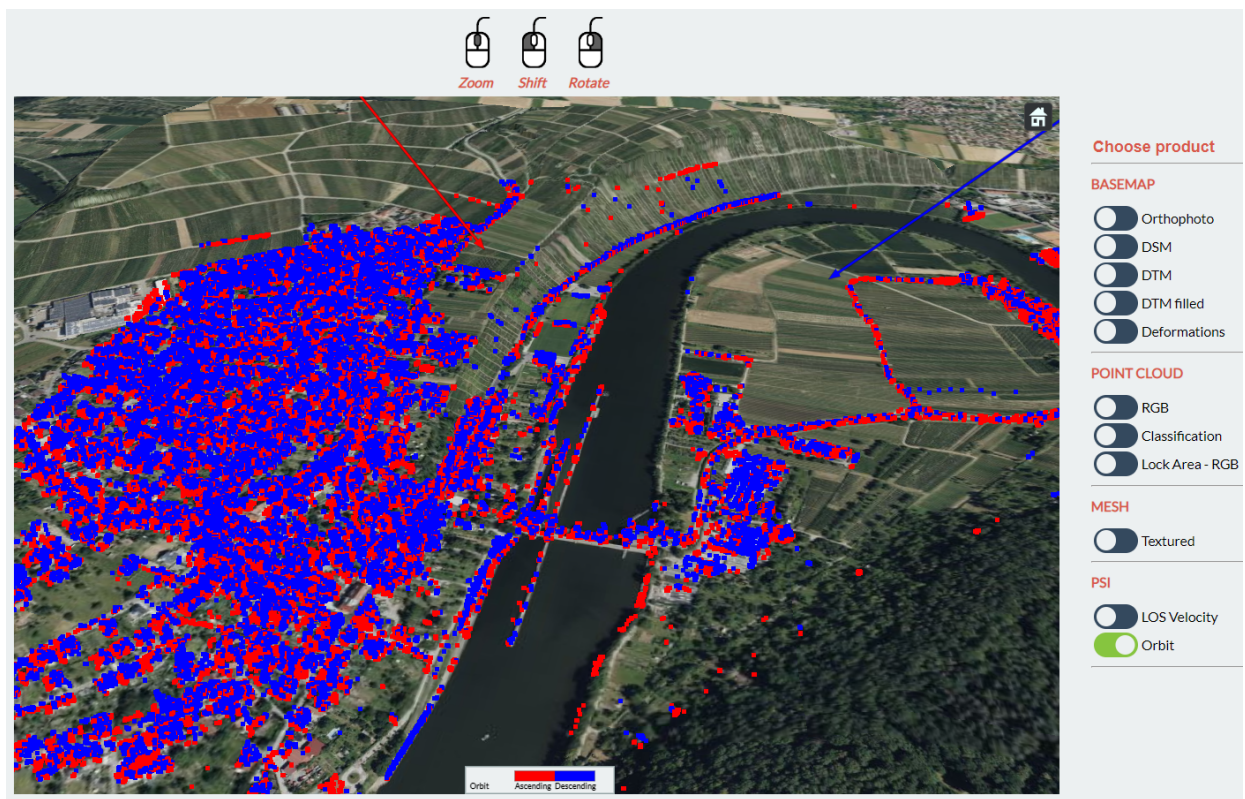


Figure 5.2: A web platform to present multi-modal data. The user can hide and show different data sources, like ALS or orthophotos to superimpose with the PSI data.

In Figure 5.3, the LOS velocity is color coded for each PS point. This helps to make out areas that undergo significant subsidence.

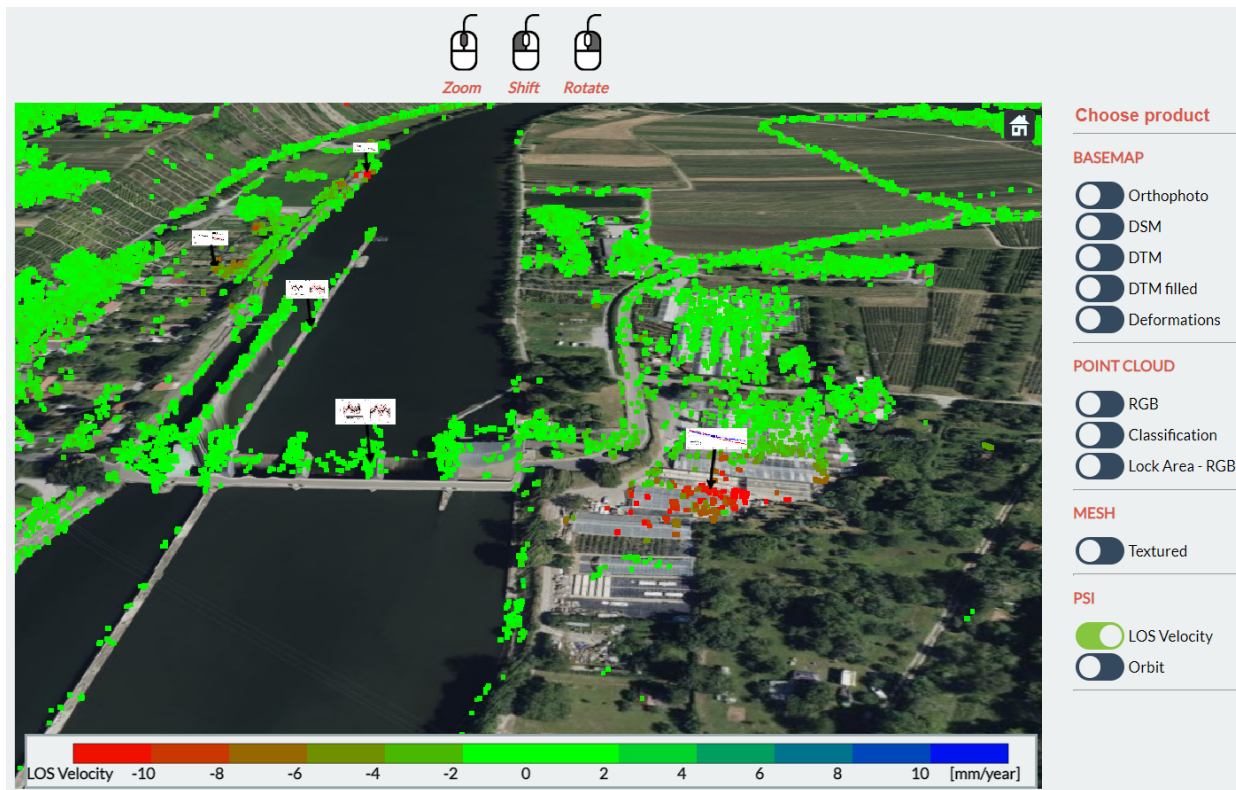
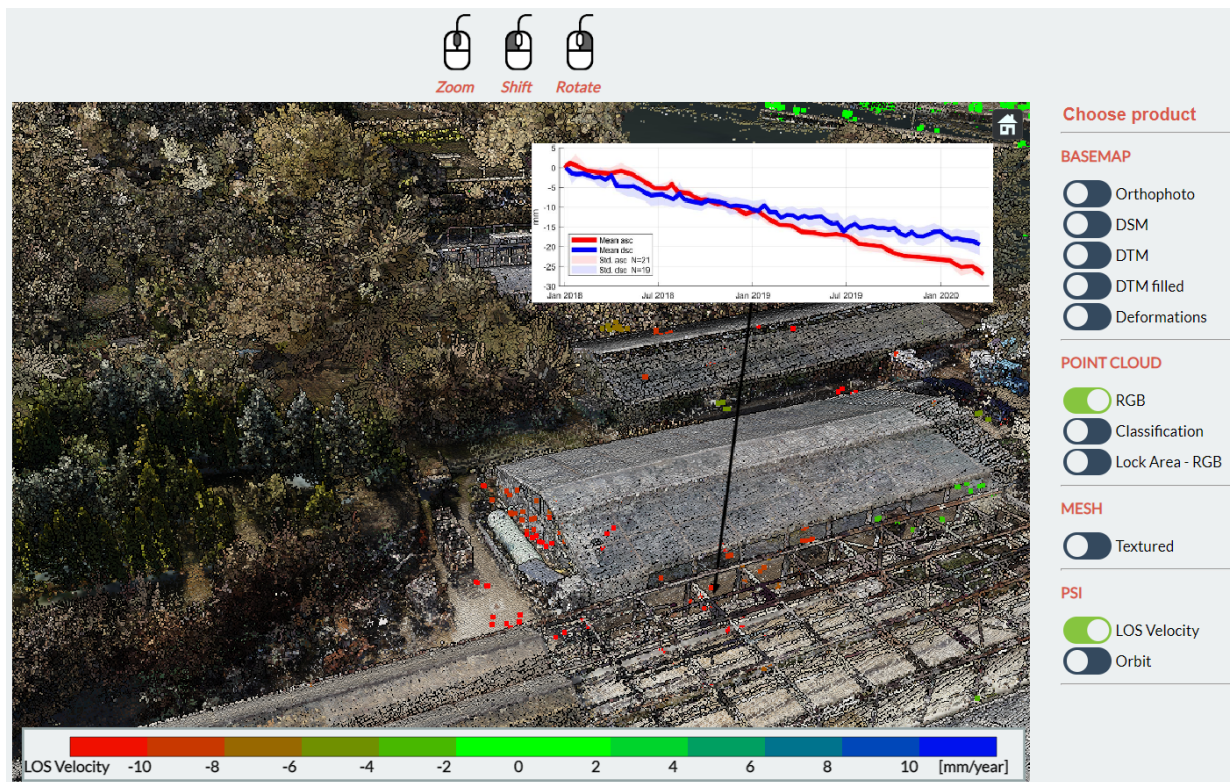


Figure 5.3: The line-of-sight (LOS) velocity of PS points is color coded. Red points indicate subsidence.

Figure 5.4 shows details from this scene. Here the ALS point cloud, respectively a mesh from UAV photogrammetry, helps with the interpretation of the data. Without this external data, the exact position of the PS points could not be determined. In order to draw the attention of the observer to certain movement patterns, the time series for some points have been superimposed in Figure 5.4a. The deformation process for both orbital directions is considered separately.





(a)



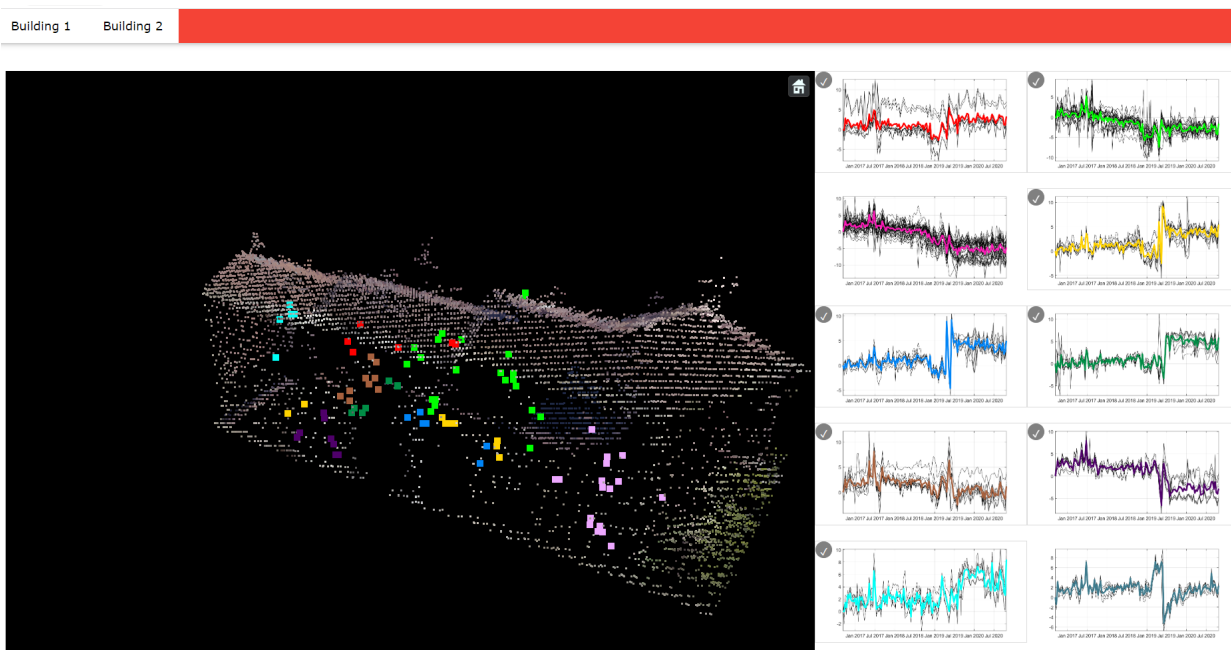
(b)

Figure 5.4: PS points super imposed with 3D geodata. (a) uses an ALS point cloud to visualize a cluttered area. The user's attention is guided, by depicting the deformation time series for certain interesting points. (b) shows the PS point cloud overlayed with a mesh from dense image matching. The details in the mesh make it easy to spot the scattering structures, like here for example the solar panels on the roof.

### 5.3.3 Visualizing PS Groups on Single Buildings

In chapter 4 we focused on PS points on single buildings. We presented an approach to group PS points into clusters that show a similar deformation behavior. The consideration of such groups instead of individual measurements offers the advantage that redundant observations of the underlying deformation processes can be made. Furthermore, the extension of such a group can be studied. The extent gives an indication of the static elements of a building.

However, it is not so easy to present such complex 3D data. The problem is that simple images only show the scene from one perspective, so the spatial structure is lost. Furthermore, it is not simple to distinguish dozens or hundreds of PS groups by color. The following exemplary implementations of web portals try to address this. If one has identified an interesting movement in the time series and one wants to know exactly where on the building this group of PS points is located, such a web portal can be straight forward be used to do this easily and without the need of special software.



*Figure 5.5:* A web portal to present resulting PS groups. An ALS point cloud, superimposed with the PS points. The clusters are color-coded and correspond with the extracted time series on the right-hand side. The user can move the mouse over a time series to highlight it in the 3D view, freely rotate and zoom and show/hide the ALS and the PS points.

In Section 4.4.3 an algorithm was presented that finds the optimal assignment for PS clusters to a structured mesh. Meshes, as a digital entity, can only be displayed in rendering software. If one wants to visualize the different structural elements of a building in this way, a web platform is a good alternative to local software. An example of such a platform is shown in Figure 5.6. The building can be visualized transparently and with or without PS points. For each cluster, the corresponding time series can be displayed. Figure 5.7 depicts a similar approach but does not show the time series to the user.



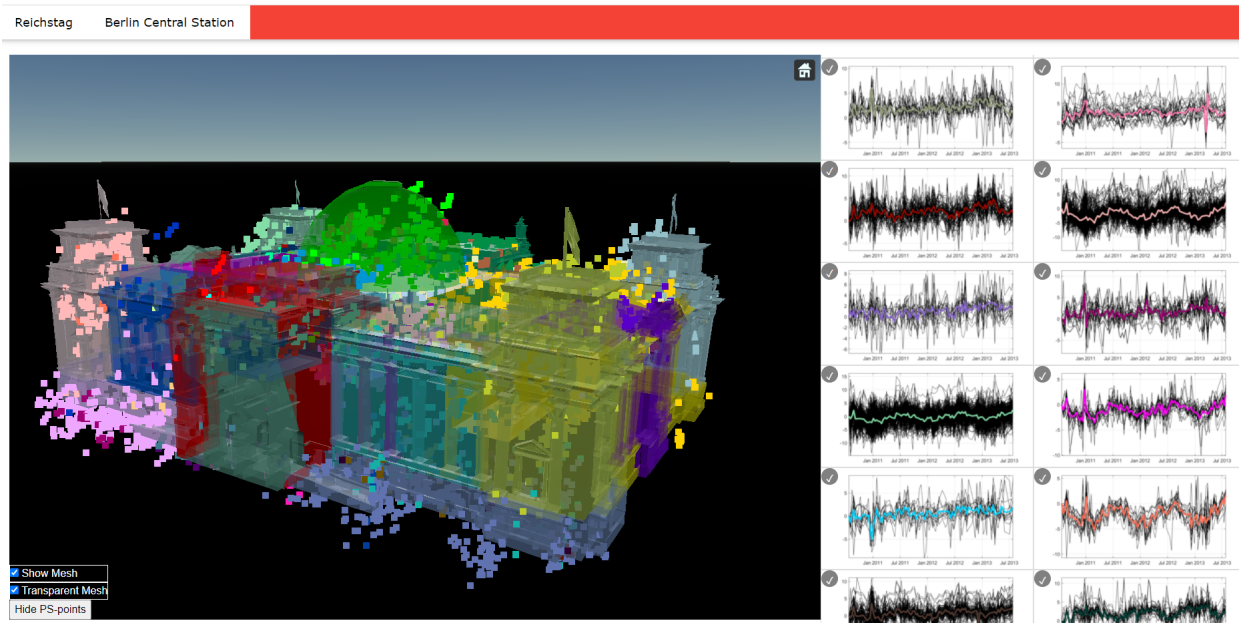


Figure 5.6: Clusters of PS points superimposed with structured mesh representations of a building. Left: Mesh superimposed with the PS points. The clusters are color-coded and correspond with the extracted time series on the right-hand side. The user can move the mouse over a time series to highlight it in the 3d view, freely rotate and zoom and show/hide the mesh and the points.

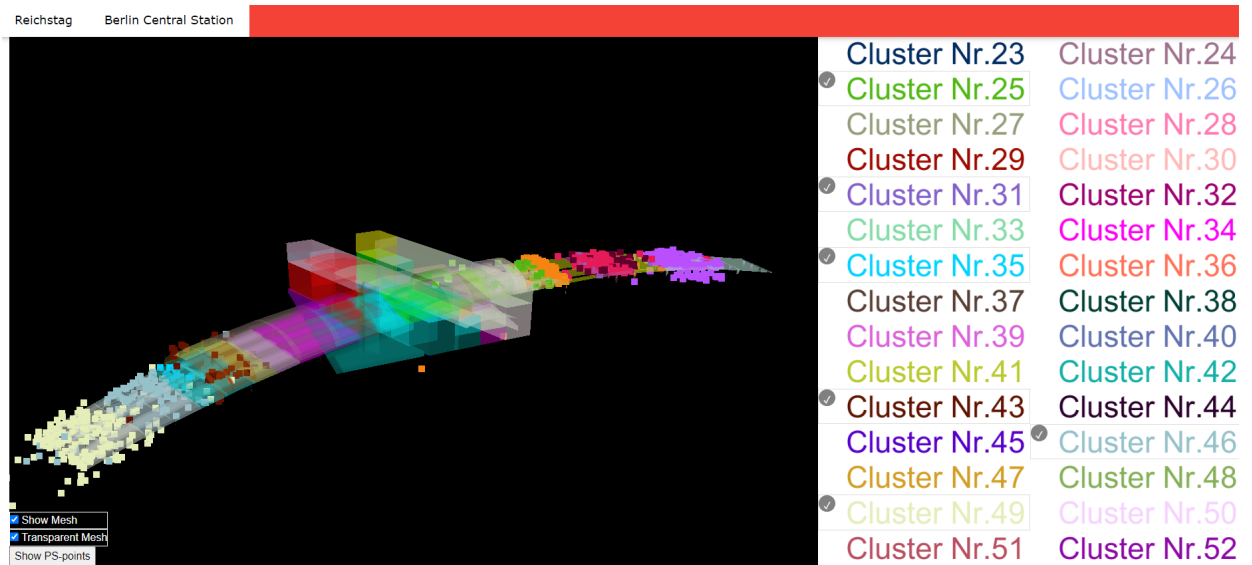
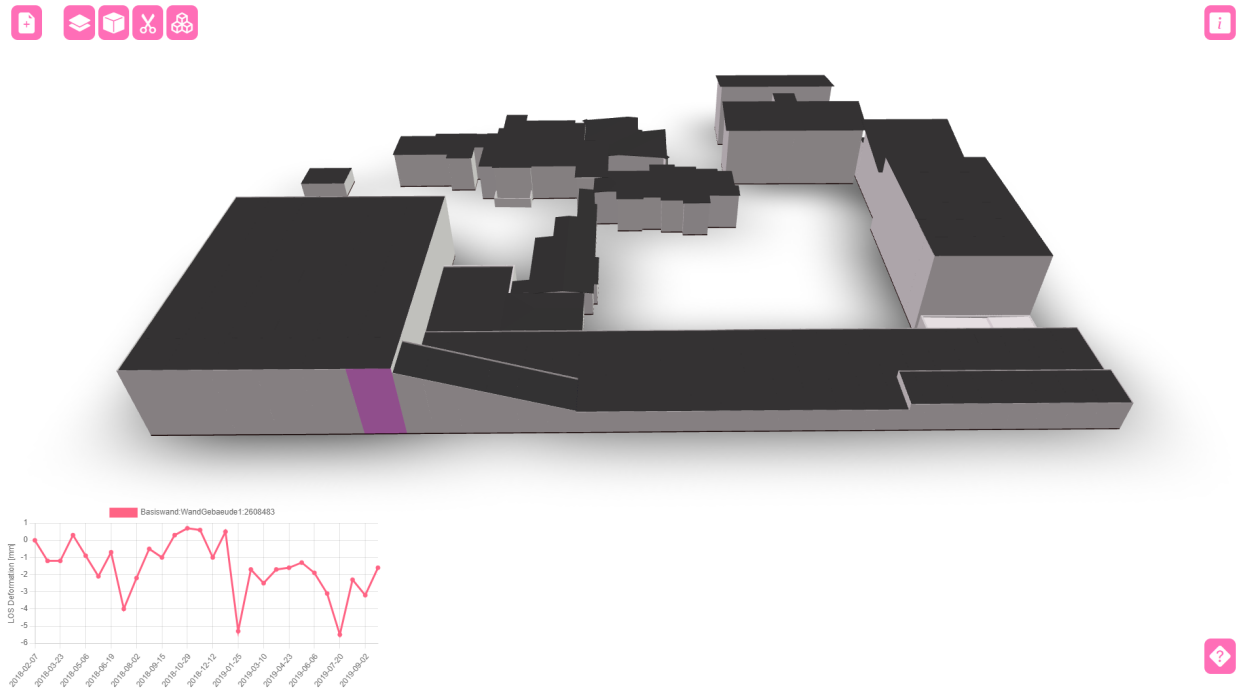


Figure 5.7: Clusters of PS points superimposed with structured mesh representations of a building. This long building consists of an elevated train track. The extension of each cluster gives an insight into the structure of the bridge. The user can zoom in and show and hide individual clusters.



### 5.3.4 Augmenting Building Information Models With PS-InSAR Data

The previously presented examples showed PS data and other representations of a building, like ALS point clouds or meshes. In Section 4.4.6 we discussed how to integrate the results from PSI into the IFC format that is commonly used in BIM. In Section 4.5.5 we showed some exemplary integration and proposed a property set for the PSI data. Here we present web-based tools, that allows any user, without the need for special software, to look at the results. The tool in Figure 5.8 directly displays the data from the IFC file. It allows showing the SAR-specific information for each element, like the LOS velocity or the associated time series for each cluster.



*Figure 5.8:* A web portal to visualize an IFC file with monitoring data from PSI. Single structural elements, like walls, beams, slabs, and parts of the roof can be selected. The associated data from the IFC file is displayed. Here the selected part of the wall is highlighted pink. The time series plot shows the movement of the PS group that is linked to this part.

The web portal allows also for more complex analysis and visualization. In Figure 5.9 the same IFC file is shown. The LOS velocity is color coded for each part. The user can visualize sections of the complete building. This allows for investigation into otherwise hidden parts, like the beams and columns and the roof.

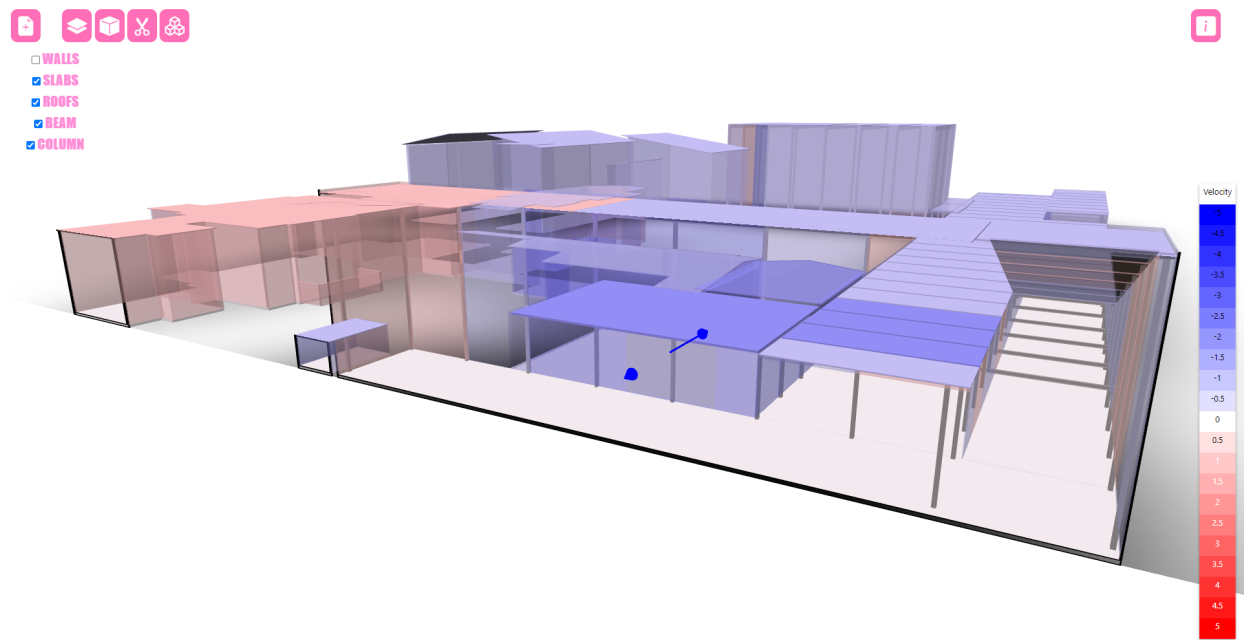


Figure 5.9: A web portal to visualize an IFC file with monitoring data from PSI. Single structural elements, like walls, beams, slabs, and parts of the roof are color coded with their LOS velocity. The tools allow section views and filter by element type to show otherwise hidden parts.

## Chapter 6

# Conclusion, Limitations and Outlook

In this thesis, methods to find and analyze patterns in Persistent Scatterer Interferometry (PSI) products were presented. In the following chapter, the key findings of the presented research and its potential applications in the industry along, with some open research questions are summarized. This is followed by a short discussion about the limitations of the here presented work and an outlook on the potential of it's further development.

Persistent Scatterer Interferometry (PSI) is a powerful method that allows to derive deformation time series from a stack of SAR images. The increasing availability of such satellite data makes a city wide per building monitoring and risk assignment possible. In contrast to this building sharp observation. We suggested to treat wide area monitoring differently from the monitoring of buildings and other complex structures. When dealing with PS points that show the deformation over a wide area its is common in literature to pick single points and analyze and discuss the movement of single PS points. We suggest to treat such a field of time series as an ensemble. Analysis methods from other data driven fields, such as meteorology are well suite for such investigations. We showed that a spectral analysis of the ensemble of time series can reveal patterns or modes that describe the movements of groups of points. The consideration of the entire field of points allows an insight in the spatial pattern of a deformation and shows the extend of a certain underlying deformation process such as an underground sinkhole or the annual temperature induced contractions and expansions of steal enforced structures. The analysis of the movements of single buildings and other complex structures requires other methods and approaches. Series of high resolution Synthetic Aperture Radar (SAR) images from missions like TerraSAR-X are available for the majority of cities world wide, especially for the ones that suffer from some kind of malicious subsidence. The PSI evaluation method leads to dense PS point clouds with often thousands of points per building. We discussed the question of how to assign the points automatically and city wide to each building using OpensStreetMap (OSM) building footprints. When considering all the PS points on a single building, we showed that groups of points can be found that have a correlated deformation behavior, the assumption here is that those points lay on the same rigid structure for example the same beam, slab or on the the same pillar. We could show the plausibility of such groups by comparing them to ground based measurements and 3D model of the building. For the further use of such satellite-based monitoring measurements it is important to combine them with other data, such as 3D building models. The presentation of this novel product is not trivial, especially because the target group often does not have the expertise with such complex 4D data. We presented an approach to link PS points to BIM models and discussed different ways to present the results in web based browser tools, that lowers the initial burden for decision makers, since no expert software has to be installed to view the big data sets.

The findings of this work conclude that high resolution SAR data enables a detailed monitoring of fine

structures and complex urban buildings. This has been shown by several authors in the past and is not in itself a new discovery. We see our contribution in the realization that the consideration of PSI results should not be limited to individual points. Rather, from the combined effect of how groups of points move, greater insight can be gained into the underlying deformation process and the potential impact on a structure. We found that methods, established in meteorology, data mining and machine learning, such as spectral analysis of time series, non-linear dimension reduction and clustering can be used to find such patterns. Furthermore, we have seen that the inclusion of multimodal sensor data, respectively the combination of PS points and 3D building models is helpful in the interpretation of the results and can enrich such models with monitoring data. The integration of this space-borne sensor data into a BIM model requires custom low-threshold entry and appropriate presentation and visualization solutions.

In this work, we could not answer all questions of how the structural analysis can be done. We suggest a workflow that assigns the movements derived from satellite data to structural parts of a building. The open question here would be on a risk assignment based on structural knowledge and the movements of adjoining parts of a building. To answer this question other experts from civil engineering and construction physics have to be regarded. We believe that the most important prerequisite for such a research project is a suitable test object, i.e., a building subject to deformation. The research building should be equipped with supplementary sensors and a detailed as-built model must be available. The good news are, that there is a good chance that archived SAR data is already existing, especially if the building is located in a known subsidence area.

Another limitation to this work, is that besides from the comparison with the ground based measurements (see Section 4.5.2.2) no quantitative metrics and quality assessment could be carried out. This is mainly due to the fact that it is difficult to make such a comparison here, since there is no ground truth for grouping the points or assigning them to the building components. Qualitative comparisons have been made, but it would be good if there was something like a benchmark that would allow the results to be evaluated quantitatively.

We are confident that the results of our work will open up opportunities for practical applications in the industry, but also new questions for further research. 3D city models are available for many cities and the future obligation to use BIM processes in the construction of many projects will intensify this trend. The integration into existing models would be conceivable that, analogous and complementary to the national ground motion services, platforms and applications are created that depict the ground motions in a city for each building. Here it is important that automatized processes and workflows are adapted. The pipeline, starting with the extraction of PS points, their assignment to each building, the clustering process and the final visualization and potential structural analysis has to be robust and must work without major hyperparameter tuning. It should also be transferable to other areas. Another requirement for such a workflow is that, once new images from the satellite are available, the process loop should start all over and update the data set consistently.

# Appendix

# A Principles

Name	Band	Start - End	Max. along-track	Max. cross-track	Max. Bandwidth	Repeat Period	Mission Goal
<b>SEASAT</b> (Born et al., 1979)	L-Band	1978-1978	30 m	26 m	10MHz	17 days	First civilian SAR satellite, operation for only three months
<b>ERS-1</b> (Rignot and Van Zyl, 1993)	C-Band	1991 - 2000	30 m	26 m	16MHz	35 days	Observation, environmental monitoring, change detection, polar ice, land ecology, geology, forestry, wave phenomena, bathymetry, atmospheric physics, meteorology
<b>JERS</b> (Yoneyama et al., 1990)	L-Band	1992 - 1998	18 m	18 m	15 MHz	44 days	Survey of geological phenomena, land usage, observation of coastal regions, geologic maps, environment, disaster monitoring, change detection.
<b>ERS-2</b> (Francis et al., 1995)	C-Band	1995 - 2011	6 m	26 m	16MHz	35 Days	Observation, environmental monitoring, change detection, polar ice, land ecology, geology, forestry, wave phenomena, bathymetry, atmospheric physics, meteorology
<b>Radsat-1</b> (Jezek et al., 2003)	C-Band	1995 - 2012	10 m	10 m	30 MHz	24 Days	Agriculture and land cover monitoring, Forestry, Geology, Hydrology, Coastal zones and oceans, Cartography and land use.
<b>Envisat</b> (Llovet and Bruzzi, 1999)	C-Band	2002 - 2012	28 m	28 m	16 Mhz	35 Days	Multi Instrument Platform, Observation, Intelligence, Interferometry
<b>ALOS</b> (Rosenqvist et al., 2007)	L-Band	2006 - 2011	10 m	10 m	28 MHz	46 Days	Observation, Intelligence, Interferometry
<b>Cosmo-SkyMed</b> (Covello et al., 2010)	X-Band	2007/2007/2008/2010 - $\geq 2022$	< 1 m	< 1 m	300-400 Mhz	16 Days 4 Day (Constellation)	Observation, Intelligence, Interferometry
<b>TerraSAR-X/TanDEM-X</b> (Krieger et al., 2007b) (Werninghaus and Buckreus, 2009)	X-Band	2007/2010 - $\geq 2022$	< 1 m	< 1 m	300 MHz	11 Days	DEM Generation, stereoetry, Intelligence, Deformation Monitoring
<b>Radsat-2</b> (Livingstone et al., 2006)	C-Band	2007 - $\geq 2022$	1 m	3 m	100 MHz	24 Days	Observation, Intelligence, Interferometry
<b>KOMPSAT-5</b> (Lee, 2010)	X-Band	2013 - $\geq 2022$	1 m	1 m	300 MHz	28 Days	Korea Multi-Purpose Satellite, Observation, Intelligence, Interferometry
<b>Sentinel-1a/b</b> Torres et al. (2012)	C-Band	2014/2016 - $\geq 2022/2021$	5 m	5 m	280 MHz	12 Days 6 Days (Constellation)	Continuous Global Observation, Long Term Archive, Interferometry
<b>ALOS-2</b> (Rosenqvist et al., 2014)	L-Band	2014 - $\geq 2022$	1 m	3 m	84 MHz	46 Days	Observation, Intelligence, Interferometry
<b>SOACOM-1a,b</b> (Giudici et al., 2017)	L-Band	2018/2020 - $\geq 2022$	10 m	10 m	45 MHz	16 Days 8 Days (Constellation)	Observation, Intelligence, Interferometry
<b>Radsat Constellation</b> (Thompson *, 2015)	C-Band	2019 - $\geq 2022$	2 m	2 m	100MHz	12 Days 4 Days (Constellation)	Observation, Intelligence, Interferometry
<b>NISAR</b> (Xaypraseuth et al., 2015)	L/S-Band	$\geq 2023 - \geq 2023$	7 m	3 m	80 MHz	12 Days	Observation, Biomass monitoring, Interferometry
<b>Capella</b> (Castelletti et al., 2020)	X-Band	2018 to 2021 - $\geq 2022$	0.5 m	0.5 m	500 MHz	<1 Day in Constellation	New Space company, 36 Microsatellites, Observation, Intelligence, Interferometry
<b>ICEYE</b> (Ignatenko et al., 2020)	X-Band	2018 - ???	1 m	0.4 m	300 MHz	17 Days 1 Day (Constellation)	Private micro-satellite constellation, Observation, Intelligence, Interferometry
<b>Sentinel-1c/d</b> Torres et al. (2021)	C-Band	2023 - ???	0.6 m	0.8 m	280 MHz	12 Days 6 Day (Constellation)	Replace Sentinel-1a/b

Table A1: SAR Missions Overview

Name	Price	Advantage	Disadvantage
SARscape (L3Harris) (SARMAP, 2014)	Several 10000€ Year	Full pipeline	Black box
StaMPS (Hooper et al., 2007)	Free (requires Matlab)	Open Source	Can not generate interferograms
ROI PAC (JPL/CalTech) (Rosen et al., 2004)	free	Open Source	Not State of the Art poorly documented
PSIG (CTTC) (Devan���� et al., 2014)	Not Commercially Available	State of the Art	Not Commercially Available
GAMMA (Gamma Remote Sensing) (Werner et al., 2000)	Several 10000€ Year	Full pipeline Source code available	
DORIS (TUDelft) Kampes and Usai (1999)	Free	open source	
PSI-GENESIS (DLR) Adam et al. (2008)	Not Commercially Available	State of the art	Not Commercially Available
SARPROZ Perissin et al. (2011)	Price on request	Different multi-temporal analysis like Permanent Scatterers (PS), Quasi-PS (QPS)	Experimental
SqueeSAR (TRE Altamira) Ferretti et al. (2011)	Processing as a service	State of the art	Not Commercially Available

Table A2: DInSAR Analysis Software Overview





# Bibliography

- Adam, N., Eineder, M., Yague-Martinez, N., and Bamler, R. (2008). High resolution interferometric stacking with TerraSAR-x. In *IGARSS 2008 - 2008 IEEE International Geoscience and Remote Sensing Symposium*. IEEE. 103
- Allaoui, M., Kherfi, M. L., and Cheriet, A. (2020). Considerably improving clustering algorithms using umap dimensionality reduction technique: A comparative study. In El Moataz, A., Mammass, D., Mansouri, A., and Nouboud, F., editors, *Image and Signal Processing*, pages 317–325, Cham. Springer International Publishing. 61
- Alshawaf, F., Hinz, S., Mayer, M., and Meyer, F. J. (2015). Constructing accurate maps of atmospheric water vapor by combining interferometric synthetic aperture radar and gnss observations. *Journal of Geophysical Research: Atmospheres*, 120(4):1391–1403. 33
- Ankerst, M., Breunig, M. M., Kriegel, H.-P., and Sander, J. (1999). OPTICS. *ACM SIGMOD Record*, 28(2):49–60. 62
- Aorpimai, M. and Palmer, P. (2007). Repeat-groundtrack orbit acquisition and maintenance for earth-observation satellites. *Journal of guidance, control, and dynamics*, 30(3):654–659. 28
- Arangio, S., Calò, F., Mauro, M. D., Bonano, M., Marsella, M., and Manunta, M. (2013). An application of the SBAS-DInSAR technique for the assessment of structural damage in the city of rome. *Structure and Infrastructure Engineering*, 10(11):1469–1483. 35
- Bamler, R. and Hartl, P. (1998). Synthetic aperture radar interferometry. *Inverse problems*, 14(4):R1. 29
- Bayramov, E., Buchroithner, M., and Kada, M. (2020). Quantitative assessment of ground deformations for the risk management of petroleum and gas pipelines using radar interferometry. *Geomatics, Natural Hazards and Risk*, 11(1):2540–2568. 37
- Berardino, P., Fornaro, G., Lanari, R., and Sansosti, E. (2002). A new algorithm for surface deformation monitoring based on small baseline differential SAR interferograms. *IEEE Transactions on Geoscience and Remote Sensing*, 40(11):2375–2383. 32, 34
- Bianchini, S., Pratesi, F., Nolesini, T., and Casagli, N. (2015). Building deformation assessment by means of persistent scatterer interferometry analysis on a landslide-affected area: The volterra (italy) case study. *Remote Sensing*, 7(4):4678–4701. 38, 57
- Bjornsson, H. and Venegas, S. A. (1997). *A Manual for EOF and SVD Analyses of Climatic Data*. McGill University. 45
- Born, G., Dunne, J., and Lame, D. (1979). Seasat mission overview. *Science*, 204(4400):1405–1406. 35, 102
- Boulila, W., Farah, I. R., and Hussain, A. (2017). A novel decision support system for the interpretation of remote sensing big data. *Earth Science Informatics*, 11(1):31–45. 85
- Brockmann, H., Sörgel, U., Havel, P., Röpel, L., Cramer, M., and Schneider, P. (2020). Multisensorales ingenieur-geodätisches bauwerks- und -umfeldmonitoring. In *Dresdner Wasserbauliche Mitteilungen* 63. 12

- Brovelli, M. A., Minghini, M., Molinari, M. E., and Zamboni, G. (2016). POSITIONAL ACCURACY ASSESSMENT OF THE OPENSTREETMAP BUILDINGS LAYER THROUGH AUTOMATIC HOMOLOGOUS PAIRS DETECTION: THE METHOD AND a CASE STUDY. *ISPRS - International Archives of the Photogrammetry, Remote Sensing and Spatial Information Sciences*, XLI-B2:615–620. 58
- Castelletti, D., Farquharson, G., Stringham, C., and Eddy, D. (2020). Operational readiness of the capella space sar system. In *IGARSS 2020-2020 IEEE International Geoscience and Remote Sensing Symposium*, pages 3571–3573. IEEE. 102
- Catalão, J., Nico, G., Hanssen, R., and Catita, C. (2011). Merging gps and atmospherically corrected insar data to map 3-d terrain displacement velocity. *IEEE Transactions on Geoscience and Remote Sensing*, 49(6):2354–2360. 33
- Chang, L., Dollevoet, R. P. B. J., and Hanssen, R. F. (2017). Nationwide railway monitoring using satellite SAR interferometry. *IEEE Journal of Selected Topics in Applied Earth Observations and Remote Sensing*, 10(2):596–604. 37
- Chang, L. and Hanssen, R. (2014). Detection of cavity migration and sinkhole risk using radar interferometric time series. *Remote sensing of environment*, 147:56–64. 36, 58
- Colesanti, C., Ferretti, A., Novali, F., Prati, C., and Rocca, F. (2003). Sar monitoring of progressive and seasonal ground deformation using the permanent scatterers technique. *IEEE Transactions on Geoscience and Remote Sensing*, 41(7):1685–1701. 34
- Colesanti, C. and Wasowski, J. (2006). Investigating landslides with space-borne synthetic aperture radar (SAR) interferometry. *Engineering Geology*, 88(3-4):173–199. 36
- Costantini, M., Falco, S., Malvarosa, F., and Minati, F. (2008). A new method for identification and analysis of persistent scatterers in series of SAR images. In *IGARSS 2008 - 2008 IEEE International Geoscience and Remote Sensing Symposium*. IEEE. 33
- Costantini, M., Falco, S., Malvarosa, F., Minati, F., Trillo, F., and Vecchioli, F. (2014). Persistent scatterer pair interferometry: Approach and application to COSMO-SkyMed SAR data. *IEEE Journal of Selected Topics in Applied Earth Observations and Remote Sensing*, 7(7):2869–2879. 33
- Costantini, M., Falco, S., Malvarosa, F., Minati, F., Trillo, F., and Vecchioli, F. (2014). Persistent scatterer pair interferometry: Approach and application to cosmo-skymed sar data. *IEEE Journal of Selected Topics in Applied Earth Observations and Remote Sensing*, 7(7):2869–2879. 57
- Costantini, M., Farina, A., and Zirilli, F. (1999). A fast phase unwrapping algorithm for SAR interferometry. *IEEE Transactions on Geoscience and Remote Sensing*, 37(1):452–460. 32
- Costantini, M., Minati, F., Trillo, F., Ferretti, A., Novali, F., Passera, E., Dehls, J., Larsen, Y., Marinkovic, P., Eineder, M., Brcic, R., Siegmund, R., Kotzerke, P., Probeck, M., Kenyeres, A., Proietti, S., Solari, L., and Andersen, H. S. (2021). European ground motion service (egms). In *2021 IEEE International Geoscience and Remote Sensing Symposium IGARSS*, pages 3293–3296. 39
- Costantini, M., Zhu, M., Huang, S., Bai, S., Cui, J., Minati, F., Vecchioli, F., Jin, D., and Hu, Q. (2018). Automatic detection of building and infrastructure instabilities by spatial and temporal analysis of insar measurements. *IGARSS 2018 - 2018 IEEE International Geoscience and Remote Sensing Symposium*, pages 2224–2227. 38, 57
- Covello, F., Battazza, F., Coletta, A., Lopinto, E., Fiorentino, C., Pietranera, L., Valentini, G., and Zoffoli, S. (2010). Cosmo-skymed an existing opportunity for observing the earth. *Journal of Geodynamics*, 49(3-4):171–180. 102
- Cozzi, P. and Ring, K. (2011). *3D engine design for virtual globes*. AK Peters/CRC Press. 86
- Crosetto, M., Crippa, B., and Biescas, E. (2005). Early detection and in-depth analysis of deformation phenomena by radar interferometry. *Engineering Geology*, 79(1-2):81–91. 33

- Crosetto, M., Gili, J. A., Monserrat, O., Cuevas-González, M., Corominas, J., and Serral, D. (2013). Interferometric SAR monitoring of the vallyebre landslide (spain) using corner reflectors. *Natural Hazards and Earth System Sciences*, 13(4):923–933. 36
- Crosetto, M., Monserrat, O., Cuevas-González, M., Devanthery, N., and Crippa, B. (2016). Persistent scatterer interferometry: A review. *ISPRS Journal of Photogrammetry and Remote Sensing*, 115:78–89. 30, 34, 35
- Crosetto, M., Monserrat, O., Cuevas-González, M., Devanthery, N., Luzi, G., and Crippa, B. (2015). Measuring thermal expansion using X-band Persistent Scatterer Interferometry. *ISPRS Journal of Photogrammetry and Remote Sensing*, 100:84–91. 38
- Crosetto, M., Solari, L., Balasis-Levinsen, J., Bateson, L., Casagli, N., Frei, M., Oyen, A., Moldestad, D. A., and Mróz, M. (2021). DEFORMATION MONITORING AT EUROPEAN SCALE: THE COPERNICUS GROUND MOTION SERVICE. *The International Archives of the Photogrammetry, Remote Sensing and Spatial Information Sciences*, XLIII-B3-2021:141–146. 39
- Crosetto, M., Solari, L., Mróz, M., Balasis-Levinsen, J., Casagli, N., Frei, M., Oyen, A., Moldestad, D. A., Bateson, L., Guerrieri, L., Comerci, V., and Andersen, H. S. (2020). The evolution of wide-area DInSAR: From regional and national services to the european ground motion service. *Remote Sensing*, 12(12):2043. 39
- Cuevas-González, M., Devanthery, N., Crosetto, M., Monserrat, O., and Crippa, B. (2015). The PSIG procedure to persistent scatterer interferometry (PSI) using x-band and c-band sentinel-1 data. In Notarnicola, C., Paloscia, S., and Pierdicca, N., editors, *SPIE Proceedings*. SPIE. 63
- Delgado, J. M. D., Butler, L. J., Gibbons, N., Brilakis, I., Elshafie, M. Z. E. B., and Middleton, C. (2017). Management of structural monitoring data of bridges using BIM. *Proceedings of the Institution of Civil Engineers - Bridge Engineering*, 170(3):204–218. 65, 68
- Desogus, G., Quaquero, E., Rubiu, G., Gatto, G., and Perra, C. (2021). BIM and IoT sensors integration: A framework for consumption and indoor conditions data monitoring of existing buildings. *Sustainability*, 13(8):4496. 65, 68
- Devanthery, N., Crosetto, M., Monserrat, O., Cuevas-González, M., and Crippa, B. (2014). An approach to persistent scatterer interferometry. *Remote Sensing*, 6(7):6662–6679. 32, 103
- Ester, M., Kriegel, H.-P., Sander, J., and Xu, X. (1996). A density-based algorithm for discovering clusters in large spatial databases with noise. In *Proceedings of the Second International Conference on Knowledge Discovery and Data Mining*, KDD’96, pages 226–231. AAAI Press. 62
- Fan, H., Zipf, A., Fu, Q., and Neis, P. (2014). Quality assessment for building footprints data on OpenStreetMap. *International Journal of Geographical Information Science*, 28(4):700–719. 58
- Farina, P., Colombo, D., Fumagalli, A., Marks, F., and Moretti, S. (2006). Permanent scatterers for landslide investigations: outcomes from the ESA-SLAM project. *Engineering Geology*, 88(3-4):200–217. 36
- Farr, T. G. and Kobrick, M. (2000). Shuttle radar topography mission produces a wealth of data. *Eos, Transactions American Geophysical Union*, 81(48):583–585. 28
- Farr, T. G., Rosen, P. A., Caro, E., Crippen, R., Duren, R., Hensley, S., Kobrick, M., Paller, M., Rodriguez, E., Roth, L., et al. (2007). The shuttle radar topography mission. *Reviews of geophysics*, 45(2). 28
- Ferretti, A., Fumagalli, A., Novati, F., Prati, C., Rocca, F., and Rucci, A. (2011). A new algorithm for processing interferometric data-stacks: SqueeSAR. *IEEE Transactions on Geoscience and Remote Sensing*, 49(9):3460–3470. 33, 103
- Ferretti, A., Prati, C., and Rocca, F. (2000). Nonlinear subsidence rate estimation using permanent scatterers in differential sar interferometry. *Geoscience and Remote Sensing, IEEE Transactions on*, 38:2202 – 2212. 31, 33, 36
- Ferretti, A., Prati, C., and Rocca, F. (2001). Permanent scatterers in SAR interferometry. *IEEE Transactions on Geoscience and Remote Sensing*, 39(1):8–20. 31, 32, 33, 36

- Fornaro, G., D'Agostino, N., Giuliani, R., Noviello, C., Reale, D., and Verde, S. (2014). Assimilation of gps-derived atmospheric propagation delay in dinsar data processing. *IEEE journal of selected topics in applied Earth observations and remote sensing*, 8(2):784–799. 33
- Francis, C., Graf, G., Edwards, P., McCraig, M., McCarthy, C., Lefebvre, A., Pieper, B., Pouvreau, P.-Y., Wall, R., and Weschler, F. (1995). The ers-2 spacecraft and its payload. *Esa Bulletin*, 83:13–31. 102
- Fu, X., Wu, M., and Tang, Y. (2012). Design and maintenance of low-earth repeat-ground-track successive-coverage orbits. *Journal of Guidance, Control, and Dynamics*, 35(2):686–691. 25, 28
- Gabriel, A. K., Goldstein, R. M., and Zebker, H. A. (1989). Mapping small elevation changes over large areas: Differential radar interferometry. *Journal of Geophysical Research: Solid Earth*, 94(B7):9183–9191. 30, 36
- Gernhardt, S., Adam, N., Eineder, M., and Bamler, R. (2010). Potential of very high resolution sar for persistent scatterer interferometry in urban areas. *Annals of GIS*, 16:103–111. 34, 38
- Gernhardt, S. and Bamler, R. (2012). Deformation monitoring of single buildings using meter-resolution SAR data in PSI. *ISPRS Journal of Photogrammetry and Remote Sensing*, 73:68–79. 38
- Gernhardt, S. and Bamler, R. (2015). Structural deformation and non-seasonal motion of single buildings in urban areas revealed by PSI. In *2015 Joint Urban Remote Sensing Event (JURSE)*. IEEE. 57
- Giudici, D., Monti Guarnieri, A., and Cuesta Gonzalez, J. P. (2017). Pre-flight saocom-1a sar performance assessment by outdoor campaign. *Remote Sensing*, 9(7). 102
- Goel, K. and Adam, N. (2013). A distributed scatterer interferometry approach for precision monitoring of known surface deformation phenomena. *IEEE Transactions on Geoscience and Remote Sensing*, 52(9):5454–5468. 33
- Goel, K. and Adam, N. (2014). A distributed scatterer interferometry approach for precision monitoring of known surface deformation phenomena. *IEEE Transactions on Geoscience and Remote Sensing*, 52(9):5454–5468. 37
- Goodchild, M. F. (2007). Citizens as sensors: the world of volunteered geography. *GeoJournal*, 69(4):211–221. 58
- Grebby, S., Sowter, A., Gluyas, J., Toll, D., Gee, D., Athab, A., and Girindran, R. (2021). Advanced analysis of satellite data reveals ground deformation precursors to the brumadinho tailings dam collapse. *Communications Earth Environment*, 2(1). 37
- Gromek, D., Stasiak, K., Samczynski, P., and Radecki, K. (2021). Experimental results of a k-band sar system for automotive applications. In *EUSAR 2021; 13th European Conference on Synthetic Aperture Radar*, pages 1–5. 17
- Guo, R. and Zhu, X. X. (2014). High-rise building feature extraction using high resolution spotlight tandem-x data. In *EUSAR 2014; 10th European Conference on Synthetic Aperture Radar*, pages 1–4. 38
- Haala, N., Kölle, M., Cramer, M., Laupheimer, D., and Zimmermann, F. (2022). Hybrid georeferencing of images and LiDAR data for UAV-based point cloud collection at millimetre accuracy. *ISPRS Open Journal of Photogrammetry and Remote Sensing*, 4:100014. 47
- Hanssen, R. F. (2001). *Radar Interferometry*. Springer Netherlands. 36
- Heidler, K., Mou, L., Baumhoer, C., Dietz, A., and Zhu, X. X. (2022). Hed-unet: Combined segmentation and edge detection for monitoring the antarctic coastline. *IEEE Transactions on Geoscience and Remote Sensing*, 60:1–14. 72
- Herrera, G., Notti, D., García-Davalillo, J., Mora, O., Cooksley, G., Sánchez, M., Arnaud, A., and Crosetto, M. (2010). Analysis with c- and x-band satellite sar data of the portalet landslide area. *Landslides*, 8(2):195–206. 36
- Hooper, A. (2008). A multi-temporal InSAR method incorporating both persistent scatterer and small baseline approaches. *Geophysical Research Letters*, 35(16). 33
- Hooper, A., Segall, P., and Zebker, H. (2007). Persistent scatterer interferometric synthetic aperture radar for crustal deformation analysis, with application to volcán alcedo, galápagos. *Journal of Geophysical Research*, 112(B7). 103

- Hooper, A., Zebker, H., Segall, P., and Kampes, B. (2004). A new method for measuring deformation on volcanoes and other natural terrains using InSAR persistent scatterers. *Geophysical Research Letters*, 31(23). 33
- Hooper, A. and Zebker, H. A. (2007). Phase unwrapping in three dimensions with application to InSAR time series. *Journal of the Optical Society of America A*, 24(9):2737. 33
- IEEE (1984). IEEE standard letter designations for radar-frequency bands. 17
- Ignatenko, V., Laurila, P., Radius, A., Lamentowski, L., Antropov, O., and Muff, D. (2020). Iceye microsatellite sar constellation status update: Evaluation of first commercial imaging modes. In *IGARSS 2020-2020 IEEE International Geoscience and Remote Sensing Symposium*, pages 3581–3584. IEEE. 102
- Isikdag, U. (2015). The future of building information modelling: BIM 2.0. In *Enhanced Building Information Models*, pages 13–24. Springer International Publishing. 65
- Jezek, K., Farness, K., Carande, R., Wu, X., and Labelle-Hamer, N. (2003). Radarsat 1 synthetic aperture radar observations of antarctica: Modified antarctic mapping mission, 2000. *Radio Science*, 38(4):32–1. 102
- Johnsen, H., Lauknes, L., and Guneriusen, T. (1995). Geocoding of fast-delivery ERS-1 SAR image mode product using DEM data. *International Journal of Remote Sensing*, 16(11):1957–1968. 27, 32
- Jung, J., Kim, D.-j., and Park, S.-E. (2013). Correction of atmospheric phase screen in time series insar using wrf model for monitoring volcanic activities. *IEEE transactions on geoscience and remote sensing*, 52(5):2678–2689. 33
- Kalia, A., Frei, M., and Thomas, L. (2021). Bodenbewegungsdienst deutschland (bbd): Konzept, umsetzung und service-plattform. *zfv – Zeitschrift für Geodäsie, Geoinformation und Landmanagement*, pages 273–279. 39
- Kalia, A. C. (2017). User driven products in the context of the ground motion service germany. In *2017 IEEE International Geoscience and Remote Sensing Symposium (IGARSS)*. IEEE. 39
- Kampes, B. and Hanssen, R. (2004). Ambiguity resolution for permanent scatterer interferometry. *IEEE Transactions on Geoscience and Remote Sensing*, 42(11):2446–2453. 33
- Kampes, B. M. (2006). *Radar Interferometry*. Springer-Verlag GmbH. 33
- Kampes, B. M. and Usai, S. (1999). Doris: The delft object-oriented radar interferometric software. 103
- Kauther, R. and Wolf, C. (2018). Detection of cavities in karst subsoil affecting civil engineering structures by means of geophysical measurements. In *TC220 Conferences in Field Monitoring in Geomechanics - Field Measurements in Geomechanics*. 47
- Khudhair, A., Li, H., Ren, G., and Liu, S. (2021). Towards future bim technology innovations: A bibliometric analysis of the literature. *Applied Sciences*, 11:1232. 65
- Kobrick, M. (2006). On the toes of giants-how srtm was born. *Photogrammetric Engineering and Remote Sensing*, 72(3):206–210. 28
- Krieger, G., Hajnsek, I., Papathanassiou, K. P., Younis, M., and Moreira, A. (2010). Interferometric synthetic aperture radar (SAR) missions employing formation flying. *Proceedings of the IEEE*, 98(5):816–843. 28
- Krieger, G., Moreira, A., Fiedler, H., Hajnsek, I., Werner, M., Younis, M., and Zink, M. (2007a). Tandem-x: A satellite formation for high-resolution sar interferometry. *IEEE Transactions on Geoscience and Remote Sensing*, 45(11):3317–3341. 28
- Krieger, G., Moreira, A., Fiedler, H., Hajnsek, I., Werner, M., Younis, M., and Zink, M. (2007b). Tandem-x: A satellite formation for high-resolution sar interferometry. *IEEE Transactions on Geoscience and Remote Sensing*, 45(11):3317–3341. 102
- Kuhn, H. W. (1955). The hungarian method for the assignment problem. *Naval Research Logistics Quarterly*, 2(1-2):83–97. 66, 67

- Laakso, M., Kiviniemi, A., et al. (2012). The ifc standard: A review of history, development, and standardization, information technology. *ITcon*, 17(9):134–161. 68
- Lanari, R., Casu, F., Manzo, M., and Lundgren, P. (2007). Application of the SBAS-DInSAR technique to fault creep: A case study of the hayward fault, california. *Remote Sensing of Environment*, 109(1):20–28. 35
- Lee, S.-R. (2010). Overview of kompsat-5 program, mission, and system. In *2010 IEEE international geoscience and remote sensing symposium*, pages 797–800. IEEE. 102
- Lege, T., Kalia, A., and Frei, M. (2019). Aspekte des bodenbewegungsdienstes deutschland. 39
- Leighton, J. M. (2010). *GPS and PSI integration for monitoring urban land motion*. PhD thesis, University of Nottingham. 33
- Liu, D., Sowter, A., and Niemeier, W. (2014). Process-related deformation monitoring by psi using high resolution space-based sar data: a case study in düsseldorf, germany. Technical report, semanticscholar. 37
- Liu, S. (2012). Satellite radar interferometry: estimation of atmospheric delay. 33
- Livingstone, C., Sikaneta, I., Gierull, C., Chiu, S., and Beaulne, P. (2006). Radarsat-2 system and mode description. Technical report, DEFENCE RESEARCH AND DEVELOPMENT CANADA OTTAWA (ONTARIO). 102
- Louet, J. and Bruzzi, S. (1999). Envisat mission and system. In *IEEE 1999 International Geoscience and Remote Sensing Symposium. IGARSS'99 (Cat. No. 99CH36293)*, volume 3, pages 1680–1682. IEEE. 102
- Lukasheh, A. F., Droste, R. L., and Warith, M. A. (2001). Review of expert system (ES), geographic information system (GIS), decision support system (DSS), and their applications in landfill design and management. *Waste Management & Research: The Journal for a Sustainable Circular Economy*, 19(2):177–185. 39
- Lv, X., Yazici, B., Zeghal, M., Bennett, V., and Abdoun, T. (2014). Joint-scatterer processing for time-series InSAR. *IEEE Transactions on Geoscience and Remote Sensing*, 52(11):7205–7221. 33
- McInnes, L., Healy, J., Saul, N., and Großberger, L. (2018). Umap: Uniform manifold approximation and projection. *Journal of Open Source Software*, 3(29):861. 61, 62
- Meyer, K., Erdogmus, E., Morcou, G., and Naughtin, M. (2008). Use of ground penetrating radar for accurate concrete thickness measurements. In *AEI 2008*. American Society of Civil Engineers. 18
- Milillo, P., Giardina, G., Perissin, D., Milillo, G., Coletta, A., and Terranova, C. (2019). Pre-collapse space geodetic observations of critical infrastructure: The morandi bridge, genoa, italy. *Remote Sensing*, 11(12):1403. 37
- Minh, D. H. T., Hanssen, R., and Rocca, F. (2020). Radar interferometry: 20 years of development in time series techniques and future perspectives. *Remote Sensing*, 12(9):1364. 35
- Monserrat, O., Crosetto, M., Cuevas, M., and Crippa, B. (2011). The thermal expansion component of persistent scatterer interferometry observations. *IEEE Geoscience and Remote Sensing Letters*, 8(5):864–868. 32, 34
- Montazeri, S., Zhu, X. X., Eineder, M., Hanssen, R., and Bamler, R. (2015). Deformation monitoring of urban infrastructure by tomographic SAR using multi-view TerraSAR-x data stacks. In *Proceedings of Fringe 2015: Advances in the Science and Applications of SAR Interferometry and Sentinel-1 InSAR Workshop*. European Space Agency. 35
- Moreira, A., Prats-Iraola, P., Younis, M., Krieger, G., Hajnsek, I., and Papathanassiou, K. P. (2013). A tutorial on synthetic aperture radar. *IEEE Geoscience and Remote Sensing Magazine*, 1(1):6–43. 22
- Newbry, L. (1960). Terrain radar reflectance study. *Photogrammetric Engineering*, 26(4):630–637. 20
- Ogushi, Matsuoka, Defilippi, and Pasquali (2019). Improvement of persistent scatterer interferometry to detect large non-linear displacements with the  $2\pi$  ambiguity by a non-parametric approach. *MDPI*, 11(21):2467. 32, 34
- Ogushi, F., Matsuoka, M., Defilippi, M., and Pasquali, P. (2021). Implementation of non-linear non-parametric persistent scatterer interferometry and its robustness for displacement monitoring. *MDPI*, 21(3):1004. 32, 34

- Osmanoğlu, B., Sunar, F., Wdowinski, S., and Cabral-Cano, E. (2016). Time series analysis of InSAR data: Methods and trends. *ISPRS Journal of Photogrammetry and Remote Sensing*, 115:90–102. 35
- Ossowska, A. (2015). *Highly resolved synthetic aperture radar with beam steering*, volume 77. KIT Scientific Publishing. 24
- Peake, W. H. and Oliver, T. L. (1971). The response of terrestrial surfaces at microwave frequencies. Technical report, Defense Technical Information Center. 18, 19
- Perissin, D., Wang, Z., and Wang, T. (2011). The sarproz insar tool for urban subsidence/manmade structure stability monitoring in china. *Proceedings of the ISRSE, Sidney, Australia*, 1015. 103
- Prats-Iraola, P., Scheiber, R., Marotti, L., Wollstadt, S., and Reigber, A. (2012). TOPS interferometry with TerraSAR-x. *IEEE Transactions on Geoscience and Remote Sensing*, 50(8):3179–3188. 32
- Preisendorfer, R. W. (1988). *Principal component analysis in meteorology and oceanography*. Elsevier. 45
- Reigber, A. and Moreira, A. (2000). First demonstration of airborne SAR tomography using multibaseline l-band data. *IEEE Transactions on Geoscience and Remote Sensing*, 38(5):2142–2152. 35
- Rignot, E. J. and Van Zyl, J. J. (1993). Change detection techniques for ers-1 sar data. *IEEE Transactions on Geoscience and Remote sensing*, 31(4):896–906. 102
- Rosen, P. A., Hensley, S., Joughin, I. R., Li, F. K., Madsen, S. N., Rodriguez, E., and Goldstein, R. M. (2000). Synthetic aperture radar interferometry. *Proceedings of the IEEE*, 88(3):333–382. 28, 30
- Rosen, P. A., Hensley, S., Peltzer, G., and Simons, M. (2004). Updated repeat orbit interferometry package released. *Eos, Transactions American Geophysical Union*, 85(5):47–47. 103
- Rosenqvist, A., Shimada, M., Ito, N., and Watanabe, M. (2007). Alos palsar: A pathfinder mission for global-scale monitoring of the environment. *IEEE Transactions on Geoscience and Remote Sensing*, 45(11):3307–3316. 102
- Rosenqvist, A., Shimada, M., Suzuki, S., Ohgushi, F., Tadono, T., Watanabe, M., Tsuzuku, K., Watanabe, T., Kamijo, S., and Aoki, E. (2014). Operational performance of the alos global systematic acquisition strategy and observation plans for alos-2 palsar-2. *Remote Sensing of Environment*, 155:3–12. 102
- Rüeger, J. M. (1996). Propagation of electromagnetic waves through the atmosphere. In *Electronic Distance Measurement*, pages 48–72. Springer Berlin Heidelberg. 17
- Samiei Esfahany, S., Hanssen, R., Thienen-Visser, K., and Muntendam-Bos, A. G. (2009). On the effect of horizontal deformation on insar subsidence estimates. In *Fringe*. 37
- Sample, J. T. and Ioup, E. (2010). *Tile-Based Geospatial Information Systems*. Springer US. 86
- Sanabria, M. P., Guardiola-Albert, C., Tomás, R., Herrera, G., Prieto, A., Sánchez, H., and Tessitore, S. (2014). Subsidence activity maps derived from dinsar data: Orihuela case study. *Natural Hazards and Earth System Sciences*, 14(5):1341–1360. 38, 64
- SARMAP (2014). Sarscape: Ps tutorial. [https://www.sarmap.ch/tutorials/PS\\_Tutorial\\_V\\_0\\_9.pdf](https://www.sarmap.ch/tutorials/PS_Tutorial_V_0_9.pdf). 47, 58, 63, 103
- Scheiber, R. and Moreira, A. (2000). Coregistration of interferometric SAR images using spectral diversity. *IEEE Transactions on Geoscience and Remote Sensing*, 38(5):2179–2191. 32
- Schneider, P. J., Khamis, R., and Soergel, U. (2020). Extracting and evaluating clusters in DInSAR Deformation data on single buildings. *ISPRS Annals of Photogrammetry, Remote Sensing and Spatial Information Sciences*, V-3-2020:157–163. 12, 58, 62
- Schneider, P. J. and Soergel, U. (2020a). Monitoring einer Schleuse mittels Persistent-Scatterer-Interferometrie. *avn - allgemeine vermessungs-nachrichten*, 3:118–123. 12

- Schneider, P. J. and Soergel, U. (2020b). Monitoring einer Schleuse mittels satellitengestützter DInSAR-Techniken. In *Publikationen der DGPF*, pages 448–456. 40. Wissenschaftlich-Technische Jahrestagung der DGPF in Stuttgart. 12
- Schneider, P. J. and Soergel, U. (2021a). Clustering persistent scatterer points based on a hybrid distance metric. In *Lecture Notes in Computer Science*, pages 621–632. Springer International Publishing. 12
- Schneider, P. J. and Soergel, U. (2021b). Segmentation of buildings based on high resolution persistent scatterer point clouds. *ISPRS Annals of the Photogrammetry, Remote Sensing and Spatial Information Sciences*, V-3-2021:65–71. 12, 61
- Schneider, P. J. and Soergel, U. (2022). Matching persistent scatterer clusters to building elements in mesh representation. *Accepted for Publication in: ISPRS Annals of the Photogrammetry, Remote Sensing and Spatial Information Sciences*, V-3-2022:update: 65–71. 12
- Schunert, A., Schack, L., and Soergel, U. (2012). Matching Persistent Scatterers to Buildings. *ISPRS - International Archives of the Photogrammetry, Remote Sensing and Spatial Information Sciences*, XXXIX-B7:79–84. 38, 57
- Schunert, A. and Soergel, U. (2016). Assignment of persistent scatterers to buildings. *IEEE Transactions on Geoscience and Remote Sensing*, 54(6):3116–3127. 38
- Scoular, J., Ghail, R., Mason, P., Lawrence, J., Bellhouse, M., Holley, R., and Morgan, T. (2020). Retrospective InSAR analysis of east london during the construction of the lee tunnel. *Remote Sensing*, 12(5):849. 37
- Sharifi, A. (1999). Remote sensing and decision support systems. In *Spatial Statistics for Remote Sensing*, pages 243–260. Springer Netherlands. 85
- Siddique, M., Wegmüller, U., Hajnsek, I., and Frey, O. (2018). SAR tomography as an add-on to PSI: Detection of coherent scatterers in the presence of phase instabilities. *Remote Sensing*, 10(7):1014. 35
- Simonetto, E. and Follin, J.-M. (2011). An overview on interferometric SAR software and a comparison between DORIS and SARSCAPE packages. In *Lecture Notes in Geoinformation and Cartography*, pages 107–122. Springer Berlin Heidelberg. 35
- Smarsly, K. and Tauscher, E. (2015). Ifc-based monitoring information modeling for data management in structural health monitoring. In *The 20th International Conference on the Applications of Computer Science and Mathematics in Architecture and Civil Engineering*. 68
- Sousa, J. J., Hooper, A. J., Hanssen, R. F., Bastos, L. C., and Ruiz, A. M. (2011). Persistent scatterer InSAR: A comparison of methodologies based on a model of temporal deformation vs. spatial correlation selection criteria. *Remote Sensing of Environment*, 115(10):2652–2663. 35
- SWR (2019). “Risse in Hausfassade über S-21-Tunnel entdeckt” Accessed August. 11 2022. <https://www.stuttgarter-zeitung.de/inhalt.stuttgart-21-risse-in-hausfassade-ueber-s-21-tunnel-entdeckt.32ff91dd-87c0-4b4a-9d0f-4d52d3b455fa.html>. 76
- Thompson\*, A. A. (2015). Overview of the radarsat constellation mission. *Canadian Journal of Remote Sensing*, 41(5):401–407. 102
- Tofani, V., Raspini, F., Catani, F., and Casagli, N. (2013). Persistent scatterer interferometry (PSI) technique for landslide characterization and monitoring. *Remote Sensing*, 5(3):1045–1065. 36
- Toma, S.-A., Bogdan, S., Focsa, A., and Pura, M.-L. (2019). On anomalous deformation profile detection through supervised and unsupervised machine learning. In *IGARSS 2019 - 2019 IEEE International Geoscience and Remote Sensing Symposium*, pages 7419–7422. 39
- Torres, R., Lokas, S., Bibby, D., Geudtner, D., Navas-Traver, I., Vega, F. C., Osborne, S., Poupaert, J., Cossu, M., and Touveneau, M. (2021). The sentinel-1c/-1d development and deployment plan. In *EUSAR 2021; 13th European Conference on Synthetic Aperture Radar*, pages 1–4. VDE. 102



- Torres, R., Snoeij, P., Geudtner, D., Bibby, D., Davidson, M., Attema, E., Potin, P., Rommen, B., Floury, N., Brown, M., et al. (2012). Gmes sentinel-1 mission. *Remote sensing of environment*, 120:9–24. 102
- van der Maaten, L. and Hinton, G. (2008). Visualizing data using t-sne. *Journal of Machine Learning Research*, 9:2579–2605. 62
- Van Leijen, F. (2014). *Persistent Scatterer Interferometry based on geodetic estimation theory*. PhD thesis, TU Delft. 33
- van Leijen, F. and Hanssen, R. (2007). Ground water management and its consequences in delft, the netherlands as observed by persistent scatterer interferometry. In *Fifth International Workshop on ERS/Envisat SAR Interferometry, 'FRINGE07', Frascati, Italy*, page 4.
- Vanlande, R., Nicolle, C., and Cruz, C. (2008). IFC and building lifecycle management. *Automation in Construction*, 18(1):70–78. 68
- Via, G. D., Crosetto, M., and Crippa, B. (2012). Resolving vertical and east-west horizontal motion from differential interferometric synthetic aperture radar: The l'aquila earthquake. *Journal of Geophysical Research: Solid Earth*, 117(B2):n/a–n/a. 37
- Volk, R., Stengel, J., and Schultmann, F. (2014). Building information modeling (BIM) for existing buildings — literature review and future needs. *Automation in Construction*, 38:109–127. 65
- Vollrath, A., Zucca, F., Bekaert, D., Bonforte, A., Guglielmino, F., Hooper, A., and Stramondo, S. (2017). Decomposing dinsar time-series into 3-d in combination with gps in the case of low strain rates: An application to the hyblean plateau, sicily, italy. *Remote Sensing*, 9. 64
- Wang, Y. and Zhu, X. X. (2015). Automatic feature-based geometric fusion of multiview TomoSAR point clouds in urban area. *IEEE Journal of Selected Topics in Applied Earth Observations and Remote Sensing*, 8(3):953–965. 35
- Wegmuller, U. (1999). Automated terrain corrected SAR geocoding. In *IEEE 1999 International Geoscience and Remote Sensing Symposium. IGARSS'99 (Cat. No.99CH36293)*, volume 10, pages 48–52. IEEE. 27, 32
- Werner, C., Strozzi, T., Wegmuller, U., and Wiesmann, A. (2002). SAR geocoding and multi-sensor image registration. In *IEEE International Geoscience and Remote Sensing Symposium*. IEEE. 27
- Werner, C., Wegmüller, U., Strozzi, T., and Wiesmann, A. (2000). Gamma sar and interferometric processing software. In *Proceedings of the ers-envisat symposium, Gothenburg, Sweden*, volume 1620, page 1620. Citeseer. 103
- Werner, C., Wegmuller, U., Strozzi, T., and Wiesmann, A. (2003). Interferometric point target analysis for deformation mapping. In *IGARSS 2003. 2003 IEEE International Geoscience and Remote Sensing Symposium. Proceedings (IEEE Cat. No.03CH37477)*. IEEE. 33
- Werninghaus, R. and Buckreuss, S. (2009). The terrasars-x mission and system design. *IEEE Transactions on Geoscience and Remote Sensing*, 48(2):606–614. 102
- Wiley, C. A. (1954). Pulsed doppler radar methods and apparatus, u.s. patent 3 196 436, 1954. U.S. Patent 3 196 436, 1954. U.S. Patent 3 196 436, 1954. 22
- Xaypraseuth, P., Satish, R., and Chatterjee, A. (2015). Nisar spacecraft concept overview: Design challenges for a proposed flagship dual-frequency sar mission. In *2015 IEEE Aerospace Conference*, pages 1–11. IEEE. 102
- Yamamoto, T., Kawano, I., Iwata, T., Arikawa, Y., Itoh, H., Yamamoto, M., and Nakajima, K. (2013). Autonomous precision orbit control of alos-2 for repeat-pass sar interferometry. In *2013 IEEE International Geoscience and Remote Sensing Symposium - IGARSS*, pages 2404–2407. 25
- Yin, H., Zhu, J., Li, Z., Ding, X., and Wang, C. (2011). Ground subsidence monitoring in mining area using dinsar sbas algorithm. *Acta Geodaetica et Cartographica Sinica*, 40(1):52–58. 35
- Yoneyama, K., Koizumi, T., Suzuki, T., Kuramasu, R., Araki, T., Ishida, C., Kobayashi, M., and Kakuichi, O. (1990). Jers-1 development status. *Acta Astronautica*, 21(11-12):783–794. 102

- Zhang, Q., Luo, Y., and an Chen, Y. (2017). Introduction. In *Micro-Doppler Characteristics of Radar Targets*, pages 1–14. Elsevier. 18
- Zhu, M., Wan, X., Fei, B., Qiao, Z., Ge, C., Minati, F., Vecchioli, F., Li, J., and Costantini, M. (2018). Detection of building and infrastructure instabilities by automatic spatiotemporal analysis of satellite sar interferometry measurements. *Remote Sensing*, 10(11):1816. 38, 57
- Zhu, X. X. and Shahzad, M. (2014). Facade reconstruction using multiview spaceborne TomoSAR point clouds. *IEEE Transactions on Geoscience and Remote Sensing*, 52(6):3541–3552. 35

# Acknowledgments

First of all, I would like to thank my parents, who supported me selflessly and full of love through the last 25 years of education, and my partner Rebeca for her partnership, who I always know patiently and understanding on my side.

Special thanks to the members of the Institute for Photogrammetry (IFP) for countless advice, discussions and input, also during the global pandemic. Here special thanks to Markus Englich, without his outstanding technical support, this research would not have been possible. Carmen and Ute for helping me with paper work and administrative issues. Micheal Kölle for being a smart and funny discussion- and office partner. Uwe Sörgel for giving me the opportunity to work at the IFP, and for his support and supervision while conducting this thesis. Thanks to my co-author Rami Khamis for straightforwardly providing ground truth measurements for the construction sites.

I also would like to thank Dr. Chia-Hsiang Yang for the introduction to PSI and SAR processing at the beginning of my time at IFP and all my master students who carried out experiments. Here, especially to Yang Li for the support in the implementation of web platforms. Thanks to Michele Crosetto for inviting me to run experiments with the CTTC's PSI processing chain, and to Qi Gao for advising me during my time in Barcelona.

The TerraSAR-X data was provided by the *German Aerospace Center* (DLR) through the proposal LAN0634 and HYD353. I would like to thank the *State Office for Spatial Information and Land Development Baden-Württemberg* (LGL) for providing citywide ALS/Mesh data and orthophotos for Stuttgart. Furthermore, I want to acknowledge the open data policy of Berlin's Senate Department for Urban Development and Housing, Department III - Geoinformation, their uncomplicated and practical approach to public data provided us with a digital surface model and the mesh of the central station. This research was partially founded by the German Federal Ministry for Economic Affairs and Climate Action (BMWK) and the German Federal Institute of Hydrology (bfg). Last but not least, we want to appreciate the work of the unknown user *AleX\_BY*, who created and provided the detailed model of the *Reichstag*.



# Curriculum Vitae

## Personal

Name	Philipp J. Schneider
Date of Birth	January 19, 1991
Place of Birth	Stuttgart, Germany

## Education

2018 - 2023	Doctoral studies, Faculty for Aerospace Engineering and Geodesy, University of Stuttgart
2015 - 2018	Master of Science, Geodesy and Geoinformatics, University of Stuttgart Master Thesis: <i>Klassifikation von Verkehrsteilnehmern in FMCW-RADAR Mikro-Doppler Signaturen mittels CNN, basierend auf simulierten und realen Trainingsdaten</i>
2012 - 2015	Bachelor of Science, Geodesy and Geoinformatics, University of Stuttgart Bachelor Thesis: <i>Automatische Erkennung von Gebäudeinfrastrukturelementen in Sensordaten des Project Tango Tablets</i>
2007 - 2010	Fanny-Leicht-Gymnasium, Stuttgart
1997 - 2007	Michael Bauer Schule

## Experience

2018 - 2023	Research Associate, Institute for Photogrammetry, University of Stuttgart
2017 - current	Freelance: Design and evaluation of sensor systems. Diehl Defence GmbH, Daimler AG, Institute for Navigation, Institute of Sport and Movement Science.
2016 - 2018	Research Assistant, Institute for Navigation, University of Stuttgart
2014 - 2018	Teaching Assistant, Institute for Photogrammetry, University of Stuttgart

## Awards

2019	DVW Harbert Award for year's best masters's degree
------	----------------------------------------------------